12-2002

Power Scaling Feasibility of Chromium-Doped II-VI Laser Sources and the Demonstration of a Chromium-Doped Zinc Selenide Face-Cooled Disk Laser

Jason B. McKay

Power Scaling Feasibility of Chromium-Doped II-VI Laser Sources and the Demonstration of a Chromium-Doped Zinc Selenide Face-Cooled Disk Laser

DISSERTATION

Jason B. McKay, Captain, USAF

AFIT/DS/ENP/02-5

DEPARTMENT OF THE AIR FORCE
AIR UNIVERSITY

AIR FORCE INSTITUTE OF TECHNOLOGY

Wright-Patterson Air Force Base, Ohio

The views expressed in this thesis are those of the author and do not reflect the official policy or position of the Department of Defense or the U. S. Government.

AFIT/DS/ENP/02-5

POWER SCALING FEASIBILITY OF CHROMIUM-DOPED II-VI LASER SOURCES AND THE DEMONSTRATION OF A CHROMIUM-DOPED ZINC SELENIDE FACE-COOLED DISK LASER

DISSERTATION

Presented to the Faculty

Graduate School of Engineering and Management

Air Force Institute of Technology

Air University

Air Education and Training Command

In Partial Fulfillment of the Requirements for the

Degree of Doctor of Philosophy

Jason B. McKay, M.S.E.E.

Captain, United States Air Force

March 2003

AFIT/DS/ENP/02-5

Power Scaling Feasibility of Chromium-Doped II-VI Laser Sources and the Demonstration of a Chromium-Doped Zinc Selenide Face-Cooled Disk Laser

Jason B. McKay, M.S.E.E.
Captain, United States Air Force

Approved:

Won B. Roh (Co-Chair)	Date
Kenneth L. Schepler (Co-Chair)	Date
Alan V. Lair (Dean's Representative)	Date
Eric Magee(Member)	Date

Accepted:

Robert A. Calico, Jr. Dean, Graduate School of Engineering And Management	Date

Acknowledgements

I thank my research sponsor, and mentor, Dr. Kenneth Schepler, for his guidance, optimism, and timely moral and fiscal support over the course of this research, where the old saying “If you’re not breaking anything, you’re not working” was proven only too true. Many diode lasers died, so the chromium laser might live. I also thank Dave Mohler, the master designer and machinist who helped turn my optical system ideas into reality, despite predictions that “it would never work.”

Finally, I am indebted to Dr. Won Roh, my faculty advisor, for his keen insight, focus on the big picture of which I needed occasional reminding, and rapier wit that was most entertaining, as long as it was not directed at me.

Table of Contents

List of Figures

Page

List of Tables

Abstract

Tunable laser sources in the 2-4 μm spectral range are required for several Air Force sensor applications, yet choices are few in that spectral region, and no truly satisfactory source has yet been found for all applications. Additional source alternatives are needed in addition to the existing rare-earth lasers and non-linear optical sources. Chromium-doped II-VI (Cr^{2+}:II-VI) materials, a new and relatively undeveloped class of laser material, have the promise of tuning over most of the 2-4 μm region, but are susceptible to thermal effects and have other issues that make demonstration of sources with sufficient output power difficult. The output power of the Cr^{2+}:II-VI laser needs to be scaled up to meet military application requirements. This dissertation investigates the feasibility of using Cr^{2+}:II-VI laser materials to produce a laser with enough output power to be useful in military sensor applications.

This dissertation surveys Cr^{2+}:II-VI material properties and potential laser designs to assess power scaling feasibility, verifies feasibility with a laser demonstration, and then characterizes the thermal effects in the working laser material to help evaluate its effectiveness. The results of the survey show that the Cr^{2+}:II-VI laser materials (such as Cr^{2+}:ZnSe, Cr^{2+}:CdSe, and Cr^{2+}:CdMnTe) are especially susceptible to overheating and thermally-induced optical distortion, but otherwise are quite satisfactory laser materials. Cr^{2+}:ZnSe is the most promising, due to its high thermal conductivity and relatively high maximum Cr^{2+} doping concentration. A face-cooled disk laser design using Cr^{2+}:ZnSe looks most feasible for efficient power scaling at the power levels useful for sensor

applications, as it produces high efficiency but low thermal distortion without requiring inordinate amounts of input power. The laser demonstration described in this dissertation shows that the Cr^{2+}:ZnSe disk laser can produce sufficient output power, which validated the design. Interestingly, the laser built in this research works well only under a restricted set of conditions, an unexpected development that the thermal analysis explores. The thermal analysis shows that the restriction is not the fault of the disk laser design itself, but of an experimental deviation from the ideal design parameters that require a uniform absorbed power distribution in the laser disk. Several modifications to the disk laser are discussed that should solve the disk-heating problem and make the Cr^{2+}:ZnSe disk laser operate as originally designed. This research concludes that Cr^{2+}:II-VI laser materials can produce enough power to be useful sources for military laser applications, if enough effort is spent on ensuring adequate thermal management in the laser material.

POWER SCALING FEASIBILITY OF CHROMIUM-DOPED II-VI LASER SOURCES AND THE DEMONSTRATION OF A CHROMIUM-DOPED ZINC SELENIDE FACE-COOLED DISK LASER

1 Introduction

1.1 Background

Compact, tunable, room temperature, solid state laser sources operating in the mid-IR spectral region are of interest to the military for a number of applications such as eyesafe laser radar, remote sensing, and infrared countermeasures. Unfortunately, there are few choices for tunable sources in the 2-4 μm spectral region that are suitable for military applications. Additional sources are needed in the 2-4 μm spectral region that are efficient, produce several watts of continuous wave or high repetition rate pulsed output power, are tunable over sizeable portions of the 2-4 μm range, and operate at room temperature.

A promising class of laser materials being investigated for mid-IR source feasibility is II-VI materials doped with chromium. II-VI materials are compounds of Group IIb transition metals and Group VI chalcogens from the periodic table. Many II-VI materials are semiconductors with large band gap and excellent mid-infrared transmission, ideal host materials for the chromium ion that, in the 2+ oxidation state, has a laser transition in the 2-3.5-μm wavelength range. Doping chromium into II-VI hosts such as zinc selenide[1], cadmium selenide[2], cadmium manganese telluride[3], etc. results in laser materials with high quantum yield and extremely broad spectral bandwidth. Recent laser

demonstrations involving the most developed chromium-doped II-VI material, Cr^{2+}:ZnSe, indicate the promise of these materials for use as mid-IR sources. Cr^{2+}:ZnSe lasers have demonstrated spectral tuning from 2.1 to 2.8 μm[4], with up to 63% slope efficiency and 1.8 watts maximum continuous output power at the peak emission wavelength of 2.4 μm[5]. Mode-locked operation has been demonstrated, producing 4-ps pulses[6, 7]. Diode pumping has been shown to be possible using diode lasers in the 1.5-1.8 μm range[8, 9]. Thus, chromium doped zinc selenide looks promising for tunable laser applications requiring high power in the 2-3 micron range. The feasibility of the other chromium-doped II-VI laser materials, such as Cr^{2+}:CdSe and Cr^{2+}:CdMnTe, is more uncertain, as these materials are not as well developed as Cr^{2+}:ZnSe is. Work still needs to be done to optimize and power scale the "initial demonstration" chromium lasers into useful devices, and to investigate the as-yet ignored potential of other chromium-doped II-VI materials.

1.2 Problem Statement

At the start of this research, no Cr^{2+}:II-VI laser had been demonstrated with the output power, tunability, and beam quality needed for military applications, although the potential was there. The Cr^{2+} laser output power needed to be scaled up to at least 5 W while maintaining tunability and good beam quality to be suitable for military applications.

Unfortunately, power scaling the Cr^{2+}:II-VI laser is made difficult by limitations in Cr^{2+}:II-VI materials technology and the properties of the Cr^{2+}:II-VI materials. It is difficult to grow low loss samples of Cr^{2+}-doped materials that have enough chromium

for efficient absorption of pump power. Efficient diode laser pumping of Cr^{2+}:II-VI materials at the 10-20 W power level is not yet possible, because the 5-8 μs excited state lifetime of Cr^{2+} requires pumping intensities of at least 2-3 kW/cm^2 for efficient laser operation, higher than what existing high power diode lasers can produce at the Cr^{2+} absorption band of 1.6-2.0 μm. High-energy pulsed operation of the Cr^{2+} laser does not look feasible, because the faint chromium doping densities (<0.1% Cr^{2+}) and short excited state lifetime make energy storage limited in Cr^{2+}:II-VI materials. Therefore, the likely modes of operation of the Cr^{2+} laser are similar to those of the familiar Ti:Al_2O_3 laser: CW, mode-locked, or gain-switched operation, pumped by a high brightness solid-state pump laser. Furthermore, intense pumping combined with a rather strong dependence of refractive index on temperature[10] makes thermal lensing a serious problem at the watt level of output power[5]. Overall heat flow must also be optimized, as the nonradiative relaxation rates increase strongly with temperature above 300 K[11]. These issues have to be dealt with in order to successfully develop a 5-W Cr^{2+}:II-VI laser.

1.3 Research Objective

The objective of this research effort was to build and test a 5-W Cr^{2+} laser operating at room temperature, and investigate the issues involved with Cr^{2+} laser optimization: Cr^{2+} doping level and fluorescence lifetime in Cr^{2+}:II-VI materials, resonator design, heat management, thermal lens control, and pumping configuration. The research focused on the more developed chromium-doped II-VI materials such as Cr^{2+}:CdSe and Cr^{2+}:ZnSe, as they showed the most promise for immediate power scaling.

1.4 Methodology

The research consisted of the following phases, presented as chapters in the dissertation: background research (Chapter 2), material characterization (Chapter 3), laser design (Chapter 4), pump source design (Chapter 5), laser demonstration (Chapter 6), thermal lensing analysis (Chapter 7), and conclusions (Chapter 8). In the background research phase, the literature was surveyed to assess power scaling feasibility for Cr^{2+} materials, and identify the pertinent design issues and constraints involved. Background research included the investigation of Cr^{2+}:II-VI properties, the development of a simple laser model, and a feasibility study of various resonator architectures. The material characterization phase consisted of experiments designed to further investigate aspects of Cr^{2+}:II-VI material properties that, according to the background research, might have significant impact on laser design. These experiments included the determination of maximum Cr^{2+} doping levels, dependence of Cr^{2+} excited state lifetime on temperature, bandwidth of Cr^{2+} stimulated emission cross sections, estimated thermal loading, and long-wavelength limit of the Cr^{2+} laser tuning range. The results from these experiments provided insight that aided in the selection of the final Cr^{2+} laser design and in evaluation of subsequent laser performance. The laser design phase used the knowledge gained in the background research and material characterization efforts to produce the final laser design, a Cr^{2+}:ZnSe disk laser, to be tested in power scaling experiments. In the next phase, pump source design, a diode-pumped Tm:YLF laser was designed and built to produce a high power pump source for the Cr^{2+} laser experiments. The laser demonstration phase consisted of the construction of the Cr^{2+}:ZnSe laser design and the

analysis of its performance. This phase consisted of the mounting and characterization of the Cr^{2+}:ZnSe disks, and the assembly and testing of several different Cr^{2+}:ZnSe disk laser configurations. In the thermal lensing analysis phase, the thermal lensing occurring in the Cr^{2+}:ZnSe disks was measured and compared to modeling results. In the final phase, conclusions, the research was summarized, power-scaling feasibility of Cr^{2+} lasers was determined, and recommendations for future Cr^{2+} laser research were made.

2 Background Research

Background research was definitely needed to identify important features of Cr^{2+} laser design and to set the stage for material characterization efforts. This chapter presents the highlights of the background research, surveying the literature to discuss Cr^{2+}:II-VI material properties, simple laser modeling, and laser power scaling design issues that pertain to the feasibility of power scaling the Cr^{2+} laser to the 5-W level.

2.1 Properties of Cr^{2+}:II-VI Materials

This section presents the material and spectroscopic properties of Cr^{2+}:II-VI materials pertinent to laser operation. Methods of crystal growth, overall Cr^{2+} energy level structure, properties of the laser transition, and thermo-mechanical properties of II:VI materials are discussed. A review of these properties will illustrate the strengths and weaknesses of the Cr^{2+}-doped II-VI materials as laser media, as well as provide the foundation for the laser model developed later in Section 2.2.

2.1.1 Methods of Cr^{2+}:II-VI Materials Growth

Cr^{2+}:II-VI laser materials are made by incorporating chromium into the lattice of II-VI compounds such as ZnSe, CdSe, $Cd_xMn_{1-x}Te$ by standard growth techniques such as Bridgman growth and seeded physical vapor transport, or by diffusion doping chromium into an undoped piece of previously grown II-VI material[2, 3, 12]. Chromium doping levels of 10^{18} cm^{-3} – 10^{19} cm^{-3} are typical, with optical loss increasing and excited state lifetime decreasing as the Cr concentration increases[13].

So far, the diffusion doping method seems to produce the best optical quality samples, but none of the manufacturing processes is very consistent. In the best

diffusion-doped samples (reported in the literature), optical round trip losses of 2%-5% for a 2-mm thick laser rod are typical. A larger variation in optical properties is observed with melt growth techniques than with diffusion doping, leading to a wide range of potential Cr doping levels, impurity/defect concentrations, and loss for similar growth conditions. Vapor transport is known to produce high quality single crystals, but the Cr^{2+} doping level of such crystals is low[2]. On the combined basis of consistency, loss, and Cr^{2+} doping density, diffusion doping appears to be superior to melt and vapor growth. However, the science (or art) of Cr^{2+}:II-VI material production is still in its early days, so a decision on the eventual best growth process is premature. For this research, however, diffusion-doped samples were used to reduce overall risk.

2.1.2 Cr^{2+} Energy Level Structure

A chromium atom has the electronic configuration $[Ar]3d^5 4s^1$. When chromium is doped into II-VI materials, the chromium atoms occupy the group II element (Cd, Zn, etc.) site in the II-VI host lattice, producing Cr^{2+} active ions in a tetrahedrally symmetric crystal field[14]. The 4s electron and one of the 3d electrons of the chromium atom in Cr:II-VI materials are used in bonding to the lattice, leaving the remaining 4 electrons in the partially filled 3d shell "active." The optical properties of Cr:II-VI materials are thus a combination of the properties of the II-VI semiconductor host and those produced by the Cr^{2+} energy levels formed by chromium $3d^4$ electrons in a tetrahedral crystal field. As the 3d shell is not shielded from the crystal lattice, the spectroscopic properties of Cr^{2+} doped materials are strongly affected by the host crystal lattice.

Although the complete spectrum of optical transitions in Cr:II-VI materials is quite complicated and not fully explained with simple models, the basic structure of the Cr:II-VI energy levels has been modeled with a fair amount of success as Cr^{2+} ions in a tetrahedral crystal field[15]. The energy level diagram of Figure 2-1[14] shows the first few Cr^{2+} levels in ZnSe, referenced to the semiconductor band gap. This energy level diagram for Cr:ZnSe is fairly representative for the entire class of chromium-doped II-VI materials.

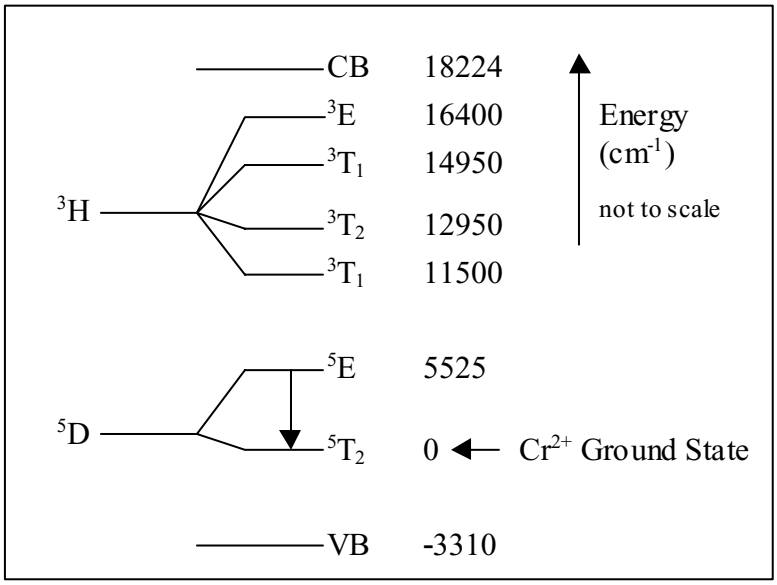

Figure 2-1 Cr^{2+} Energy Levels in Cr^{2+}:ZnSe as described by Grebe et al[14].

The energy levels associated with laser operation are the $^5T_2$ ground state and the ^5E excited state. Transitions to/from the other nearby excited states, the $^3T_1$ and $^3T_2$ states, are spin forbidden and are weak compared to the transition from $^5T_2$ to ^5E[15]. There is a possibility of excited state absorption (ESA) due to the ^5E-$^3T_1$ transition, but it was shown to have a small cross section in Cr^{2+}:ZnSe[16]. Thus, the $^5T_2$-^5E laser transition is the only significant Cr^{2+} spectral feature in the mid-infrared spectral region of 1.5-4 μm.

The II-VI materials themselves are fully transparent over the wavelength range of interest. In addition the II-VI materials have low phonon energies of approximately 300 cm^{-1}, rendering non-radiative relaxation of the Cr^{2+} excited state ^5E multi-phonon and hence weak at moderate temperatures[10]. The simple Cr^{2+} energy level structure and low interaction strength of transitions potentially parasitic to laser operation result in the promise of high efficiency and clean dynamics in Cr^{2+}:II-VI lasers.

2.1.3 Properties of the Cr^{2+} Laser Transition

Although only the $^5T_2$ and ^5E energy levels play a significant role in Cr^{2+} dynamics in the mid-infrared spectral region, strong vibrational coupling[17] of those levels to the host lattice results in an effectively ideal four-level laser system with extremely wide spectral bandwidth. The general idea is illustrated in Figure 2-2 (shown for Cr^{2+}:CdSe). Since the Cr^{2+} active energy levels come from 3d electrons, the energy level wave-functions are not shielded by the rest of the electrons in the Cr^{2+} ion and are strongly coupled to the host lattice. The coupling is not the same for each energy level, as the various energy level wave-functions differ. This effect causes the bond lengths (modeled as a single 'configuration coordinate') around the Cr^{2+} ion at thermal equilibrium to vary according to what electronic state the ion is in. The difference between configuration coordinates at thermal equilibrium between the $^5T_2$ and ^5E levels is so large that a radiative transition is most likely to terminate at a high vibrational energy state that is effectively unpopulated at room temperature. Since the high vibrational energy states relax back to thermal equilibrium very quickly, this pair of energy levels acts effectively as the ideal four level configuration for low-threshold, highly efficient lasers. The

vibrational coupling also produces extremely broadband absorption and emission, each with at least 400-nm full-width-half-maximum (FWHM) bandwidth. Thus, the Cr^{2+}:II-VI laser material appears ideal for producing widely tunable, efficient, mid-infrared lasers.

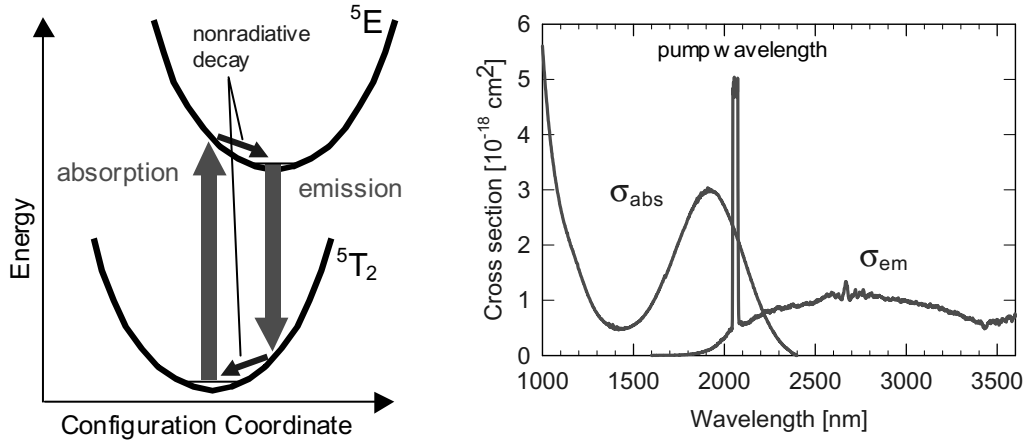

Figure 2-2 Cr^{2+}:CdSe Laser Transition Energy Level Diagram and Plot of Absorption and Stimulated Emission Cross Sections

Absorption in Cr:CdSe is peaked at 1.9 μm and has a smooth Gaussian shape at room temperature with 400-nm FWHM[2]. The emission is peaked at 2.6 μm and has at least 400-nm FWHM with a long tail going out towards 3.5 μm. Such broad absorption and emission bands enable the Cr^{2+}:II-VI laser to be pumped by broadband sources and raise the possibility of an extended tuning range. The features of other chromium-doped II-VI materials such as ZnSe[1] and CdMnTe[3] are similar, as shown in Table 2-1.

Table 2-1 Cr^{2+}:II-VI Laser Transition Properties

Property	Cr:CdSe	Cr:ZnSe	Cr:CdMnTe
Absorption Cross Section (10^{-18} cm^2)	3	0.87	2.7
Absorption Peak (nm)	1900	1750	1900
Stim. Emission Cross Section (10^{-18} cm^2)	1.8	0.92	
Emission Peak (nm)	2500	2350	2550
Lifetime at 293 K (μs)	5	8	4.5

The ^5E-$^5T_2$ transition of Cr^{2+} in II-VI materials is characterized by a large absorption/emission cross section in the 10^{-18} cm^2 range[1], and a short radiative lifetime of 6-8 microseconds. This is somewhat comparable to the better known Ti:Al_2O_3 laser, but with higher cross section and longer lifetime[12]. The large cross sections allow efficient absorption of the pump laser in 5-10 mm of gain material, resulting in fairly convenient laser rod geometry, given the available Cr^{2+} doping levels[12, 13] of 10^{18} cm^{-3} to 10^{19} cm^{-3}. The short lifetime proves to be both an advantage and a disadvantage to laser operation. The advantage is that the fast radiative rate effectively competes with nonradiative relaxation processes, rendering the radiative efficiency of the Cr^{2+}:II-VI system quite high at room temperature, unlike that of other transition metal ions with longer excited state lifetimes such as Fe^{2+} or Co^{2+}[1]. The disadvantage is that the short lifetime means that intense pumping is required to reach laser threshold, simply to compensate for the fast radiative decay of the excited state population.

2.1.4 Thermo-Mechanical Properties

Assessing the thermo-mechanical properties of a potential laser material is an important step in determining the eventual feasibility of using the material in mid-to-high

power lasers. The properties of interest are the temperature dependence of the refractive index (dn/dT), the thermal shock parameter (R_T), and the thermal conductivity (κ). A material with a refractive index that has a strong temperature dependence will introduce considerable optical distortion into the resonator, due to the inevitable temperature gradients set up inside the laser material by the absorption of the pump energy and the necessary cooling. The thermal shock parameter is a measure of resistance of a material to cracking while under thermal load – the higher this parameter is, the more intensely a laser material can be pumped before it fractures. The thermal conductivity is also very important, as a high thermal conductivity will lead to small temperature gradients in the material and low operating temperatures – likely producing higher efficiency laser operation than a material with lower thermal conductivity . A comparison of II-VI materials ZnS and ZnSe to more commonly known laser hosts is shown below in Table 2-2.

Table 2-2 Thermo-mechanical Properties of Various Laser Hosts[12]

Material	κ (W/mK)	R_T ($W/m^{1/2}$)	dn/dT (10^{-6}/K)
ZnS	17	7.1	+46
ZnSe	18	5.3	+70
CdSe/CdMnTe	4	No data	No data
YAG	10	4.6	+8.9
YLF	5.8	1.1	-2.0,-4.3
Phosphate glass	0.6	0.35	-5.1
Al_2O_3 (sapphire)	28	22	+12

The severity of thermally-induced optical distortion is typically estimated by calculating or measuring the optical power of the so-called “thermal lens” which arises due to the transverse temperature (and thus refractive index) profile that occurs in

pumped laser rods. Optical power of a lens is simply the inverse of the focal length of the lens (using units of diopters). Assuming a uniformly pumped cylinder, side cooled, and neglecting the impact of strains in the laser rod, the expression[18] for the thermal lens power is:

$$TLP = \frac{1}{f} \approx \frac{P_a}{2\kappa A}\frac{dn}{dT} \tag{2-1}$$

In this expression, TLP refers to the thermal lens power, f refers to the thermal lens focal length, κ refers to the thermal conductivity, A refers to beam cross sectional area, P_a refers to the absorbed power in the rod, and dn/dT refers to the change in refractive index with change in temperature. The greater the thermal lens power is, the stronger the thermally-induced optical distortion is. Although a typical laser rod will not be uniformly pumped, this simplified expression is good for illustrating the basic dependence of thermal distortion on material parameters. Note that the thermal lens power is proportional to the product of absorbed power per unit area (absorbed intensity) and the ratio of dn/dT to κ. The lower the ratio of dn/dT to κ, the more power per unit area can be absorbed for the same thermal lens power. The ratio is 2.57×10^5 W/m for ZnSe, compared to 23.3×10^5 W/m for sapphire and 11.2×10^5 W/m for YAG, based on values shown in Table 2-2. Thermal distortion will be 9 times stronger in ZnSe than in sapphire, and 4.3 times stronger than in YAG, for a given heat load. Thermal lensing in Cr^{2+}:II-VI materials should therefore be expected to be a significant issue in laser design, and so far has indeed been a problem[5].

If the thermal distortion can be somehow avoided or mitigated, the II-VI materials should be able to handle quite large heat loads. The thermal shock resistance (R_T values) of the zinc based II-VI materials such as ZnS and ZnSe are quite good, less than sapphire but more than YAG and considerably more than YLF or phosphate glass. Although R_T data are not available for cadmium-based chalcogenides such as CdSe and CdMnTe, their lower thermal conductivity than ZnS and ZnSe likely means a lower thermal-shock resistance. In any case, it would not be any worse than that of YLF, a commonly used host material for 10-20W rare-earth lasers. Therefore, thermal-induced optical distortion, but not thermal fracture, will be the main obstacle in demonstrating a 5-W Cr^{2+} laser.

2.1.5 Summary

In summary, the Cr^{2+}:II-VI materials look promising for tunable laser applications in the 2-3 μm range, judging from the spectroscopic data. The ^5E-$^5T_2$ mid-infrared transition acts as a nearly ideal four level system, has good radiative efficiency at room temperature, has a broad bandwidth for tuning, and appears to be free of any parasitic processes such as ESA that could limit the usefulness of the materials. However, the short lifetime and greater than average susceptibility to thermal distortion of Cr^{2+}:II-VI materials may cause some difficulty with high power laser demonstration.

2.2 Laser Modeling

Laser modeling is a useful tool for estimating feasibility of different resonator designs to enable the research (and the budget) to be focused on the most promising configurations. Often even the simplest of models can prove very useful as a laser design aid. This research employed a simple laser model that consisted of two parts: a one-

dimensional laser dynamics model using the rate-equation approach and a simple stability and mode overlap analysis using the ray-trace method with complex beam parameter. The one-dimensional dynamics model was useful in predicting input power levels needed for a given Cr^{2+} laser configuration and what the output efficiency might be, assuming the resonator was properly designed. The stability analysis provided insight into what the proper design of the resonator needed to be to achieve the results predicted by the one-dimensional dynamics model. This two-part laser model was very useful in the feasibility analysis of resonator designs and the interpretation of results from the Cr^{2+} laser experiments. This section presents the laser model used in this research, discussing the laser rate equations that underlie the dynamics model, the one-dimensional laser dynamics model itself, and the stability and mode overlap analysis of a simple optical resonator typical of those used in this research. In the end, the simple model is proven adequate for qualitative prediction of laser behavior, exactly what was needed for both the design feasibility evaluation and interpretation of Cr^{2+} laser results.

2.2.1 Cr^{2+} Laser Rate Equations

The laser dynamics model used in this research is based on rate equations describing the population densities and dynamics of the electronic states of Cr^{2+} ions in Cr^{2+}:II-VI laser materials. This section presents a simplified set of Cr^{2+} energy level population rate equations, the assumptions behind them, and defines the parameters needed for the laser dynamics model.

Cr^{2+}:II-VI laser dynamics are well modeled by two energy levels, the $^5T_2$ ground state and the ^5E excited state. Any Cr^{2+} ion in the material has to be in either the ground state

or excited state – a closed system. Transition processes between the two states consist of absorption, emission, and non-radiative relaxation. Due to the large energy difference between the states, non-radiative relaxation is overwhelmingly a transition from the excited state to the ground state. Thus, the rate equations need to merely describe absorption, emission, and non-radiative relaxation between the excited state and the ground state. Before the rate equations are written, a few simplifying assumptions are in order.

1. **The nonradiative relaxation rate from ^5E to $^5T_2$ is constant.** To be accurate, this assumption requires laser material temperature to be constant during laser operation.
2. **Excited state absorption is not significant**. This assumption has been justified in Cr^{2+}:ZnSe by spectroscopic studies[19] but remains to be validated for other II-VI hosts.
3. **All Cr^{2+} sites are equivalent (homogeneous broadening).** This appears to be true based on laser efficiency while operating narrow-band. At the least, the homogeneous linewidth dominates.
4. **Excitation and lasing bandwidth are both narrow with respect to the transition bandwidth.** This assumption is reasonable, given 50-75 nm FWHM or less free running laser bandwidth but 400-nm FWHM transition cross section bandwidth.
5. **The conditions for quasi-four level laser dynamics are satisfied.** The material is being pumped close to the absorption peak at ~1.8-1.9 μm and the laser is

operating close to or on the long-wavelength side of the emission peak, ensuring quasi-four level laser dynamics.

6. **Vibronic relaxation of excited Cr^{2+} ions to the minimum of the excited state energy band is very fast.** Pulsed laser experiments do not show signs of time lag when pumping with 40-ns FWHM pulses. Cr^{2+} laser "turn-on" in a short cavity is virtually at the leading edge of the pump pulse. The vibronic relaxation time is thus orders of magnitude shorter than the excited state lifetime.

With those assumptions in place, the rate equations for the two states can now be written:

$$\frac{dN_2}{dt} = -\frac{N_2}{\tau} + \frac{\sigma_{abs} I_p}{h\nu_p} N_1 - \frac{\sigma_{em} I_L}{h\nu_L} N_2 \tag{2-2}$$

$$\frac{dN_1}{dt} = -\frac{dN_2}{dt} \tag{2-3}$$

$$N = N_1 + N_2 \tag{2-4}$$

N_2 and N_1 refer to the population density of the excited and ground states in the laser material, respectively. N represents the total Cr^{2+} concentration in the material. σ_{abs} and σ_{em} refer to absorption and emission transition cross sections, τ denotes the excited state lifetime produced by the combination of radiative and non-radiative decay rates, ν_p and ν_L refer to the pump and laser photon frequencies, and I_P, I_L denote pump and resonated light intensities.

The assumption of equilibrium ($dN_{1,2}/dt = 0$) simplifies these equations further, and is justified in continuous wave (CW) laser operation, as input pump intensity remains constant and the populations adjust until the net rate of change is zero. It is reasonable even for pulsed Cr^{2+} laser operation, as the low energy-storage capability of Cr^{2+}

materials typically ensures that pulsed Cr^{2+} lasers are often run in quasi-CW configuration by pumping with a pulsed source. The resulting simplified equation is:

$$N_2 = N_1 \frac{\sigma_{abs} I_p \tau}{h\nu_p} \left(\frac{1}{1 + \frac{\sigma_{em} I_L \tau}{h\nu_L}} \right) \tag{2-5}$$

Optical gain results when it is more likely for a photon at the emission transition wavelength to stimulate emission from the excited state than be absorbed. As long as the Cr^{2+} laser wavelength is greater than about 2.4 μm in Cr^{2+}:ZnSe or 2.5 μm in Cr^{2+}:CdSe, the probability of absorption is negligible, and any population of Cr^{2+} ions in the excited state results in optical gain. With this restriction, gain depends only on N_2. The expression for the optical gain coefficient is simply excited state population times the stimulated emission cross section:

$$\gamma = N_2 \sigma_{em} \cong \sigma_{em} N_1 \frac{\sigma_{abs} I_p \tau}{h\nu_p} \left(\frac{1}{1 + \frac{\sigma_{em} I_L \tau}{h\nu_L}} \right) \tag{2-6}$$

A further simplification results if the excited state population is small compared to the total Cr^{2+} concentration, so that essentially the entire Cr^{2+} concentration in the sample remains in the ground state. In this case, the resulting optical gain can be expressed in terms of Cr^{2+} concentration, transition parameters, pump photon frequency, and emitted photon frequency.

$$\gamma \approx N_2 \sigma_{em} \cong \sigma_{em} N \frac{\sigma_{abs} I_p \tau}{h\nu_p} \left(\frac{1}{1 + \frac{\sigma_{em} I_L \tau}{h\nu_L}} \right) \tag{2-7}$$

Of course, if the Cr^{2+} ground state is substantially bleached, then this step is not justified, and (2-6) must be used instead.

The expression for gain coefficient can be expressed in more convenient terms by invoking the definition of saturation intensity and expressing the pumping rate of the excited state in terms of absorbed pump power. The saturation intensity I_{sat} is defined as the light intensity at the peak emission wavelength that stimulates enough emission to reduce the gain coefficient by a factor of two – a useful measure of the magnitude of the optical field produced in a laser[20] The saturation intensity can be determined from (2-6) or (2-7).

$$I_{sat} = \frac{h\nu_L}{\sigma_{em} \tau} \tag{2-8}$$

The term $N_1 \sigma_{abs} I_p$ in (2-6) or $N \sigma_{abs} I_p$ in (2-7) can be expressed as absorbed pump power P_{abs} per unit volume V in the gain material:

$$\frac{P_{abs}}{V} = N_1 \sigma_{abs} I_p \approx N \sigma_{abs} I_p \tag{2-9}$$

The expression becomes:

$$\gamma = \frac{\sigma_{em} P_{abs}}{V h \nu_p} \tau \left(\frac{1}{1 + \frac{I_L}{I_{sat}}} \right) \tag{2-10}$$

If there is little stimulated emission, then the gain coefficient is unsaturated and is called the "small signal gain coefficient", γ_0.

$$\gamma_0 = \frac{P_{abs}}{Vh\nu_p}\sigma_{em}\tau \tag{2-11}$$

As stimulated emission is simply the inverse process of absorption, a beam of light experiencing optical gain inside the laser material is amplified exponentially according the following expression:

$$I_{out} = I_{in}e^{\gamma_g} \tag{2-12}$$

where I_{out} is the light intensity after traveling through the laser material, I_{in} is the incident light intensity, γ is the optical gain coefficient, and l_g is the length of the path the light traveled inside the laser material. Now that expressions of the saturation intensity and small signal gain coefficient have been developed, the laser cavity model can be built.

2.2.2 Laser Dynamics Model

The laser dynamics model is just a simple one-dimensional simulation useful in predicting the pump intensity level required to produce laser output and the output efficiency expected. For simplicity, it is assumed that the laser resonator is stable and produces good transverse overlap between the resonated light and the pumped volume in the laser material. If those conditions are satisfied, this model does a fairly good job of predicting laser performance.

The laser to be modeled is a simple, end-pumped standing wave laser, as it is convenient to model and has been widely used in the literature (and in this research) for Cr^{2+} laser demonstration. This laser consists of the laser material (with optical gain) placed between two mirrors creating an optical resonator. One of the mirrors is highly

reflective, and the other is partially reflective to let a fraction of the resonated light out in a single beam (the laser output). The model is only one-dimensional, as it completely ignores transverse variations for simplicity: area is simply factored out of all the equations, leaving optical power measured in terms of intensity (W/m^2). A schematic of the laser cavity is shown in Figure 2-3:

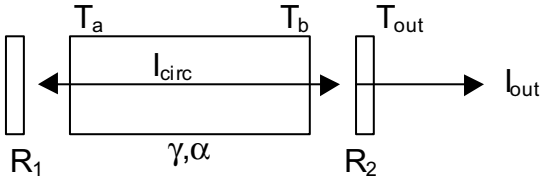

Figure 2-3 Standing Wave Laser Cavity For Laser Model

where R_1 and R_2 are mirror reflectivities, T_a and T_b account for laser rod surface transmission, T_{out} is the transmission through the output coupler ($T_{out}=1-R_2$), I_{circ} is the circulating optical field intensity inside the cavity, I_{out} is the output intensity of the laser, γ is the optical gain coefficient of the laser material, and α is the optical loss coefficient of the laser material.

The laser material has to be excited by a pump source of sufficient intensity to produce optical gain greater than the resonator loss to produce output power. The condition at which the round-trip optical gain equals loss is called the laser threshold. The gain at threshold γ_{rh} can be derived from the threshold condition:

$$R_1 R_2 T_a^2 T_b^2 e^{2l_g(\gamma_{th}-\alpha)} = 1 \tag{2-13}$$

Manipulating the expression to solve for the laser threshold gain γ_{th} yields:

$$\gamma_{th} = \frac{1}{2l_g}\ln\left(\frac{1}{R_1 R_2 T_a^2 T_b^2}\right) + \alpha \tag{2-14}$$

If the laser rod is pumped with enough power that the small signal gain is higher than the laser threshold gain, the laser will operate. The intracavity optical field I_{circ} will increase to the point where the stimulated emission rate increases the depopulation rate of the excited state enough to reduce the excited state population and thus the optical gain back to the threshold value. Once the excited state population has been "saturated" back to the threshold value, the optical gain for the circulating intensity is equal to the loss, and the laser reaches a dynamic equilibrium. One can estimate the output power of the laser by solving for the circulating intensity that it takes to saturate the small signal gain back to the threshold gain value.

$$I_{circ} = I_{sat}\left(\frac{\gamma_0}{\gamma_{th}} - 1\right) \tag{2-15}$$

In the standing wave laser cavity, I_{circ} is composed of forward and backward propagating optical fields (I_F and I_B) which both experience gain from the laser rod.

$$I_{circ} = I_F + I_B \tag{2-16}$$

Unfortunately for modeling, the two fields have different intensities, as most useful resonators are designed to out-couple light from one mirror only. Thus, the field traveling towards the partially transmissive output mirror will have higher intensity than the one traveling away from the output mirror. If the round-trip cavity loss is low, it is reasonable to approximate both fields as the same amplitude (tacitly assuming then that all loss is evenly distributed throughout the gain medium).

$$I_{circ} = 2I_F = 2I_B \tag{2-17}$$

The actual output power of the laser is then just the percentage of the field traveling towards the output coupler that leaves the cavity:

$$I_{out} = \frac{I_{circ}}{2} T_b T_{out} = \frac{I_{sat}}{2} T_b T_{out} \left(\frac{\gamma_0}{\gamma_{th}} - 1 \right) \tag{2-18}$$

Expressed in terms of absorbed pump power P_{abs}, and threshold pump power P_{th}, the expression for the laser output intensity is:

$$\begin{aligned} I_{out} &= \frac{I_{sat}}{2} T_b T_{out} \left(\frac{P_{abs} \sigma_{em} \tau}{\gamma_{th} V h \nu_p} - 1 \right) = \frac{\nu_L}{\nu_P} \frac{T_b T_{out}}{\ln\left(\frac{1}{R_1 R_2 T_a^2 T_b^2} \right)} \frac{L_g}{V} \left(P_{abs} - P_{th} \right) \\ P_{th} &= I_{sat} \frac{\nu_P}{\nu_L} \frac{V}{2 L_g} \ln\left(\frac{1}{R_1 R_2 T_a^2 T_b^2} \right) \end{aligned} \tag{2-19}$$

Simplifying the output expression by lumping the photon energy ratio and output coupling efficiency ratio into a single "slope efficiency" parameter η_{slope} produces expressions for laser threshold and output intensity that are commonly used in experimental laser work.

$$I_{out} = \eta_{slope} \left(I_{abs} - I_{th} \right) \tag{2-20}$$

$$\eta_{slope} = \frac{\nu_L}{\nu_P} \frac{T_b T_{out}}{\ln\left(\frac{1}{R_1 R_2 T_a^2 T_b^2} \right)} \tag{2-21}$$

$$I_{th} = \frac{I_{sat}}{2} \frac{\nu_P}{\nu_L} \ln\left(\frac{1}{R_1 R_2 T_a^2 T_b^2} \right) \tag{2-22}$$

These expressions are good for semi-quantitative analysis of CW and quasi-CW laser dynamics, for low loss cavities. However, the results of this model will tend to

underestimate the efficiency of the laser, due to the varying axial intensity of the optical fields inside an actual standing wave resonator. In a real laser, since the optical field has highest amplitude right before the output mirror (in efficient lasers), the ratio of photons coupled out of the resonator to the total number of photons lost in one round trip will be higher than this model predicts. Accounting for the non-uniformly distributed losses requires a more lengthy derivation[20]. The expression for the output intensity as a function of gain, assuming non-uniform losses, is:

$$I_{out} \cong I_{sat} \frac{T_2 T_{out}}{2} \left(\frac{\gamma_0 l_g - \frac{1}{2} \ln\left(1/R_1 R_2 T_a^2 T_b^2\right)}{\left(1-\sqrt{R_1 R_2 T_a^2 T_b^2}\right)\left(1+\sqrt{T_b^2 R_2 / T_a^2 R_2}\right)} \right) \tag{2-23}$$

Now that the expressions for output power vs. input power have been determined, the simple one-dimensional dynamics model can be compared with laser demonstrations from the literature. The performance of two Cr^{2+}:ZnSe laser experiments obtained from the literature are compared to the model in Table 2-3, using (2-23).

Table 2-3 Comparison of Published Results to Modeling Predictions

Demonstration	Mond et al[8]	Wagner et al[21]
Laser Material	Cr:ZnSe	Cr:ZnSe
Pump wavelength	2.01 μm	1.94 μm
Emission wavelength	2.5 μm	2.4 μm
Output Coupling (T_2)	13.4%	7%
Loss (Other than T_2)	2.5%	2-4%
Threshold	420 W/cm^2	450 W/cm^2
Slope Efficiency	73%	63%
Threshold Predicted by Model	**1400 W/cm^2**	**680 W/cm^2**
Slope Efficiency Predicted by Model	**68.5%**	**60%**

Taking a look at the modeling results in Table 2-3, it appears that the simple 1-D model does arrive at the correct order of magnitude, but does not exactly agree with the experimental results. Notice, however, that the published results do not agree with each other any more closely than they do with the model. Although there is not a close correspondence between the model and the results of laser experiments in the literature, the level of agreement is sufficient for feasibility analysis or semi-quantitative predictions of laser efficiency and output power. The less-than-perfect accuracy of this model is not surprising. Threshold predictions are particularly vulnerable to errors in measured quantities such as beam diameter, cavity loss, excited state lifetime, and the peak power of the pump laser. Slope efficiency is more robust, being dependent mainly on good transverse overlap between the gain region in the laser rod and the resonant cavity mode and the ratio of cavity loss to output coupler transmission. If these parameters are not well known, then the laser model is useful mainly as a design tool to estimate laser threshold intensity order of magnitude as a starting point for laser experiments. If, on the other hand, the mode overlap is good and the cavity loss, output laser wavelength, transmission of the output coupling mirror, and Cr^{2+} excited state lifetime are known, then the model will be more useful for quantitative prediction of laser performance.

A look at the experimental results in Table 2-3 indicates that with the very best laser crystals (as used in these demonstrations), threshold intensities of 450 W/cm^2 can be expected and slope efficiencies in the 60%-70% range can be achieved. Judging from the modeling results, the Cr^{2+}:ZnSe samples used in those experiments had to be very low loss with little nonradiative decay at room temperature to achieve such low thresholds.

Apparently it is possible to obtain very high quality Cr^{2+}:ZnSe samples – good news for the intended high power Cr^{2+} laser research effort.

Although the modeling presented here is only semi-quantitative, it performs surprisingly well in predicting the performance of actual Cr^{2+} laser demonstrations, given the level of approximations used to arrive at the results. It appears that the Cr^{2+} laser, at least with the ZnSe host, does indeed act like a four-level laser, and it is reasonable to use the simple dynamics model to estimate the theoretical best performance of a given laser design. Thus, the model can be used to investigate the feasibility of power scaling designs, as long as the results are taken with the proverbial grain of salt, and the laser designs should prove stable and produce reasonable mode overlap.

2.2.3 Analysis of Laser Stability and Mode Overlap

The predictions of the one-dimensional laser dynamics model discussed in the previous section rely on two assumptions which are not guaranteed to be valid in general for a real optical system with mirrors and gain elements: namely cavity stability and good mode overlap.

Stability in an optical cavity simply means that a confined optical field can exist inside the cavity. This confined optical field is called a cavity mode. The condition required for cavity-mode existence is self-consistency: the optical field after a round trip through the cavity should be identical to the original optical field in phase distribution and identical in intensity distribution within a multiplicative constant. Determination of cavity stability is thus a determination of the existence of a cavity mode for the particular optical cavity under investigation, and is not concerned with optical gain or loss.

Mode overlap is simply the degree to which the optical field of the cavity mode overlaps the volume in the laser material with gain (the pumped volume). Pumped areas in the laser material that are not overlapped by the cavity mode represent wasted power from the pump source. Mode overlap is determined by solving for the transverse intensity distribution of the cavity mode as a function of longitudinal position in the laser material, and comparing it to the shape of the absorbed pump intensity distribution (gain distribution) in the laser material.

Cavity stability and mode overlap are important considerations in laser design because cavity stability is necessary for the laser to operate, and poor mode overlap leads to unsaturated (unused) gain that represents wasted pump power and thus reduced laser efficiency. Making a mistake in cavity design that results in instability or poor mode overlap could be unfortunate for the Cr^{2+} laser demonstration. Analysis of optical cavity stability and predicted cavity mode size (for mode overlap calculations) are needed to supplement the one-dimensional model to aid in designing and analyzing the performance of real laser cavities.

The technique used in this research to determine cavity stability and mode overlap is the so-called ABCD method using the Gaussian complex beam parameter, described in laser textbooks such as *Laser Electronics*[20]. It is assumed that a Gaussian beam is the fundamental TEM_{00} mode of the laser cavity. The conditions for cavity stability are simply the conditions for the existence of the Gaussian mode. The existence and properties of Gaussian cavity modes can be calculated using simple ray-optics matrix

methods and the so-called ABCD law, which relates how ray optics matrices can be used to account for Gaussian beam propagation.

The first step in this procedure is to determine the ray optics matrix that describes a round trip through the optical cavity. Each optical element in the laser cavity is described by a 2x2 matrix. The effect of the beam going through two or more optics is handled by simply multiplying the matrix of the first optic by the matrix of the second optic, etc., with free space between optics having its own matrix representation. The round-trip through the optical resonator ends up being represented by a simple 2x2 matrix consisting of all the component matrices multiplied together.

$$M = \begin{bmatrix} A & B \\ C & D \end{bmatrix} \tag{2-24}$$

The next step is to apply the stability criterion. A Gaussian beam cavity mode exists if the following condition is satisfied:

$$\left| \frac{A+D}{2} \right| \leq 1 \tag{2-25}$$

As long as the cavity is stable, the cavity mode radius can be found at any point inside the resonator. This is done by calculating the ray-optics matrix for a round-trip through the resonator at the point of interest and using the following expression for the mode radius:

$$W = \left| \left[\frac{2\lambda B}{\pi \sqrt{4-(D+A)^2}} \right]^{\frac{1}{2}} \right| \tag{2-26}$$

where W is the mode radius, A, and D are ray-optics matrix elements, and λ is the wavelength of the light in the cavity.

Mode overlap is determined by simply calculating the mode radius in the laser rod and comparing it with that of the gain region. It will be assumed that the cavity mode is aligned with the gain region in the transverse plane, so a comparison of mode radius to gain region radius is meaningful. In long laser rods, the radius of the resonator mode or gain region might change significantly as a function of longitudinal position in the laser rod. However, this is not the case for the short laser rods of high index Cr^{2+}:II-VI laser materials considered in this research.

Interpretation of stability is quite simple: the laser cavity produces output when it is stable, and does not when the cavity is unstable. The interpretation of mode overlap is not so simple, as there is considerably more going on with cavity mode structure than this model considers.

In this research, mode overlap calculations were used for laser design purposes as a qualitative indicator of what kind of performance would result in the Cr^{2+} laser for a given optical cavity. There were three qualitative kinds of mode overlap with different consequences for laser efficiency:

1. **$W_{mode} = W_{gain}$:** If the radius of the cavity mode were the same as that of the gain region, throughout the laser material, then most likely the efficiency of the laser would be highest: close to that of the ideal case assumed in the dynamics model. The stable Gaussian mode would likely be a fairly accurate representation of the real laser cavity mode.

2. **$W_{mode} > W_{gain}$:** If the radius of the cavity mode were much larger than the radius of the gain region, then although laser efficiency should be high because all the gain would be saturated, the efficiency would be less than that predicted due to thermally-induced optical distortion present at the edge of the gain region in Cr^{2+} materials. In this case, the real laser cavity mode would be similar to the predicted Gaussian mode but somewhat distorted due to the thermal aberration that is not well represented as a spherical optical element. (See Section 6.5 and Chapter 1 for further discussion of thermal effects.)
3. **$W_{mode} < W_{gain}$:** If the radius of the cavity mode were much smaller than the radius of the gain region, then one of two things could happen: the efficiency of the laser would be significantly reduced due to the pump power wasted on the unused areas of the gain region, or multiple cavity modes would simultaneously be supported by the large gain region, preserving laser efficiency but increasing output beam divergence. The amount of mode selectivity of the resonator would determine which would happen.

Experience shows that the most efficient laser operation requires a TEM_{00} cavity mode radius ~ 50% - 100% of the gain region radius, producing at least slightly multi-mode output.

2.3 Power Scaling feasibility of the Cr^{2+}:II-VI Laser

Power scaling the Cr^{2+} laser (to the 5-W power level) was the main goal of this research. A review of Cr^{2+} power scaling experiments and effective high power laser designs was conducted to determine what resonator designs and Cr^{2+} materials were the

most likely to result in a successful power scaling demonstration. This section presents the highlights of that review, discussing Cr^{2+} laser designs found in the literature, design issues involved with the power scaling of Cr^{2+}:II-VI lasers, and the feasibility of several prospective resonator designs.

2.3.1 Cr^{2+} Power Scaling in the Literature

Although the literature shows many successful initial laser demonstrations of Cr^{2+}:II-VI materials, the laser cavities and crystal geometries used have all been very simple, suitable for initial laser demonstrations but not high power operation. Although power scaling has been attempted[5], more advanced resonator designs have not. The typical demonstration resonator used the end-pumped standing wave configuration with several watts of 2-μm pump power focused to a 40-80 μm radius in the laser rod. The laser cavity would be either a 4-mirror folded cavity or a simple 2-mirror hemispherical cavity, using short radius of curvature mirrors to achieve cavity stability. A representative schematic is shown in Figure 2-4 for a low power 4-mirror folded cavity Cr^{2+}:ZnSe laser demonstration[13]. These designs work well at low pump power levels, and indeed require only a few tenths of a watt absorbed power in a 40-μm radius beam to reach laser threshold[21]. However, neither of these designs can tolerate the high degree of thermal lensing present in heavily pumped Cr^{2+}:II-VI materials, and thus so far only low power has been demonstrated.

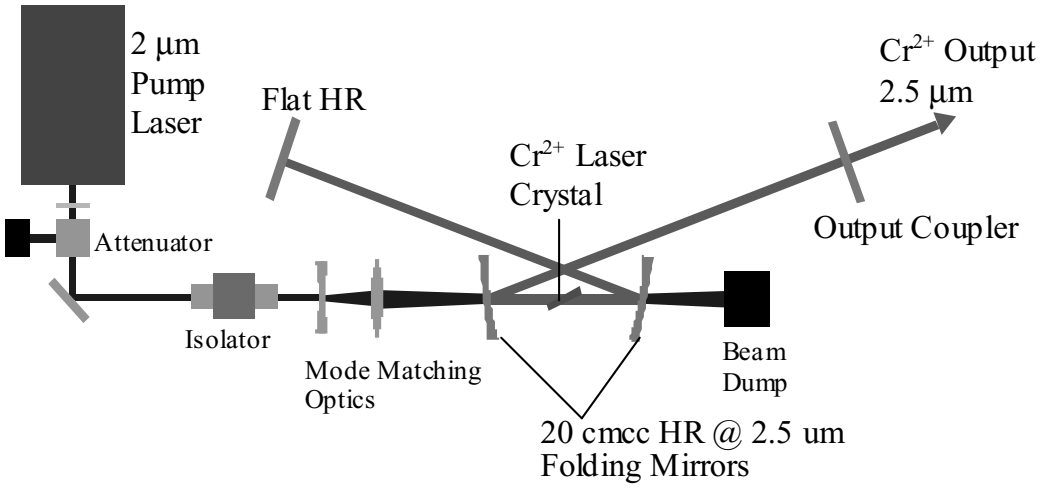

Figure 2-4. Typical Configuration for Low Power Cr^{2+}:II-VI Laser Demonstrations (4 Mirror Standing Wave Cavity with 2-µm Pump and Cr^{2+}:ZnSe Material)

2.3.2 Cr^{2+}:II-VI Power Scaling Issues

For the Cr^{2+}:II-VI laser, the material properties and laser demonstrations suggest that the likely power scaling issues are thermal lensing, increased nonradiative decay at elevated crystal temperatures, the low Cr^{2+} doping density, and damage. These issues are interrelated, as thermal distortion can lead to damage, increased nonradiative decay leads to increased heating, etc. The overall result is that Cr^{2+} laser design for high power operation is an exercise in engineering tradeoffs and designing around simultaneous constraints.

Thermal lensing appears to be the Achilles heel of the Cr^{2+}:II-VI materials. Output power of end-pumped Cr^{2+} lasers has been limited to the 2-watt level by severe thermal lensing. The high brightness pumping needed with 5-8 µs lifetime Cr^{2+} materials combined with their high dn/dT, creates large thermally induced refractive index changes

in the pumped region of the gain material. Standard end-pumped CW Cr^{2+} lasers can expect thermal lensing focal lengths of 4 cm or less, when operating at 4 times threshold in a low loss cavity, based on a standard thermal lensing model[18] and recent Cr^{2+}:ZnSe thermal lensing measurements[5]. Scaling laser power beyond 2 W requires an alternative resonator design.

Increased nonradiative decay of the Cr^{2+} excited state at elevated temperatures has been reported in the literature[1] and should result in reduced laser efficiency at operating temperatures greater than about 300 K. This sets limits on Cr^{2+}:II-VI operating temperature for efficient laser operation.

Cr^{2+} doping in II-VI materials is limited to ~$2x10^{19}$ cm^{-3} or less due to the onset of significant emission quenching and optical loss at greater doping levels[13, 22]. The low Cr^{2+} doping density in II-VI materials affects power scaling efforts by requiring a pump absorption path of 2 mm or more, and raises the possibility that the pump absorption could be saturated (bleached), resulting in inefficient pump absorption, especially for pulsed excitation. In addition, high energy Q-switched operation is out of the question, as the Cr^{2+}:II-VI material cannot store enough energy.

The damage threshold of II-VI materials is approximately 100kW/cm^2 for CW light and ~ 2 J/cm^2 for pulsed light. A CW intensity in the 100 kW/cm^2 range should never be required in Cr^{2+} lasers, so CW damage should only occur if a surface were already compromised (dirty, or bad coating). The main risk for CW damage is thermal fracture caused by a temperature gradient that is too steep. This will occur for absorbed pump intensities considerably less than 100 kW/cm^2. Damage during pulsed operation could

easily occur if the damage threshold were exceeded, which corresponds to ~ 16 mJ in a 1-mm diameter beam. IR coatings vary widely in pulsed damage threshold, so considerable variation in pulsed damage threshold is expected. Avoiding damage entails proper management of heat transfer in the laser rod to avoid thermal fracture, keeping the surfaces clean and scratch free, obtaining high damage threshold coatings, and avoiding small beam diameters in the laser material during pulsed operation.

In summary, significant issues have to be considered when power scaling the Cr^{2+} laser. First, thermal lensing appears to be so strong that the resonator must be designed to mitigate or accommodate it. Second, active cooling is required to prevent excessive non-radiative relaxation. Finally, Cr^{2+} doping considerations and damage limits force resonator designs to consider large diameter beams and laser designs with long pump absorption paths. Of these issues, by far the most significant is the thermal lensing. The simple bulk end-pumped resonator can't deal with so much thermal lensing, especially given all the other simultaneous constraints. A different resonator design that can handle or mitigate severe thermal lensing is needed to enable successful power scaling of the Cr^{2+}:II-VI laser to the 5-W level.

2.3.3 Resonator Designs for Power Scaling

The biggest obstacle to power scaling the Cr^{2+}:II-VI laser is thermal lensing. Therefore, resonator designs which mitigate thermal lensing are prime candidates for use in power scaling the Cr^{2+}:II-VI laser. Many resonator designs that mitigate thermal effects are found in the literature. The basic design categories are the optical fiber laser, the zig-zag slab laser, the waveguide laser, and the thin disk laser. Of these, only the slab

and thin disk laser designs are currently feasible, as Cr^{2+}-doped II-VI optical fiber and low loss 2-3 μm waveguides are not available.

The zig-zag slab laser consists of a rectangular slab that is edge pumped, face cooled, and shaped so that the resonated light bounces off the faces of the slab in a zig-zag path, averaging the effects of thermal gradients in the plane of the path of the resonated light[18]. This greatly reduces the effects of thermal gradients on the resonator. The slab laser is an effective design for power scaling to the stress fracture limit of a given laser material, but poor coupling efficiency and the large amount of pump laser power needed for reasonable slab sizes make the slab laser not attractive for a 5-20 W Cr^{2+} laser. For example, a 1-mm x 3-mm cross section zig-zag slab, pumped transversely, would need a total of 75 W of pump power in the slab to reach 4 times threshold, yielding 27-W output. This assumes that a very optimistic 80% absorption efficiency, 500 W/cm^2 laser threshold and 60% slope efficiency applicable to the end-pumped laser demonstrations still hold for a side-pumped slab laser. This also assumes that 75 W of pump power was available for pumping the Cr^{2+} laser. In this research, 20 W was the maximum available pump power, barely enough to reach laser threshold.

A slab with smaller transverse area is needed to reduce laser threshold, if the slab geometry is to be used in the 5-W Cr^{2+} laser demonstration. However, only the thickness of the slab can be reduced, because the 3-mm slab width is needed for effective absorption of the pump laser light. Keeping the slab width at 3 mm while reducing the slab thickness below 1 mm raises coupling efficiency and beam quality issues. It is difficult to effectively couple the energy from such a non-radially symmetric gain region

into a TEM_{00} cavity mode that can produce a low divergence, round output beam. Given a 20-W limitation in pump power, the slab design is not suitable. If a 75-W pump laser, or better yet, a 75 W, 1.9-μm diode laser stack became available, the slab laser design might be an attractive option.

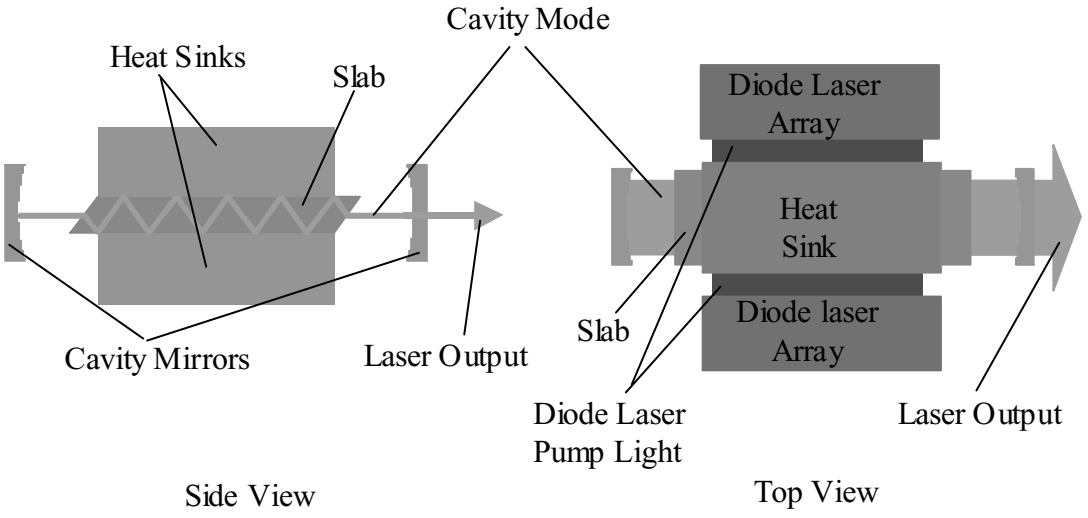

Figure 2-5. Schematics of Side and Top Views of the Zig-Zag Slab Laser Concept The slab is rectangular in cross section and has Brewster surfaces on the ends for high efficiency transmission of the resonated light. Pumping is from the side, ideally from high power diode laser arrays, and cooling is provided by heat sinks on the top and bottom surfaces of the slab. The resonated light travels in a zig-zag path that averages out the effects of the refractive index gradient associated with the primary thermal gradient in the slab, thus mitigating thermal lensing.

The thin disk laser, on the other hand, has been shown to scale up to kW output power (with Yb:YAG), just like the slab laser, but can retain high efficiency at low power as well[23]. The thin disk laser is essentially an end-pumped rod laser that uses a face-cooled laser rod with a large ratio of diameter to thickness. One face is anti-reflection (AR) coated and the other face is high-reflection (HR) coated and mounted on a heat sink for cooling. The thin disk acts both as the gain element and as a mirror of the optical

cavity. Pumping is done through the AR face, at an angle to avoid the use of extra dichroic mirrors in the resonator. The thin disk geometry minimizes radial thermal gradients and thus reduces thermal lensing to manageable levels. If the transverse intensity distribution of the input pump laser is uniform, (a 'top-hat' beam), the thermal lensing in the laser disk will be even lower.

As long as the disk is thin enough, the desired output power can be adjusted by changing the size of the pumped area on the disk. A 0.25-mm thick disk should allow operation of modes with diameter > 0.5 mm with only weak thermal lensing. (The larger the ratio of pumped diameter to disk thickness, the lower the amount of thermal lensing for a constant absorbed intensity.) Operating at 4 times threshold and assuming a 500 W/cm^2 threshold, 80% absorption efficiency and 60% slope efficiency, a 1-mm pumped diameter requires 20-W pump power to reach 4 times threshold and results in 7-W output power with an overall efficiency of 35%. Given the good coupling efficiency provided by this end-pumped configuration, these estimates should be fairly reasonable. The thin disk laser is therefore likely to be considerably more efficient than a slab laser, at least for low-medium power TEM_{00} applications.

However, there is a difficulty with the thin disk laser design: absorbing the pump power efficiently. Cr^{2+} doping levels are limited by scattering and high nonradiative relaxation rates[13]. To effectively absorb the pump power in a 0.25-mm thick disk, a Cr^{2+} doping concentration of at least 10^{19} cm^{-3} and a multiple-pass pumping system with eight or more passes are needed, thus complicating the laser design. In addition, the transverse absorbed power density in the laser disk must be as uniform as possible,

requiring a 'top-hat' pump beam in the ideal case. However, the added system complexity of the thin disk laser is a small price to pay for mitigation of the thermal effects which have so far hindered the power scaling of the Cr^{2+} laser.

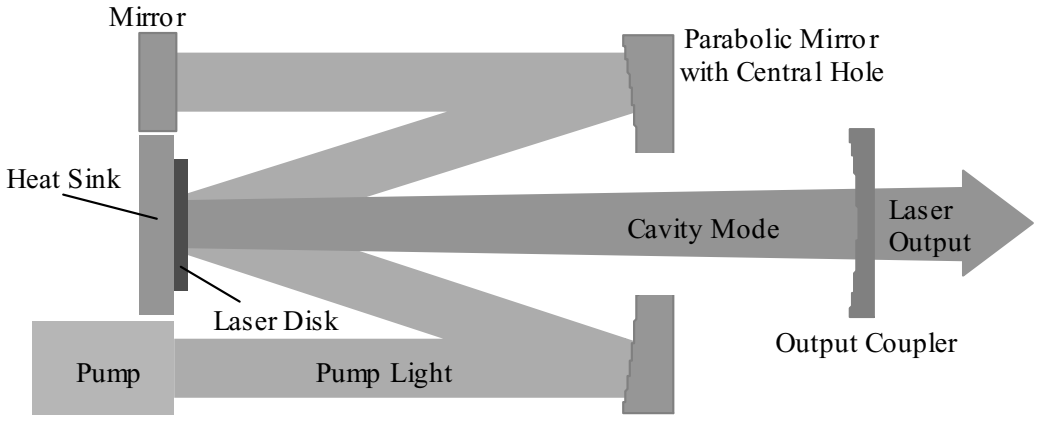

Figure 2-6. Thin Disk Laser
The disk is mirror coated on the rear surface and mounted on a heat sink. Since the disk is thin, the pump laser beam has to be passed through the disk many times to achieve adequate pump absorption. Off axis pumping is used to minimize cavity loss for the resonated light. If the pump has uniform transverse intensity distribution, and has diameter at least four to six times the disk thickness, thermal gradients in the laser disk will be predominantly longitudinal, significantly reducing thermal lensing.

2.3.4 Summary of Cr^{2+} Laser Power Scaling Feasibility

It should be possible to produce a 5-W Cr^{2+}:II-VI laser if a resonator design is used that considerably reduces thermal lensing and pump laser power of 20 W or more is available. Of the typical laser geometries suitable for high power Cr^{2+} laser design, the thin disk laser design is the most attractive option available for the demonstration of a 5-10 watt Cr^{2+} laser. The additional pumping optics required in the thin disk laser

geometry are more than offset by the mitigation of thermal lensing and efficient operation at powers unobtainable with end-pumped rod designs.

3 Material Characterization

This chapter presents spectroscopic experiments to investigate maximum Cr^{2+} doping concentrations for useful laser material, the temperature dependence of Cr^{2+} fluorescence lifetimes in different materials; stimulated emission cross section values and bandwidths, estimated thermal loading under lasing and non-lasing conditions, and broadband tuning of a Cr^{2+}:CdSe laser to verify optical gain estimates at long wavelengths. These experiments were conducted over quite some time, using a variety of Cr^{2+} samples and pump laser configurations. These variations make quantitative extrapolation somewhat questionable, but the qualitative trends and conclusions obtained have proven invaluable in understanding the Cr^{2+} laser and laser design considerations.

3.1 Determination of Maximum Cr^{2+} Doping Level

The disk laser approach to power scaling the chromium laser involves making the laser crystal as thin as possible, to minimize overall passive loss due to the unavoidable scattering in the materials, and to aid in heat removal. The thinner the laser material, the higher the dopant concentration needs to be to ensure adequate absorption efficiency of the pump laser, through providing both a high absorption coefficient and enough Cr^{2+} ions to prevent bleaching. The Cr^{2+}-II-VI laser crystals used in bulk end-pumped laser experiments reported in the literature had $< 10^{19}$ cm^{-3} Cr^{2+} concentration and thus required pump absorption path lengths longer than 2 mm to ensure efficient utilization of the pump laser. Cr^{2+} doping-level in laser disks would thus have to be higher than that of the typical bulk material to enable the disks to be thin. Unfortunately, a survey of existing Cr^{2+}:II-VI samples in the lab indicated that crystals doped with too much Cr^{2+}

tended to exhibit reduced excited state lifetime, likely due to nonradiative decay processes. The maximum chromium concentration in CdSe or ZnSe that would still result in good laser material needed to be determined.

An experiment was conducted to determine the effect of high doping on Cr^{2+} excited state lifetime in Cr^{2+}:ZnSe and Cr^{2+}:CdSe, two of the most promising Cr^{2+}:II-VI laser materials. Diffusion-doped samples of Cr^{2+}:CdSe and Cr^{2+}:ZnSe were obtained, respectively from Cleveland Crystals and Spectragen, with the highest Cr^{2+} concentration available in each respective material, and were tested for quenching of fluorescence which coincides with high Cr^{2+} doping. The Cr^{2+}:CdSe sample was a 4-mm thick block, anti-reflection coated on two faces. The Cr^{2+}:ZnSe sample was an uncoated 1-mm thick slab, later coated and used in the disk laser power scaling experiment. A Q-switched 2.06-μm Tm,Ho:YLF laser beam with 300-ns FWHM pulses pumped the samples. Cr^{2+} absorption was measured with a power meter and fluorescence decay time constant was measured simultaneously with a fast InGaAsP photodiode and an oscilloscope. Since the diffusion and polishing processes used in sample fabrication resulted in transverse chromium-concentration gradients across the samples, translation of the samples across the laser beam provided access to different Cr^{2+} concentrations. The results are shown in Figure 3-1 and Figure 3-2.

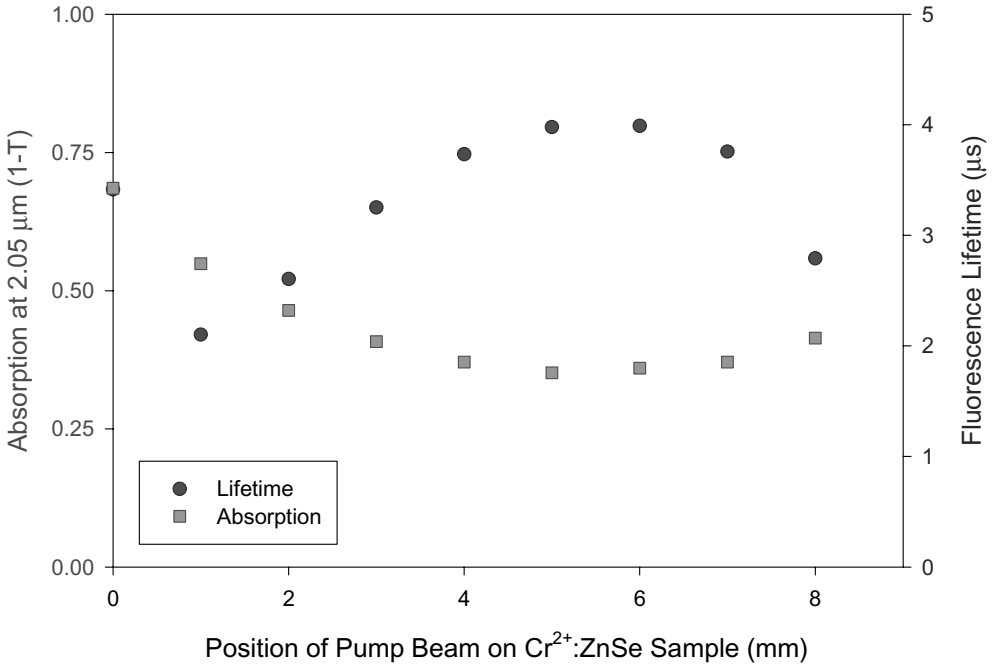

Figure 3-1. Pump Absorption and Cr^{2+} Fluorescence Lifetime Measurements in 1-mm Thick Cr^{2+}:ZnSe Sample as a Function of Pump Beam Position

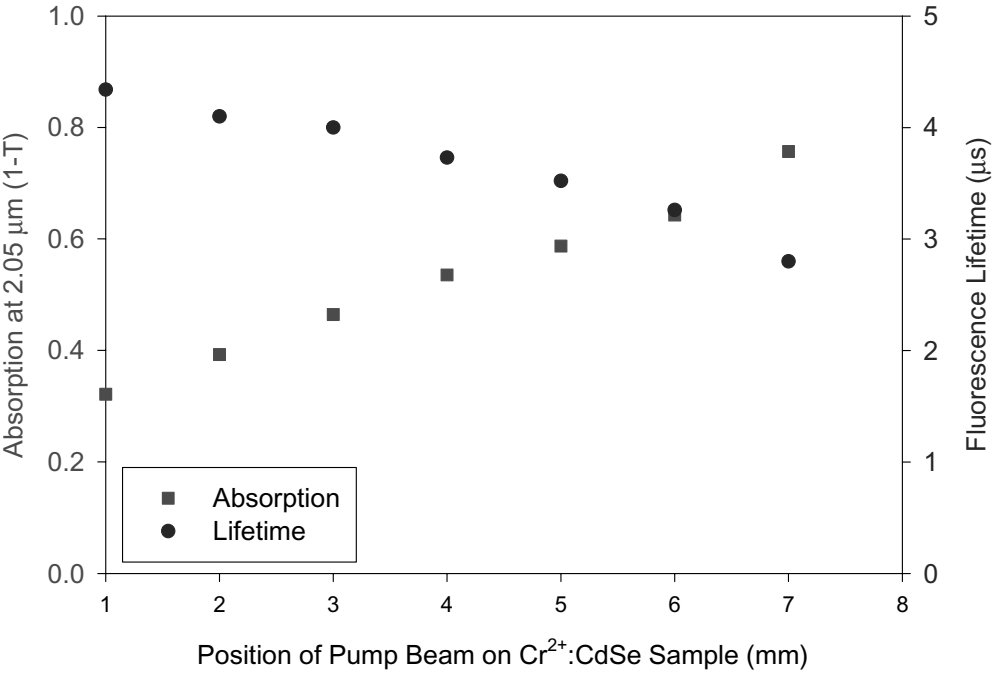

Figure 3-2. Pump Absorption and Cr^{2+} Fluorescence Lifetime Measurements in 4-mm Thick Cr^{2+}:CdSe Sample as a Function of Pump Beam Position

Qualitatively, the samples showed a negative correlation between pump absorption and excited state lifetime. In the areas with the most pump absorption, fluorescence lifetimes were reduced by more than a factor of two compared with data obtained from other samples having lower Cr^{2+} doping. Such reduced excited state lifetimes could significantly impair Cr^{2+} laser efficiency in pulsed operation, and raise Cr^{2+} laser thresholds to unacceptably high levels in CW operation.

But what were the actual Cr^{2+} concentrations in the samples? Unfortunately, that determination is difficult. Small, pulsed beams had to be used to obtain accurate lifetime data, which led to intense localized pumping intensity. The result was that the Cr^{2+} absorption was partially bleached for both samples in the experiment. In other words, the population density of Cr^{2+} ions in the ground state was not independent of pump input power. Estimates of Cr^{2+} concentration using the absorption cross section and Beer's Law assuming constant ground-state population would not be accurate. This also raises the question of how accurate the published values of absorption and emission cross sections are. Calculations using published cross section values and the assumption that bleaching is negligible resulted in estimated Cr^{2+} concentration values of 0.4×10^{18} cm^{-3} to 1.4×10^{18} cm^{-3} for Cr^{2+}:CdSe, and15×10^{18} cm^{-3} to 40×10^{18} cm^{-3} for Cr^{2+}:ZnSe. However, the input pump intensity was ~70 μJ per pulse in a 90-μm radius beam, resulting in approximately 7×10^{14} photons illuminating the pumped volume. According to the calculations, even the highly doped Cr^{2+}:ZnSe piece did not have more than 10^{15} Cr^{2+} ions in the pumped volume. Thus, the concentration values calculated assuming negligible bleaching are inaccurate.

In theory, it is possible to estimate Cr^{2+} concentration and absorption cross section through measurement of absorption saturation as a function of input light intensity, as the varying transmission renders both dopant concentration and absorption cross section observable. In this research, the process of bleaching a saturable absorber was simulated numerically in Matlab and run for the experimental conditions (using published absorption cross section values) to provide an estimate of Cr^{2+} concentration. Simultaneous estimation of absorption cross section and Cr^{2+} concentration was not done, as it required much more extensive data taking and control over experimental parameters, making it outside the scope of this research.

The simulation used the finite-element approach, breaking down the Cr^{2+}:II-VI material into a three dimensional grid of elements with independently tracked Cr^{2+} ground state populations. A Q-switched laser pulse was modeled as a series of smaller pulses, each of which having low enough energy that Beer's Law was a valid model for absorption. The simulation sent each component pulse through the laser material, calculated how many photons were absorbed in each element, and then updated the Cr^{2+} ground state population values to account for the absorption. This was repeated for all the component pulses. Comparing the total number of photons absorbed to the total number of incident photons in the laser pulse yielded transmission (or absorption) for a particular Q-switched pulse energy. This process was repeated for an array of input pulse energies, creating a curve that could be fit to experimental data by modifying simulation parameters.

Pertinent simulation parameters were 70-μJ incident energy per pulse at 2.06 μm, Gaussian pump-beam intensity distribution with 90-μm radius, uncoated 1-mm thick Cr^{2+}:ZnSe with pump absorption cross section of $2.9x10^{-19}$ cm^2, and 4-mm thick anti-reflection coated Cr^{2+}:CdSe with pump absorption cross section of $2.25x10^{-18}$ cm^2. The absorption cross section values at the 2.06-μm pump laser wavelength were calculated using published peak cross section values of $0.87x10^{-18}$ cm^2 for Cr^{2+}:ZnSe[11] and $3x10^{-18}$ cm^2 for Cr^{2+}:CdSe[2] and FTIR transmission curves. Note that using a 1.9-μm Tm:YLF pump laser would have resulted in higher absorption cross sections values for both materials, $0.67x10^{-18}$ cm^2 for Cr^{2+}:ZnSe and $3x10^{-18}$ cm^2 for Cr^{2+}:CdSe, but this laser was not available at the time of the experiment.

Applying the simulation to estimate Cr^{2+} concentrations from absorption data results in better estimates of Cr^{2+} concentration than those obtained under the assumption that bleaching is negligible. Using the simulation to estimate Cr^{2+} concentrations from the absorption data in Figure 3-1 and Figure 3-2 results in plots of fluorescence lifetime as a function of estimated Cr^{2+} concentration. These plots are shown in Figure 3-3 and Figure 3-4. The simulation produced estimated Cr^{2+} concentration values of $1.7x10^{18}$ cm^{-3} to $5.9x10^{18}$ cm^{-3} for the Cr^{2+}:CdSe sample, and $21x10^{18}$ cm^{-3} to $36x10^{18}$ cm^{-3} for the Cr^{2+}:ZnSe sample. Since published absorption cross section values were used, which have uncertainty of about a factor of two, the estimated Cr^{2+} concentrations have the same factor-of-two uncertainty. However, the fact that Cr^{2+}:ZnSe had considerably larger absorption coefficient than the Cr^{2+}:CdSe did makes Cr^{2+}:ZnSe appear more useful for laser applications requiring a short pump absorption path.

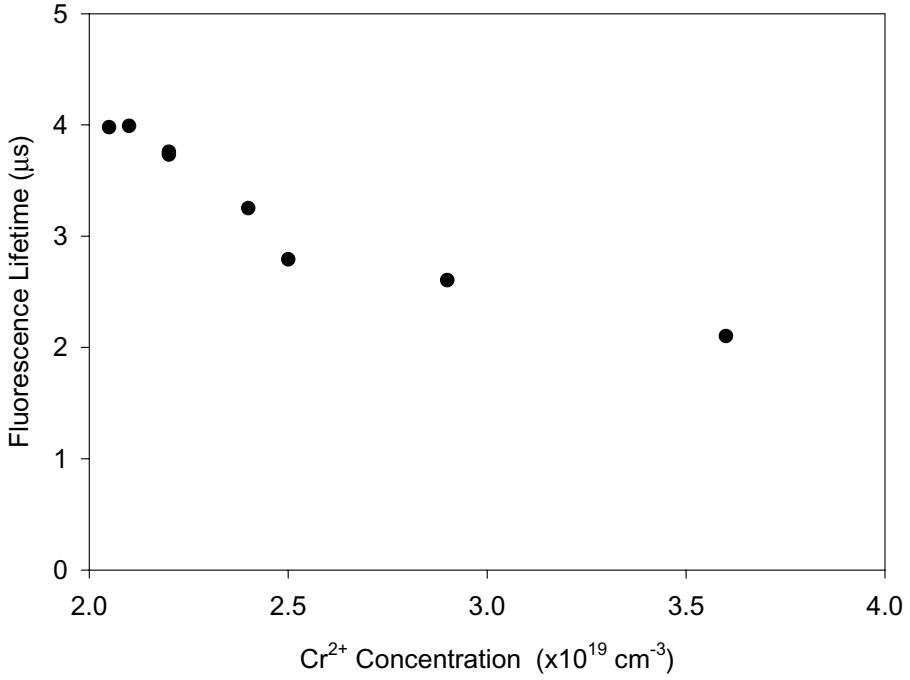

Figure 3-3. Cr^{2+} Fluorescence Lifetime vs. Estimated Cr^{2+} Concentration in 1-mm Thick Cr^{2+}:ZnSe Sample (Using Saturable Absorber Simulation)

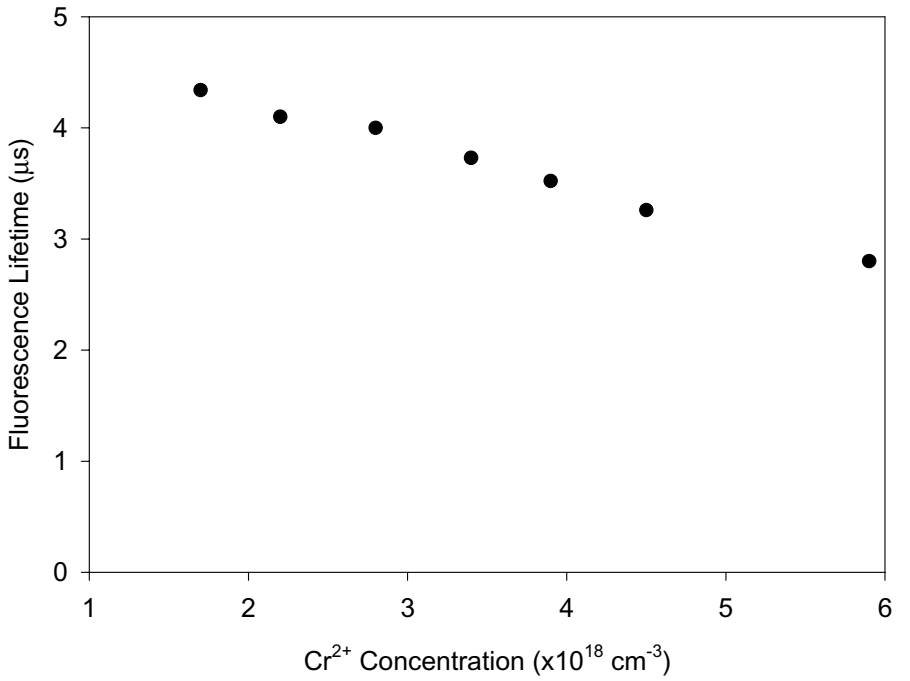

Figure 3-4. Cr^{2+} Fluorescence Lifetime vs. Estimated Cr^{2+} Concentration in 4-mm Thick Cr^{2+}:CdSe Sample (Using Saturable Absorber Simulation)

Using the low concentration lifetimes of 8 μs for Cr:ZnSe[1] and 6 μs for Cr:CdSe[2], it appears that Cr^{2+} concentrations of approximately $2x10^{19}$ cm^{-3} in ZnSe and $6x10^{18}$ cm^{-3} in CdSe should result in a similar lifetime reduction, assuming published absorption cross section values are accurate. This experiment shows that, at least for current doping methods, ZnSe allows a higher chromium concentration to be incorporated in a useful laser crystal – about a factor of three times more Cr^{2+} than CdSe will accept. Using these concentration values, a 0.25-mm thick Cr^{2+}:ZnSe disk would have 28% single-pass absorption at 1.9 μm and be capable of absorbing 52 mJ/cm^2. A similar disk of Cr^{2+}:CdSe would have 36% single-pass absorption at 1.9 μm and be capable of absorbing 16 mJ/cm^2. ZnSe thus appears to be the better host for Cr^{2+} in terms of energy storage.

3.2 Temperature Dependence of Excited State Lifetime

It has been known for years that Cr^{2+}-doped II-VI materials exhibit reduction of Cr^{2+} excited state lifetime at elevated temperatures[11]. An estimate of maximum advisable operating temperature for Cr^{2+} laser materials was needed for the power scaling design effort. Therefore, an experiment was conducted to measure the fluorescence lifetime of Cr^{2+} materials at different temperatures. A sample each of Cr^{2+}:CdSe, Cr^{2+}:ZnSe, and Cr^{2+}:CdMnTe were subjected to a temperature range of 15 K to 400 K while Cr^{2+} fluorescence lifetime was measured. A cryostat was used to produce temperatures below 290 K, and an oven was used to produce temperatures greater than 290 K. A fast InGaAsP photodiode and oscilloscope detected the Cr^{2+} fluorescence and a 1.9-μm Tm:YLF laser run at 500 Hz with 0.8 mJ, 300-ns FWHM pulses in a ~1-mm diameter

beam provided the excitation. Temperature was measured with a thermocouple attached to the copper block on which the samples were placed. The measured fluorescence intensity curves were fit with a generic exponential decay function to estimate decay time constant (lifetime). The results are shown in Figure 3-5.

Looking at the results, it is quite apparent that these samples showed decreased excited state lifetime at both low temperatures and high temperatures. The reason for the decrease in excited state lifetime below 200 K is not known, nor is it explained in the literature. The emission signal (not shown) of all three samples decreased only at the higher temperatures, indicating nonradiative processes became significant only at temperatures greater than about ~250-350 K. Increase in temperature above 290-300 K resulted in drastic reduction of excited state lifetime and emission strength for all three samples. For reference the absolute maximum Cr^{2+} excited state lifetimes measured under conditions of high fluorescence efficiency for these kinds of materials are 8 μs for Cr^{2+}:ZnSe[11], 6 μs for Cr^{2+}:CdSe[2], and 4-5 μs for Cr^{2+}:CdMnTe[3]. For this particular experiment, the Cr^{2+}:ZnSe sample exhibited the least reduction in lifetime at elevated temperatures. The Cr^{2+}:ZnSe sample exhibited a 4 μs lifetime at 350 K, corresponding to a 50% reduction in lifetime. The other two samples exhibited 50% reduction in Cr^{2+} excited state lifetime at 300 K: 3 μs for Cr^{2+}:CdSe and 2 μs Cr^{2+}:CdMnTe.

When considering this experiment, it needs to be realized that the results really cannot be interpreted quantitatively. The three samples had widely different volumes and contact areas on the thermal mass, making heat sink temperature a somewhat inadequate measure

of sample temperature for comparison purposes. In addition, since only sample of each material was available, the effects of sample-to-sample variation on the temperature dependence of lifetime could not be determined.

In designing a Cr^{2+} laser, temperatures of 350 K or more inside the Cr^{2+} laser material need to be strictly avoided, and every effort needs to be made to keep the temperature as low as possible. Cooling need not be carried to extremes, fortunately, because operating temperatures much below 270 K do not result in longer Cr^{2+} excited state lifetimes. The overall conclusion is that it would probably be best to put the Cr^{2+} gain cell in a nitrogen purged box and cool the laser material to about 270 K, to maximize laser efficiency and minimize CW laser threshold. However, room temperature operation may not incur significant penalties in efficiency, particularly for Cr^{2+}:ZnSe.

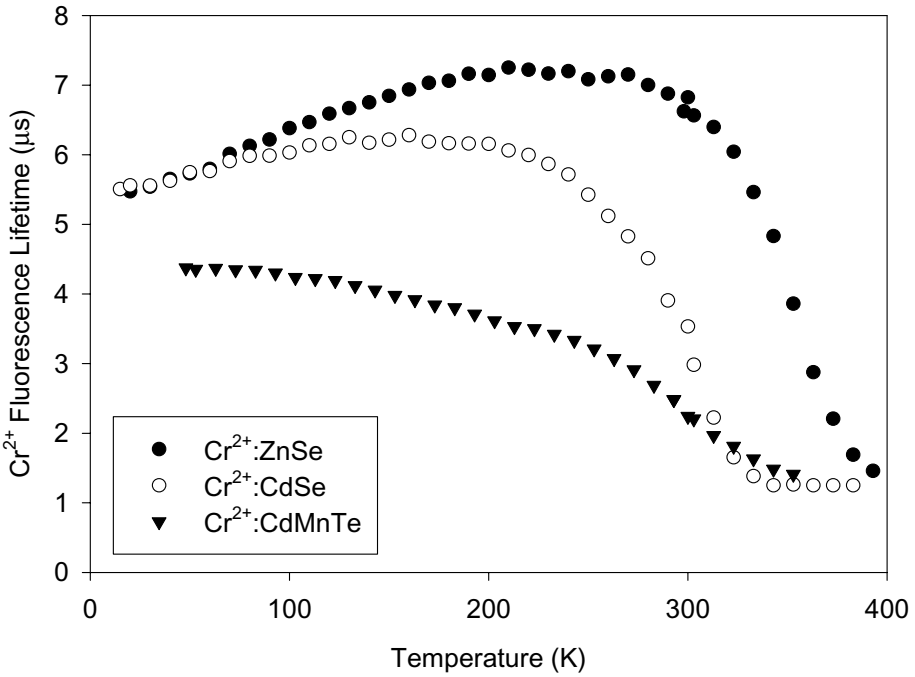

Figure 3-5. Estimated Cr^{2+} Fluorescence Lifetime vs. Cryostat Temperature

3.3 Cr^{2+} Stimulated Emission Cross Section Measurements

Emission spectroscopy of Cr^{2+}:CdSe and Cr^{2+}:ZnSe was performed with the goal of assessing feasibility of 3-4 μm laser operation. The experiment used a chopped 1-W CW Tm,Ho:YLF laser as the excitation source, a 15-cm monochromator with 300 g/mm grating for wavelength discrimination, and lock-in detection with a photo-conductive PbSe detector to detect fluorescence. The particular Cr^{2+} samples investigated were a 2-mm thick Cr^{2+}:ZnSe sample with ~7 μs fluorescence lifetime and a 4-mm thick Cr^{2+}:CdSe sample with ~3-5 μs fluorescence lifetime at room temperature. Fluorescence was detected over a range from 1.7 μm to 3.4 μm. Wavelength resolution was 20-nm FWHM using ¾-mm spectrometer slit width (required to maintain detector signal-to-noise ratio) – more than adequate to resolve broad Cr^{2+} absorption features. Raw emission spectra were calibrated for detector response and system transmission using a precision, variable temperature blackbody source as a reference. The following procedure was used for calibration and calculation of stimulated emission cross section:

1. The sample was pumped with the chopped Tm,Ho:YLF laser and Cr^{2+} fluorescence signal intensity *S* was recorded as a function of wavelength.
2. The blackbody source was operated at an appropriate temperature such that its power spectral density was negligible at wavelengths shorter than that of the Cr^{2+} fluorescence (to minimize "aliasing" effect of multiple diffracted orders getting through the grating instrument). The blackbody temperature that matched the best was 743 K. At this temperature, the blackbody radiation was negligible below 1.6 μm.

3. The Cr^{2+} fluorescence detection system recorded blackbody radiation signal intensity *R* as a function of wavelength.
4. The theoretical photon density for blackbody radiation *BB* was generated, using the set temperature of the blackbody source (743 K).
5. The fluorescence signal *S* was divided by the blackbody reference signal *R*, and this quotient was multiplied by the theoretical photon density for blackbody radiation *BB*, producing the photon number spectral density *F*. Since the data were taken as a function of wavelength, the result is photon number spectral density with units of fluorescence photon number per unit wavelength.

$$F(\lambda) = \frac{S(\lambda)}{R(\lambda)} BB(\lambda) \tag{3-1}$$

6. This photon number spectral density needed to be turned into a line-shape function. Therefore, it was normalized such that the integral of $F(\lambda)d\lambda$ was unity. The normalized fluorescence photon number per unit wavelength F_n could now be considered a lineshape function, and was used to determine stimulated emission cross section.

$$\sigma_{em} = \frac{A_{21}\lambda^4 F_n(\lambda)}{8\pi n^2 c} \tag{3-2}$$

The stimulated emission cross sections for Cr^{2+} in CdSe and ZnSe calculated by this method are shown in Figure 3-6. Note that the peak cross sections are similar, 10^{-18} cm^2, but the Cr^{2+}:CdSe emission extends to much longer wavelengths than that of Cr^{2+}:ZnSe, as far as 3.4 μm. (The increase in the Cr^{2+}:ZnSe cross section past 3 μm is a measurement

artifact due to second order diffraction of 1.5-1.7 μm fluorescence, magnified by the λ^4 factor in the cross section calculation.) It does not appear likely that Cr^{2+}:ZnSe would tune out past 3 μm without exceptionally intense pumping. Thus if tuning out past 3 μm is needed for the laser application, Cr^{2+}:ZnSe would not be suitable despite its superior thermal conductivity, strength, and Cr^{2+} doping density. A cadmium-based II-VI host like CdSe would be needed to access wavelengths longer than 3 μm.

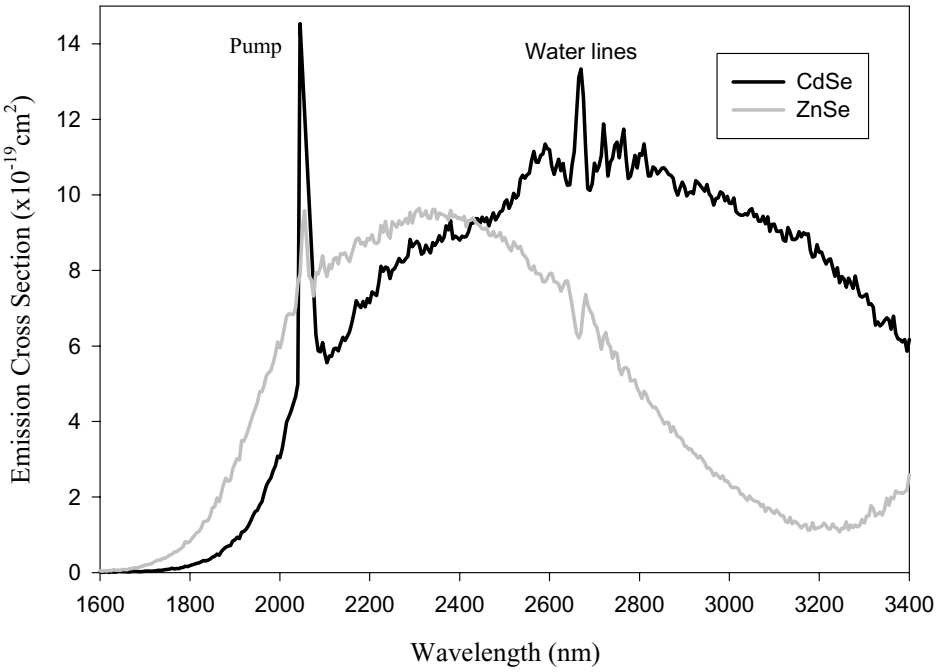

Figure 3-6. Calculated Stimulated Emission Cross Section Measurements in Cr^{2+}:CdSe and Cr^{2+}:ZnSe Using Calibrated Fluorescence Measurements

3.4 Estimated Thermal Load

Given the strong thermal lensing and temperature dependent non-radiative relaxation rates seen in Cr^{2+}:II-VI materials, it is useful to have an estimate of both lasing and non-

lasing thermal loading incurred by the absorption of the pump laser beam. An estimate can be obtained by using the fluorescence lifetime and emission line-shape to calculate the fraction of pump photon energy that turns into heat for a given temperature (and wavelength if lasing).

When pumped at 1.9 μm, quantum efficiency calculations using the measured line shape functions discussed in Section 3.3 produce a thermal load of 15 percent in Cr^{2+}:ZnSe and 20 percent in Cr^{2+}:CdSe. These values represent the minimum thermal load produced by 1.9-μm pumping under non-lasing conditions, since the non-radiative transition path between the excited and ground states is not considered. Factoring in the non-radiative transition rate of course significantly increases the estimated heat load. Using the lifetime measurements described in Section 3.2 to estimate non-radiative relaxation rates, estimates of non-lasing thermal loading at 300K are 30% for the Cr^{2+}:ZnSe sample and 60% for the Cr^{2+}:CdSe and Cr^{2+}:CdMnTe samples. The estimated non-lasing thermal loading at 350K is 60% for the Cr^{2+}:ZnSe sample and virtually 100% for the Cr^{2+}:CdSe and Cr^{2+}:CdMnTe samples.

If the samples are lasing, however, the situation changes. Pulsed and CW laser operation result in thermal loading in the range of 30%-40%, though for different reasons. For CW laser operation, the excited state population is clamped at the threshold value, considerably reducing the excited state population that can non-radiatively decay. The thermal loading for CW operation consists of two parts: the thermal loading due to the power absorbed in reaching laser threshold and the thermal loading produced in the generation of laser output. The first part is just radiative efficiency, which has been

covered already and is on average about 50% for near room temperature operation. The second part is simply due to the quantum efficiency of the laser operation, which produces thermal loading anywhere from 10% to 40% depending on the pump and laser wavelengths. Thermal loading due to quantum efficiency of the laser is about 25% for 1.9-μm pumping and 2.5-μm lasing, a fairly representative situation for Cr^{2+} lasers. Thermal loading for CW laser operation is expected to be around 30-40%.

Thermal loading for pulsed operation is determined mainly by the cavity build-up time and the quantum efficiency of the laser. For pulsed operation, non-radiative relaxation affects things differently, mainly decreasing energy storage lifetime. The Cr^{2+} lifetime is already short enough that CW-pumped Q-switched operation is impractical, so gain-switched pumping is used. In gain-switched pumping, the longer the delay between the pump pulse and the Cr^{2+} output pulse is, the less efficient the laser is due to decay of the excited state population. The fraction of excited state population that decays produces thermal loading as if the sample were not lasing. The fraction of the pump laser power that is converted into laser output produces thermal loading based on the quantum efficiency of the laser. The amount of thermal loading is determined by the ratio between the start-up time of the laser resonator and the excited state lifetime. Thermal loading for pulsed Cr^{2+} operation is somewhere between the values for non-lasing thermal loading and those for thermal loading based on laser quantum efficiency. Thermal loading in pulsed lasing Cr^{2+}:II-VI materials is approximately 25-30%, given 1.9-μm pumping and 2.5-μm lasing, assuming the pumping is several times threshold and the cavity start-up time is several times shorter than the excited state lifetime.

Since the thermal load while lasing should stay less than 40%, but the non-lasing thermal load at temperatures of 350 K or greater is 60-100%, it is safe to say that the non-lasing thermal loading for intensely pumped Cr^{2+}:II-VI materials will be as much as double that of the thermal loading while lasing, assuming the cooling system is operating at room temperature.

3.5 Bandwidth Measurement of Cr^{2+}:CdSe Optical Gain

The wide emission bandwidth of Cr^{2+}:II-VI materials makes them attractive source materials for applications requiring tunable lasers. Some of the potential applications involve the detection of organic molecules (like methane) that have absorption features in the 2.7-3.5 μm range. The Cr^{2+} laser could be a useful source for those applications if it could be made to tune out over that range. The stimulated emission cross section measurements of Section 3.3 indicated that it should be possible for Cr^{2+}:CdSe (but not Cr^{2+}:ZnSe) to generate laser output over the required range, although such a feat had never been demonstrated. Perhaps limited coating bandwidth and thermal effects had prevented earlier experiments[24] from realizing the entire Cr^{2+}:CdSe tuning range. An experiment was conducted to measure the bandwidth of optical gain in pumped Cr^{2+}:CdSe using a tunable laser cavity, to verify that there really was laser gain in Cr^{2+}:CdSe for wavelengths longer than 3 μm.

The laser tuning experimental setup consisted of a simple end-pumped Cr^{2+}:CdSe standing wave laser using a lightly doped 12-mm long Cr^{2+}:CdSe laser rod with 6 μs lifetime and 63% pump absorption, a Tm,Ho:YLF laser for excitation, a 295 g/mm diffraction grating for tuning, and a 15-cm spectrometer and pyroelectric detector for

wavelength measurements. A schematic of the setup is shown in Figure 3-7. The Tm,Ho:YLF laser was Q-switched at 3 kHz (400 ns FWHM pulses) and focused to a 1-mm beam diameter inside the Cr^{2+}:CdSe rod. The laser rod was held in a water-cooled heat sink, with the water temperature at 293 K. Positive thermal lensing inside the laser rod provided the cavity stability. The output from the Cr^{2+}:CdSe laser was the ~20% specular reflection from the diffraction grating, and the feedback was provided by the first order diffraction. Changing the grating angle changed the Cr^{2+}:CdSe laser wavelength. The output was sent through a 15-cm monochromator and detected by a chopped pyro-electric power meter.

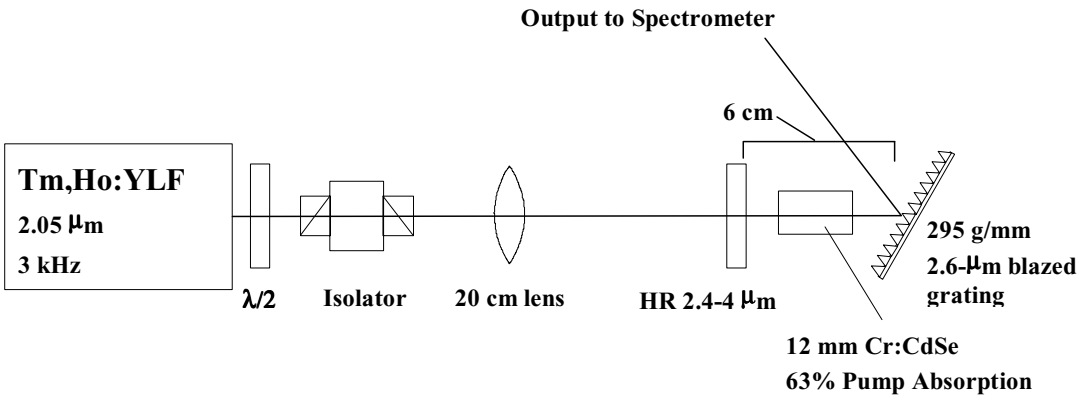

Figure 3-7. Cr^{2+}:CdSe Laser Tuning Experiment Configuration

An estimate of relative laser gain as a function of wavelength was obtained by recording the threshold of the Cr^{2+}:CdSe laser at a series of different grating angles (Cr^{2+} laser wavelengths) with respect to absorbed pulse energy. Measuring laser threshold provided the most direct measurement of laser gain, requiring the minimum assumptions to be made. In this case, the assumption is that, to first order, the cavity loss is constant over the tuning range (for lack of any better estimate of diffraction grating specular

reflectivity). Since gain = loss at laser threshold, and the cavity loss was fairly constant over the tuning range, the threshold measurements represent a measure of relative optical gain as a function of wavelength. The higher the laser threshold for a particular wavelength, the lower the gain per unit pump intensity was for that wavelength. The result is shown in Figure 3-8.

The experiment validates the stimulated emission cross section measurements that indicate significant gain out to long wavelengths past 3 μm. A broad tuning range of 2450 nm to 3400 nm was demonstrated, the longest wavelength tuning yet achieved for a Cr^{2+} laser. Tuning below 2450 nm has previously been demonstrated, but was not possible for this experiment, due to a cutoff in the input-coupler reflectivity at 2450 nm. With appropriate broadband optics (such as metallic mirrors), pulsed operation over the range of 2.3-3.4 μm from the Cr^{2+}:CdSe laser should be possible. The fundamental limits on the tuning range are ground state absorption at short wavelengths and the onset of thermal effects and damage at long wavelengths. It is possible that Cr^{2+}:CdSe laser sources could be used for detection of organic chemicals in the atmosphere, and other applications requiring a laser tunable from 2.3-3.4 μm. Obtaining efficient laser operation at the long wavelength end of the tuning curve would require considerable effort, however, due to the 40% or higher thermal load produced at those long wavelengths (capping optical-to-optical efficiency at 60% at best.). Pump absorption and mode matching had better be right on target.

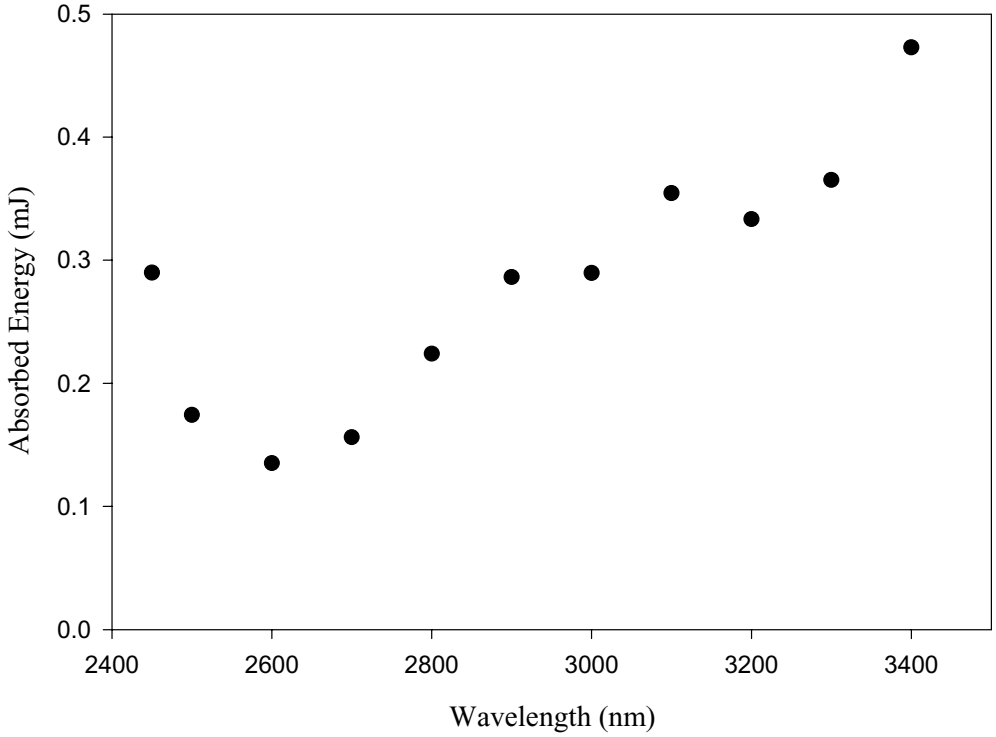

Figure 3-8. Cr^{2+}:CdSe Laser Threshold as a Function of Cr^{2+}:CdSe Laser Output Wavelength

3.6 Summary of Material Characterization

Pertinent Cr^{2+} laser design issues revealed by these experiments are summarized in the following list:

1. Cr^{2+} concentrations higher than about $20x10^{18}$ cm^{-3} in Cr^{2+}:ZnSe and $6x10^{18}$ cm^{-3} in Cr^{2+}:CdSe resulted in over 50% reduction of fluorescence lifetime in the samples measured. This would represent the maximum doping level for a useful laser crystal. The concentration might need to be lower for CW laser operation to keep threshold low. Pump absorption is limited to less than approx. 2.1 J/cm^3 in Cr^{2+}:ZnSe and 0.63 J/cm^3 in Cr^{2+}:CdSe. Bleaching of the absorption in good

Cr^{2+}:II-VI laser crystals is of prime concern in laser design, making Cr^{2+}:ZnSe the clear choice for thin disk material or for high energy pulsed operation.

2. The Cr^{2+}:II-VI materials exhibit reduction in fluorescence lifetime at temperatures at or above 300K. All three materials (Cr^{2+}:ZnSe, Cr^{2+}:CdSe, Cr^{2+}:CdMnTe) exhibited this phenomenon. The excited state lifetimes of all three materials fell to less than 50% of their maximum values at temperatures of 350K or more. Some of the samples exhibited significant lifetime reduction even at 300K. Any Cr^{2+} laser design must either plan for this to occur or incorporate cooling the outside of the laser rod substantially below room temperature to avoid an efficiency penalty. A little more investment in materials development might render this problem obsolete, however, as there is variability among different samples of essentially identical laser materials.
3. The thermal load in pumped Cr^{2+} laser materials is significant, as much as 30%-100% for the non-lasing case, depending on the material and its temperature. Fortunately, the thermal load while lasing should be more reasonable, around 30% for reasonable lasing conditions (1.9-μm pumping at 4 times threshold, 2.5-μm lasing). Note that laser threshold will increase with increased temperature, so thermal runaway needs to be avoided in the laser design by ensuring thresholds occur at low operating temperatures (or low input pump powers). Interestingly, keeping the laser threshold low also helps to prevent significant bleaching of the Cr^{2+} absorption from occurring in CW and some pulsed laser configurations. Running a gain-switched laser with both pump pulse-width and resonator start-up

time less than 0.5-1 μs allows one to ignore both temperature effects and bleaching effects.

4. Measurements of stimulated emission cross section show peak cross section values in the range of 10^{-18} cm^{-3} for both Cr^{2+}ZnSe and Cr^{2+}:CdSe, with maximum potential laser tuning ranges of ~2-3 μm for Cr^{2+}:ZnSe and ~2.2-3.4 μm for Cr^{2+}:CdSe.
5. The Cr^{2+}:II-VI materials really can work in broadband lasers tunable over the bulk of their emission range, as evidenced by the tuning of the Cr^{2+}:CdSe laser from 2450-3400 nm.

The results of these experiments represent a fairly complete picture of the potential issues that should be considered in designing a Cr^{2+} laser, but often are not. One notices that there are quite a few restrictions on the parameter space that might produce an otherwise effective Cr^{2+} laser design. Of these, the difficulty of incorporating more Cr^{2+} in the II-VI materials is the hardest to deal with, as it impacts laser design in so many ways, all of which impair efficiency. Getting that concentration increased by a factor of 5-10 without increased non-radiative relaxation rates would open up the parameter space of Cr^{2+} laser design considerably.

4 Final Cr^{2+} Laser Design

This section discusses the issues involved with determining the optimum laser design and presents the resulting final design for the Cr^{2+} laser power scaling experiment. First, design decisions influenced by the 20-W limit on pump power are discussed. Next, the basic laser design and predicted performance is presented. A discussion of what optical cavity is needed to ensure stability and good mode overlap follows. Finally, the overall laser design is summarized.

4.1 Design Decisions Forced by Limited Pump Power

The fact that no more than 20 W of pump power was available resulted in two big design decisions that, combined with the constraints imposed by Cr^{2+}:II-VI properties, virtually removed all degrees of freedom in the laser design. The first design decision forced by limited pump power was the choice of the disk laser design over the slab laser design. Background research indicated that the disk and slab laser designs were suitable for power scaling the Cr^{2+}:II-VI laser, but only the disk laser would work efficiently with less than 20-W pump power. The second design decision forced by limited pump power was the choice of gain region diameter in the laser disk. For the 20-W maximum pump power available, the beam diameter had to be less than 1 mm to get the laser pumped several times above threshold for efficient operation, given the 400-1000 W/cm^2 pumping needed to reach Cr^{2+} laser threshold.

The fact that a 1-mm or smaller beam diameter was to be used in the disk laser forced the disk to be only 0.25-mm thick to maintain the 4:1 beam diameter to disk thickness ratio needed for thermal lens mitigation. The Cr^{2+} doping density in the disk had to be as

high as possible, to ensure adequate absorption of the pump laser power. ZnSe thus had to be the host material for the laser disk, as it could incorporate the most Cr^{2+}. Even then, Cr^{2+} doping densities of at least 10^{19} cm^{-3} were needed, the upper doping limit for acceptable Cr^{2+}:ZnSe excited state lifetime. Even at this (relatively) high Cr^{2+} doping level, the pump laser wavelength needed to be as close as possible to the Cr^{2+}:ZnSe absorption peak at 1.75 μm, and at least 8-pass pumping would still be needed to ensure adequate (80%) pump absorption due to the disk thickness. In addition, the loss in the resonator had to be low, to allow efficient laser operation with low enough laser threshold to prevent Cr^{2+} absorption from bleaching out before threshold was reached. In short, a maximally-doped 0.25-mm thick disk combined with a complicated multi-pass pumping system would result in the best performance for Cr^{2+} power scaling using the disk laser design and < 20-W input power.

4.2 Estimated Laser Efficiency and Maximum Output Power

Given a 0.25-mm Cr^{2+}:ZnSe disk and multiple-pass pumping, the efficiency of the disk laser would be good if the loss in the disk were low enough. Since the disk is so thin, the loss would be mainly due to surface polish and coating losses. Given IR coating technology for ZnSe, coating losses on the order of 2% or less could be expected. Assuming loss of 2% in the laser disk, output mirrors already available in the lab with reflectivity of 97%R or 90%R (at 2.5 μm) could be used to complete the optical cavity, producing predicted output power levels of 6-6.5 W at slope efficiencies in the range of 45-65% and thresholds of 380-950 W/cm^2. The design predicted more output power than the 5-W goal, hopefully enough to provide a comfortable safety margin.

4.3 Cavity Design for Stability and Mode Overlap

The above calculations assumed that a stable resonator with good mode overlap at the gain region would be used. To achieve the efficiencies predicted in the laser dynamics model, the resonant cavity had to be stable and support a mode radius somewhere between approximately 50% and 100% of the radius of the pumped spot, multi-mode operation being acceptable for this demonstration. A stable cavity with mode radius between 0.25 mm and 0.5 mm was needed.

The resonant cavity was a simple two-mirror standing wave cavity shown in Figure 4-1 consisting of the highly reflective (coated) rear surface of the Cr^{2+}:ZnSe laser disk acting as one mirror and a concave partially reflective output coupler as the other mirror. This simple cavity was easy to align and did not suffer the loss that would have been incurred by including additional optics in the laser cavity. Pumping the laser disk was done through the disk input face, using off axis beams to allow multiple-pass pumping to be done without having extra optics in the resonator. For stability and mode overlap considerations, the only effect of pumping is to vary the strength of the thermal lens present in the gain material.

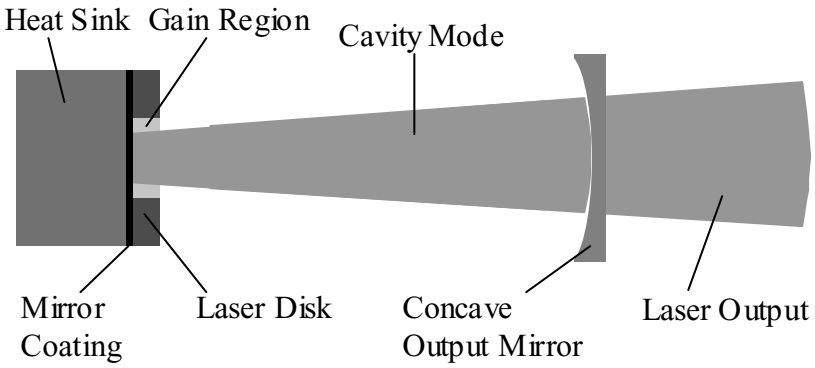

Figure 4-1. Schematic of Disk Laser Cavity

The stability of this simple laser cavity was determined by three things: the distance d between the disk and the output mirror, the radius of curvature R of the output mirror, and the focal length f_{th} of the thermal lens present in the laser disk gain region. The thermal lens in the laser disk was modeled as an unaberrated thin lens for simplicity and indeed for lack of knowledge of the nature and severity of actual aberrations. The disk was thin enough that, with a thermal lens present, it acted like a concave mirror with radius of curvature equal to the one-pass focal length of the thermal lens. The expression for cavity stability was thus essentially the familiar expression for the stability of a two-mirror cavity, using the convention of concave mirrors having positive radius of curvature and converging lenses having positive focal length:

$$0 \le \left(1 - \frac{d}{R}\right)\left(1 - \frac{d}{f_{th}}\right) \le 1 \qquad (4\text{-}1)$$

In addition to stability, mode overlap considerations imposed a constraint on cavity design. Mode radius at the laser disk needed to be in the range of 0.25 mm to 0.5 mm for

the likelihood of efficient laser operation to be good. The expression for the mode radius W at the laser disk is:

$$W = \left| \left[\frac{4\lambda d\left(1-\frac{d}{R}\right)}{\pi\sqrt{4-\left(2-\frac{4d}{R}-\frac{4d}{f_{th}}+\frac{4d^2}{f_{th}R}\right)^2}} \right]^{\frac{1}{2}} \right| \tag{4-2}$$

Note that the thermal-lens focal length of the laser disk appears in the expressions for cavity stability and mode radius at the laser disk. The amount of thermal lensing had to be estimated in order to calculate cavity stability and cavity mode size. The disk laser geometry was supposed to render thermal lensing negligible if the disks were at least 4 times thinner than the beam diameter, and the transverse absorbed power distribution were uniform. However, if experimental conditions deviated from the ideal design specifications, such as having to use thicker disks or pumping with non-uniform transverse intensity distribution, strong thermal lensing might be present. The simple equation of (4-3) for thermal lensing in a uniformly pumped laser rod was used to estimate the thermal-lens focal length for the case of strong thermal lensing.

$$f \approx \frac{\kappa A}{P_a}\left(\frac{1}{2}\frac{dn}{dT}\right)^{-1} \tag{4-3}$$

The result was a 40-cm focal length thermal lens for a 1-W heat load absorbed in a 1-mm diameter spot in Cr^{2+}:ZnSe. The actual heat load produced in Cr^{2+}:ZnSe material as a fraction of pump power absorbed was estimated at 25-30% while lasing, due to the ratio of pump wavelength (1.9 μm) to output wavelength (2.5 μm). At the estimated maximum absorbed power level (80% of 20 W), the total heat load in the laser disk was estimated at

5 W, yielding an estimated thermal lens focal length of 8 cm if a thick disk had to be used. Note that this 8-cm focal length is for one pass through the disk. Since the disk is used as a cavity mirror, light passes through the thermal lens twice, making the laser disk act like a concave mirror with radius of curvature f_{th}.

The following plots show cavity stability and mode radius as a function of cavity length and output coupler radius of curvature to show the parameter space that the disk laser demonstration was likely to operate in. Figure 4-2 shows stability for negligible thermal lensing. Figure 4-3 shows the mode radius at the laser disk for the case of negligible thermal lensing for a selected set of output mirror curvatures: concave mirrors with radius of curvature values of 10 cm, 20 cm, 30 cm, 40 cm, and 50 cm. Figure 4-4 shows stability for the case of the predicted 8-cm focal length thermal lens at full pump power. Figure 4-5 shows the mode-radius at the laser disk for the case with 8-cm focal length thermal lens, using the same set of output coupler curvatures as in Figure 4-3.

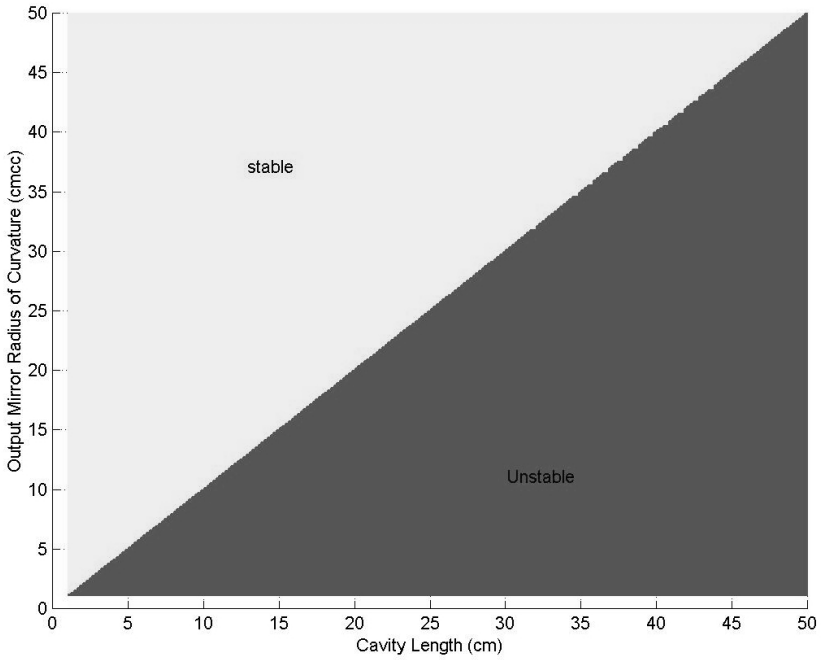

Figure 4-2. Stability Diagram for Disk Laser Design Parameter Space, Negligible Thermal Lensing

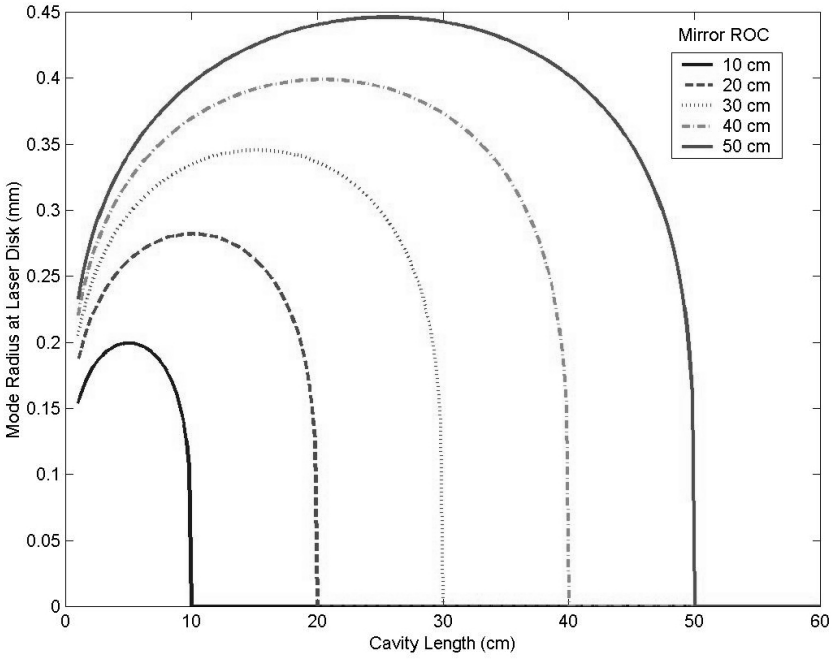

Figure 4-3. Cavity Mode Radius at the Laser Disk as a Function of Cavity Parameters, Negligible Thermal Lensing

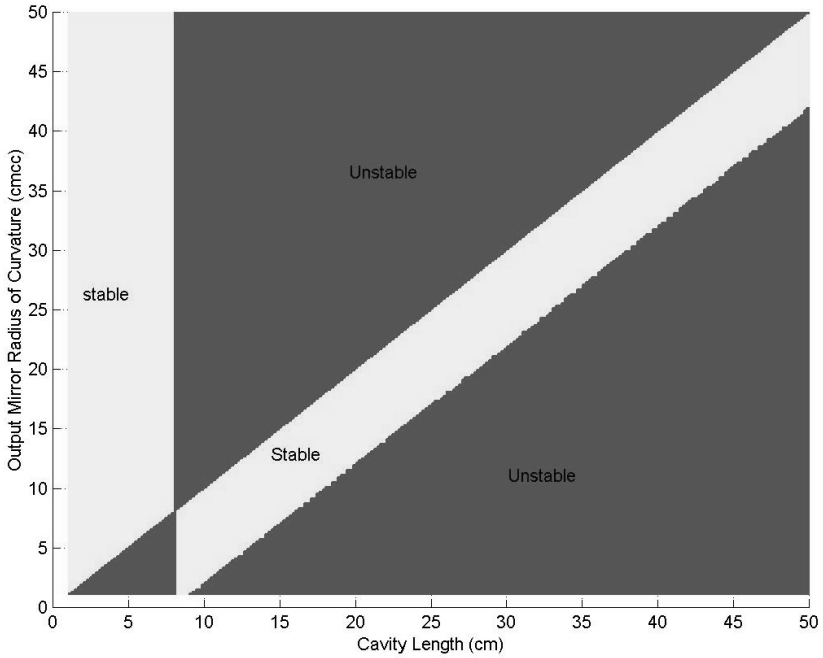

Figure 4-4. Stability Diagram for Disk Laser Design Parameter Space, Strong Thermal Lensing (f_{th} = 8 cm)

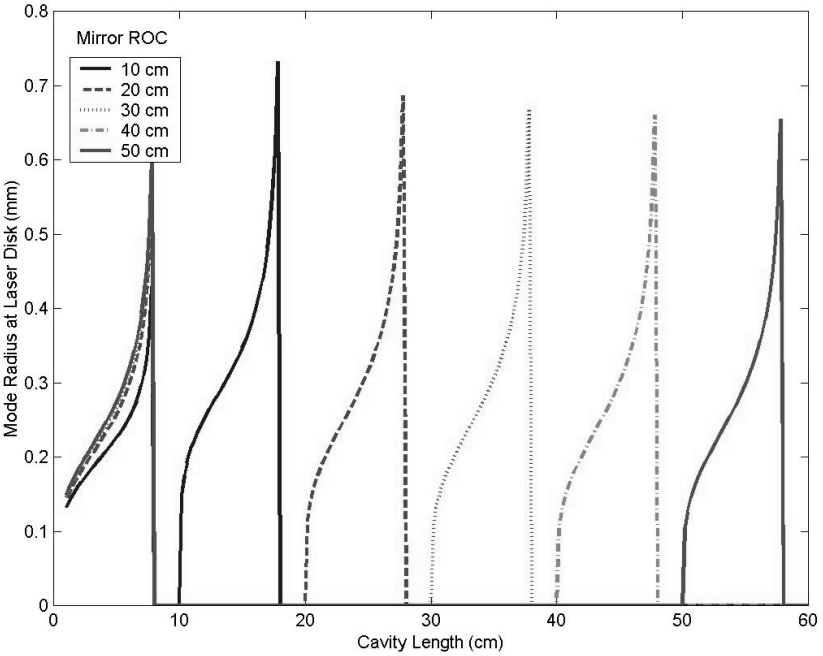

Figure 4-5. Cavity Mode Radius at the Laser Disk as a Function of Cavity Parameters, Strong Thermal Lensing (f_{th} = 8 cm)

Ideally, the thermal lensing would be negligible in the disk laser. In this case, the cavity is stable when cavity length is less than the output mirror radius of curvature. Mode radius increases with output coupler radius. Looking at Figure 4-3, acceptable mode radius can be obtained using mirrors with radius of curvature no shorter than 20 cm concave curvature (cmcc). The 20-cmcc mirror produces multi-mode operation, while the 50-cmcc mirror produces either single mode operation or multi-mode operation, depending on the cavity length. Cavity length of 50% of the mirror radius of curvature produces the maximum mode-radius. Mirrors with radius of curvature longer than 50 cm could be used in theory, but then the lab setup becomes more difficult to align and more vulnerable to disturbance. There is no need to use mirrors with radius any longer than that required to produce adequate mode overlap. Thus, the basic design for the disk laser if thermal lensing proved to be negligible was a 25-cm long cavity with a 50-cm radius of curvature mirror for single-mode operation, and a 10-cm long cavity with 20-cm radius of curvature mirror for multi-mode operation.

If the thermal lensing proved to be significant despite the disk laser configuration, a different cavity design would be needed. There are two modes of operation in the case of strong thermal lensing: a short cavity with cavity length in the range of $d < f_{th}$ (and $d < |R|$), and a long cavity with $|R| < d < f_{th} + |R|$. Both modes of operation produce similar distributions of cavity mode radius at the laser disk as a function of cavity parameters. In addition, the cavity mode size at the laser disk is almost identical for all five mirror curvatures used, given the 8-cm focal length thermal lens used in the model. A cavity mode radius of about 0.3 mm is readily obtained, within the range for efficient

multi-mode operation but definitely out of the range for efficient single-mode operation. At least this cavity does not need mirrors different than those used in the case of negligible thermal lensing: merely a cavity length change is needed.

4.4 Summary of Cr^{2+} Laser Design for Power Scaling Experiments

The final Cr^{2+} laser design was a 5-W Cr^{2+}:ZnSe laser operating at 2.5 μm, pumped by a 20-W (CW or high repetition-rate Q-switched) 1.9-μm Tm:YLF pump laser with a 1-mm diameter beam. A multiple-pass pumping system of at least 8 passes ensured at least 80% pump absorption in the Cr^{2+} laser disk. The Cr^{2+}:ZnSe disk would be low-loss, with 0.25-mm thickness and 10^{19} cm^{-3} Cr^{2+} concentration, coated anti-reflective (AR) on the input face, and highly-reflective (HR) on the rear face. The rear face of the disk would be mounted directly on a water-cooled heat sink to prevent overheating and subsequent loss of laser efficiency. The Cr^{2+} laser would use a simple standing wave cavity with cavity mirrors consisting of a partially reflective concave output mirror and the HR coating on the rear face of the laser disk. Concave output mirrors with reflectivity in the range of 90%-97% and radius of curvature in the range of 20-50 cm would be sufficient to ensure efficient laser operation. Under these conditions, the Cr^{2+} disk laser should produce 6-6.5 W maximum output power at slope efficiencies in the range of 45-65% and thresholds of 380-950 W/cm^2.

5 Pump Source Design and Performance

This chapter discusses the design and performance of the pump laser constructed for this research. At the start of this research, the available pump lasers in the lab at the appropriate wavelengths for pumping Cr^{2+} were diode-pumped, liquid-nitrogen cooled Tm,Ho:YLF lasers, producing up to 5 W each at 2.06 μm, operating CW or Q-switched with repetition rates of 1-20 kHz.. Although these lasers worked well in Cr^{2+} experiments, a pump laser was needed that could produce the 15-20 W required for the power scaling experiments and not be subject to interruptions every 30-minutes for refilling liquid nitrogen dewars. It became necessary to build a high power pump laser.

5.1 Pump Laser Design

The basic design was that of a cryogenically-cooled, end-pumped, bulk solid-state laser configured for CW or Q-switched multi-mode operation. Existing pump lasers in the lab used Tm,Ho:YLF which operates at 2.06 μm. The high power pump laser needed to operate near 1.9 μm to increase pump absorption efficiency in the thin Cr^{2+}:ZnSe disks. Since both Tm:YLF and Tm,Ho:YLF can be pumped at the same diode laser wavelength (Tm^{3+} absorbs the light in both cases), the high-power pump laser was designed to work with both Tm,Ho:YLF and Tm:YLF crystals. The evolution of the laser design resulted in two final configurations: one for Tm:YLF operation at 1.89 μm (Figure 5-1) and one for Tm,Ho:YLF at 2.06 μm (Figure 5-2).

Both configurations shared the same pumping scheme. Two 25-W fiber-coupled diode lasers supplied the pump power at 792 nm, which was 1:1 relay-imaged into the

laser crystal through each end, producing an 800-µm diameter pumped volume inside the laser crystal, which could be either 6%Tm,1%Ho:YLF for 2.06-µm operation or 5%Tm:YLF for 1.89-µm operation. The diode lasers were clamped to a water-cooled aluminum block and maintained at 289 K by a precision chiller to prevent the diode wavelengths from changing (which would change the 2-µm laser output power). The Tm,Ho:YLF crystal dimensions were 4x4x7 mm^3, with the long dimension being along the laser axis. The Tm:YLF crystals dimensions were 4x4x20 mm^3, with a 12-mm long doped region and two 4-mm long undoped end-caps (added to reduce risk of thermal fracture). A copper heat sink held either laser crystal and was maintained at ~150 K by a "Cryo-Tiger" closed-cycle cryogenic cooler with 30-W capacity. Due to the cryogenic cooling, the crystal had to be placed in an evacuated housing equipped with windows and dichroic beamsplitters to allow pump light to get in and resonated light to pass through. A vacuum roughing pump was used to periodically evacuate the housing to maintain vacuum insulation and prevent build-up of frost. (Most of the time the pump was simply left on).

The resonator design for both configurations was a simple multi-mode standing wave cavity. The multi-mode design was intentional, as it had been found that TEM_{00} operation resulted in not only less output power, but also a greater likelihood that the laser would be damaged during operation. For the Tm,Ho:YLF configuration, the resonator consisted of the HR coating on the rear face of the crystal, the crystal itself, a 20-cm focal-length intracavity lens placed 12 cm from the crystal to provide cavity stability, and a flat 70% reflecting output coupler placed 12 cm from the lens. The

Tm:YLF resonator consisted of a 38-cm long symmetric cavity with the crystal in the middle and mirrors with 20-cm radius of curvature placed at each end. Of course, the Tm:YLF crystal faces were both AR coated. Output coupler reflectivity for the Tm:YLF resonator was 70%, the same as for the Tm,Ho:YLF configuration. There were other optics in the resonators that did not significantly impact resonator stability, such as an acousto-optic modulator, the dichroic beamsplitters, and dewar windows. In addition, it was useful to put an uncoated piece of lithium niobate at Brewster's angle inside the laser cavity to ensure that output was completely polarized.

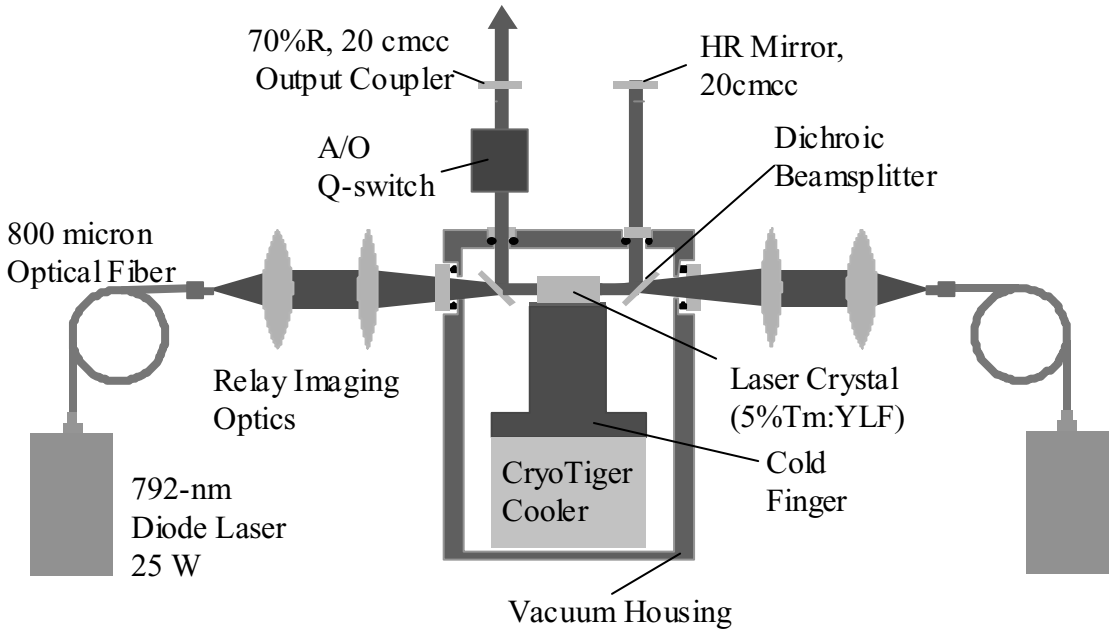

Figure 5-1. Schematic of Basic Pump Laser Design (Multi-Mode Tm:YLF Configuration)

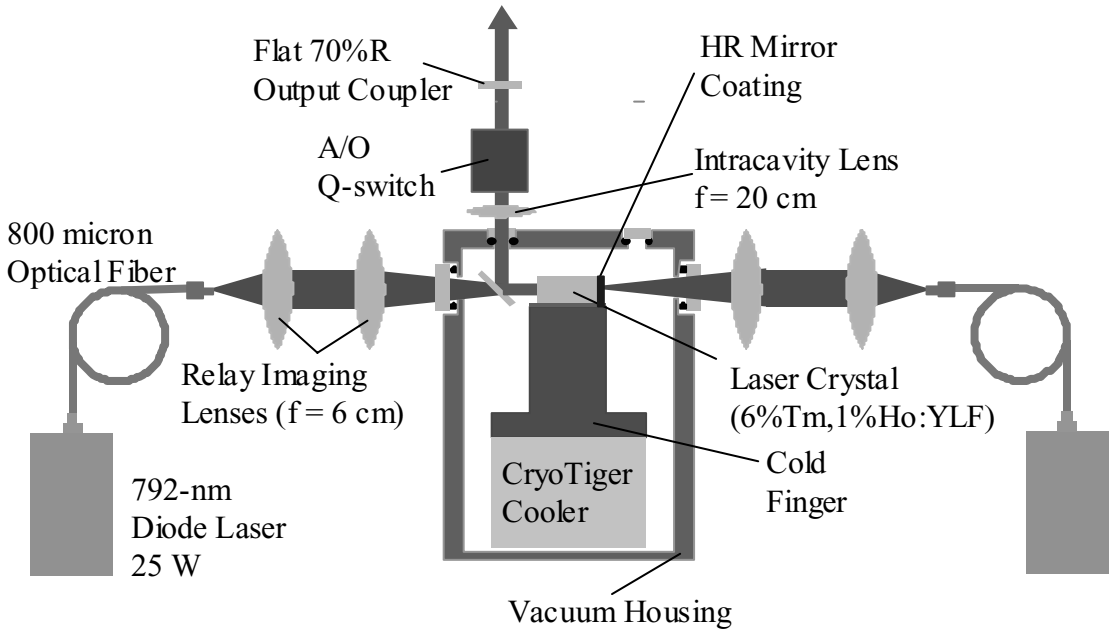

Figure 5-2. Schematic of Pump Laser Design, (Multi-Mode Tm,Ho:YLF Configuration)

5.2 Pump Laser Performance

Although the cavities used were different, both the Tm:YLF and Tm,Ho:YLF laser configurations in the end produced more than 15 W at 50-W diode laser input power for the two intended modes of operation: Q-switched at 10 kHz repetition rate, and continuous-wave. This corresponds to an optical-to-optical conversion efficiency of 30%. Beam parameters and output power did not differ significantly between the Q-switched and CW modes of operation. The Tm:YLF configuration produced 1.89-µm output with ~5 M^2 at full power. The Tm,Ho:YLF configuration produced 2.06-µm output with ~3 M^2 at full power. In Q-switched mode, pulse-widths in the range of 0.3-1 µs were produced, depending on the diode input power and hence pulse energy. The beam parameters changed at different diode laser input power levels, so the pump laser was simply designed to run at maximum output power at all times, with attenuation taken care

of outside the resonator. The laser could run at the same power level for extended periods, making it convenient to use in the Cr^{2+} experiments. It worked as designed, except that the output power of 15 W was less than the 20 W predicted. More power could be wrung from either pump-laser configuration, but only under conditions that tended to cause damage to the pump laser optical components.

For both CW and Q-switched operation the average output power stayed stable to within 10% over the course of a full research day, though over the course of weeks the maximum laser power tended to diminish. When power dropped below acceptable levels, the laser had to be 'overhauled,' which consisted of cleaning the crystal and translating the pump beams to a new, undamaged spot to regain full efficiency . This process could be performed as many as 6 to 7 times for a single laser crystal, providing on average 6 months to a year of satisfactory laser operation per crystal as long as catastrophic damage was avoided. The root cause for the damage remains unknown, but 'rogue pulses' and dust deposited by condensation are likely candidates. Obviously, this pump laser did require regular maintenance, which added up to a lot of time over the course of this research. Fortunately, the evacuated housing was designed to be easy to open and service. The only difficulty was there was no way to quickly warm up the cold finger if a crystal needed to be cleaned or replaced after it was cooled down. It took ~5 hours for the system to warm up, but only ~30 minutes to cool down. If a crystal was damaged while running the laser, every effort was made to translate the diode pumped spot to a clean crystal location and thus spare 5 hours of lost warm-up time.

Although average output power was stable on the hour time scale for CW operation, it was not stable at the microsecond time scale, showing sinusoidal oscillations with modulation depth anywhere from 20%-100%. This was a consequence of using the recirculating cooling system to keep the crystals cold, as it produced strong vibrations that could not be damped out. Turning off the cryogenic cooler drastically improved the amplitude stability at microsecond time scales, but obviously the cooler could not be left off long enough to perform experiments. Other ways to reduce the high frequency oscillations were through cavity alignment or by placing an etalon in the laser cavity and aligning it while watching the high-frequency output intensity variation on an oscilloscope. For the most part, however, the high frequency oscillations on the CW output were just ignored as they did not affect the Cr^{2+} laser operation.

Q-switched operation did not show similar vibration-induced instability, but had its own set of constraints. First, the pulse-width of laser output was determined by the pulse energy and the laser cavity (as might be expected). 1-mJ pulses had widths of ~300-500 ns and 100-μJ pulses had widths of ~1 μs. The actual pulse-widths seen for a given experiment were found to vary considerably as a function of fine alignment of the laser cavity mirrors. Second, the higher the repetition-rate, the more timing-jitter and variation in pulse energy there was in the pulse train. For 10 kHz operation at full power, timing jitter was within1 μs, and pulse energy variation was roughly 30%, although 'rogue pulses' with energy more than 2 times the average were observed to occur infrequently. If, for some reason, a particular pulse did not start or was of lower than average energy, the stored energy remaining in the laser material would 'keep' until the next opening of

the Q-switch, due to the ~2 ms lifetime of Tm:YLF. In fact, at 10-kHz repetition rate, energy could be stored efficiently over as many as 20 pulses, leading to pulse energy fluctuations. Third, for both configurations, the laser crystal and beamsplitter surfaces were found to have an optical surface damage threshold corresponding to 2 mJ of output energy per pulse with the 70%R mirror. This damage threshold had to be kept in mind when choosing the repetition rate of the Q-switch. The long excited state lifetimes of Tm:YLF and Tm,Ho:YLF allowed storage of more than 30 mJ of energy inside either kind of laser crystal at the highest diode pump powers, 15 times the laser damage threshold. Thus, setting the 15-W Tm:YLF laser to run Q-switched at 500-Hz repetition rate would result in a pump laser catastrophe. This damage restriction resulted in two main pulsed operation modes: 10-kHz repetition-rate at full power for Cr^{2+} laser power scaling tests, and 500-Hz operation at less than 500-mW output power for spectroscopy which required short, identical pulses with high energy, low timing jitter, and small thermal load. Finally, due to the likelihood of damage, it was always advisable to run the pump beam through a Faraday isolator to prevent accidental feedback from causing havoc.

5.3 Summary

With considerable effort and financial outlay, a high power 2-μm pump laser was constructed for the Cr^{2+} power scaling research. This laser produced 15 W of average output power with M^2 of 5 or less, at either 1.89 μm or 2.06 μm, in CW operation or as a train of Q-switched pulses with ~500-ns pulse width and 10-kHz repetition rate. Stability was good on the scale of hours (where it needed to be good), but suffered on time scales

of weeks due to the accumulation of incremental crystal-surface damage, and time scales of microseconds due to vibration-induced relaxation oscillations. Since the beam divergence changed as a function of diode laser input power, it proved easiest to run the laser at maximum power at all times and attenuate the output beam outside the resonator. The laser was not foolproof, and learning what part of its performance envelope to avoid was a time-consuming and expensive task. The damage threshold of optical surfaces inside the laser limited output pulse energy to 2 mJ, restricting Q-switched operation at full power to repetition rates of 10 kHz or higher. In the end, however, it got the job done, providing enough power for the Cr^{2+} power scaling experiments and enough control for the Cr^{2+}:II-VI spectroscopic characterization efforts. It certainly was an immense improvement over the 5-W liquid-nitrogen-cooled lasers present in the lab at the start of this research effort.

6 Cr^{2+}:ZnSe Disk Laser Experiments

This chapter is concerned with describing and evaluating the performance of the Cr^{2+}:ZnSe disk laser. First, the overall disk laser concept and intended resonator design are briefly described, putting the rest of the chapter in proper context by showing the design goals and expected performance of the Cr^{2+}:ZnSe disk laser. The Cr^{2+}:ZnSe disks are then discussed, summarizing manufacture, characterization, and heat-sink mounting techniques. Next, the three main disk laser experiments are presented: two power-handling experiments using 8-pass and 16-pass pumping systems, and an experiment investigating mode-coupling efficiency. Afterwards, the results of the Cr^{2+}:ZnSe disk laser experiments are summarized and evaluated with respect to the design goals.

6.1 Disk Laser Design

As mentioned earlier in Section 2.3.3, the disk laser is essentially an end-pumped rod laser in which the laser rod has a large diameter to thickness ratio. Figure 6-1 shows the basic design schematic. One disk face is coated AR; the other face is coated HR and mounted on a heat sink for face cooling. The disk acts both as the gain element and as an HR mirror of the optical cavity. Pumping is done through the AR face, at an angle to avoid the use of extra dichroic mirrors in the resonator. The face-cooling aspect of the disk laser architecture minimizes radial thermal gradients in the disk and thus reduces thermal lensing to manageable levels.

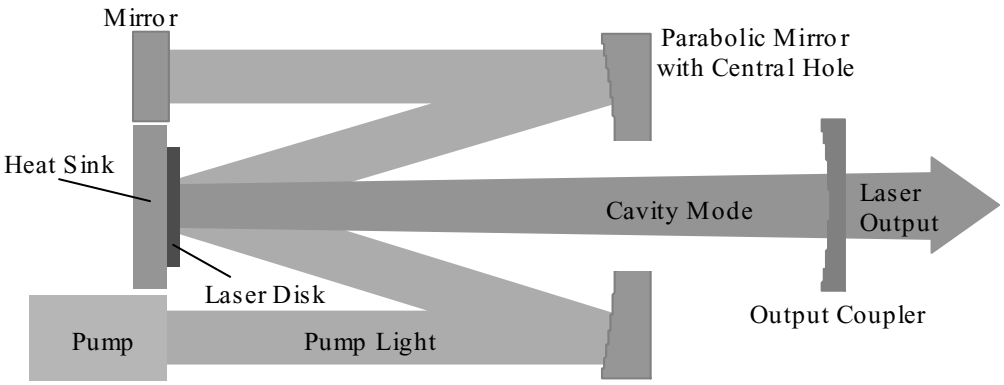

Figure 6-1. Schematic of Disk Laser Concept

The Cr^{2+}:ZnSe disk laser design described in Chapter 1 was for a simple, two mirror standing wave laser using a 0.25-mm Cr^{2+}:ZnSe disk with 10^{19} cm^{-3} Cr^{2+} doping, a 97%R output mirror with concave radius of curvature anywhere from 20-50 cm, and a 1-mm beam diameter. On paper, this design produced 6-W output power at 20-W input pump power. Once all the parts were purchased and the experiment set up, it soon became clear that this design was overly optimistic. The maximum pumping achievable at the disks turned out to be ~12 W, due to a maximum pump-laser power of ~15 W and ~30% optics losses due to polarizers with unexpectedly poor transmission.

The main difficulty with the thin disk laser design was thus ensuring the pump laser was absorbed efficiently. To maximize chances of success, disks of different thickness (1 mm, 0.5 mm, 0.25 mm) were purchased, and two multiple-pass pumping systems (8 pass and 16 pass) were designed.

6.2 Laser Disks

The laser disks used in this experiment were made of ZnSe with chromium diffused in by extended annealing at high temperatures. Two doping runs (using different conditions) were commissioned from Spectragen, resulting in Cr^{2+}:ZnSe samples with

different doping concentrations. The Cr^{2+}:ZnSe from each doping run was processed into three 10x10 mm^2 wide disks of different thickness: 1 mm, 0.5 mm, and 0.25 mm. Thus, there were six disks, with three disk sizes and two Cr^{2+} doping levels. The doping levels were designated as 'standard' and '2x' (double) Cr^{2+} doping. The 2x doping took 7 days at 1000 C. The standard doping took 5 days at slightly lower temperature. These doping runs attempted to produce the highest Cr^{2+} concentration possible in the ZnSe while still maintaining reasonable optical quality and Cr^{2+} emission lifetime. Transmission and bleaching measurements indicate that the maximum Cr^{2+} doping in the disks (produced by the '2x standard' doping) was around 2-5x10^{19} cm^{-3}. This high doping level was present only in the 2x-doped 1-mm thick disk. The other disks (such as the 2x-doped 0.5-mm disk) contained at least a factor of two less.

It is hard to tell just how much this difference in Cr^{2+} concentration depended on the doping parameters, given the post-processing steps required. Apparently, the high temperature annealing tends to cause enough vapor transport leave the surfaces of the samples quite rough. To obtain enough clear aperture, larger samples are doped, then ground down to the required sizes. This has the unfortunate side effect of grinding away most of the highly doped areas in each piece of Cr^{2+}:ZnSe. Samples apparently start out much the same size, so fabricating a thinner disk means simply grinding the doped sample down more, which amounts to removing more of the highly doped outer layers of the sample. Thus, the thinnest disks also had the lowest Cr^{2+} doping concentrations – a bad trend because the thinnest disks need high Cr^{2+} doping the most to ensure efficient absorption of the pump laser. Another consequence of this processing technique was that

a radial concentration gradient was present on all the disks, with as much as a factor of three higher Cr^{2+} concentration around the edge of the each disk than in the middle.

The unexpectedly low Cr^{2+} doping of the thinner disks rendered the 0.25-mm disks effectively unusable, and the 0.5-mm disks questionable. The disks ultimately used in laser experiments were the '2x'-doped 1-mm and 0.5-mm disks. The 1-mm disk had an absorption coefficient of 10.6 cm^{-1} (in the middle) and a Cr^{2+} fluorescence lifetime of ~4 μs. The 0.5-mm disk had an absorption coefficient of 6 cm^{-1} (in the middle), and a Cr^{2+} fluorescence lifetime of ~8 μs.

Once the disks arrived and were examined, they were sent out for optical coating. The disks were designed to act as 'active mirrors' in the disk laser resonator, with both the pump light and the resonated light entering and exiting the disk through one face only. Therefore, one face of each disk was coated antireflection at the pump and resonated wavelengths (1.89-2.06 μm and 2.5 μm respectively), and the other face was coated for maximum reflectivity at those wavelengths. The mirror-coated face was designed to be fastened or bonded to a heat sink, for management of the disk temperature during laser operation. To aid in the bonding, each disk had an extra metallic gold coating applied on top of the mirror coating. Although the 0.25-mm disk with 'standard' doping did not survive the coating process, the other five made it unscathed, in excellent condition.

The resulting laser crystals were of good optical quality. The surfaces were flat and smooth, the coatings were good, and the samples showed low internal loss. The 0.5-mm 2x-doped disk had roughly 2-3% overall round-trip loss for 2.5-μm light incident slightly

off axis. The 1-mm 2x-doped disk had slightly more loss, which varied depending on the exact position examined on the disk (but not more than 5-8%). This amount of loss is fairly typical for Cr^{2+} crystals coated for these wavelengths, and was not enough to cause problems in the laser experiments.

The two most promising Cr^{2+}:ZnSe disks, the 2x-doped 1-mm and 0.5-mm disks, were permanently mounted on individual heat sinks. The heat sinks were copper rods with one end faced off flat for mounting the disks, and the other end fitted with a compression pipe fitting for interfacing with a water circulation system. During laser operation, water circulated through a hole in the end of the heat sink tube with the pipe fitting to provide cooling.

The 1-mm disk was mounted first, using solder. The heat sink was tinned, cooled down, and then re-heated with the disk in place. A precarious situation ensued, with the disk floating on the tinned heat sink surface without sticking, but the use of rosin flux and light pressure and sideways movement applied by a pointed (soft, insulating) wooden stick caused the disk to finally stick. After the disk and heat sink cooled down, a final inspection indicated a successful mounting. Under strong visible lighting, one could see that the action of the flux and solder had mottled the gold coating on the back of the disk. Fortunately, the dielectric coating still held up under CW and Q-switched pumping.

Given that the solder technique (with flux) was a bit risky, the 0.5-mm disk was epoxied to its heat sink using conductive silver epoxy. This mounting technique was safe and easy, but ended up being somewhat unsatisfactory in the long haul. It seemed to allow the disk to flex or bubble a bit during intense CW excitation, and the distortion

would remain when the pump power was removed. After several experiments with 5-10W CW pumping in a 1-mm diameter beam, there were several 1-mm diameter permanent concavities in the rear surface mirror coating. No actual thermal fracturing of the entire disk was ever seen, just smooth lens-like concavities. In the end, the mounting techniques were good enough for laser experiments to be successful for both disks, but would need to be significantly improved to ever be considered reliable. Probably some technique of pressing the disk into a bed of indium on its heat sink and holding it in place while it is used would be the best. Developing such a technique was beyond the scope of this research.

In summary, the outcome of two doping runs, material processing, optical coating, crystal triage, and heat sink mounting were two diffusion-doped Cr^{2+}:ZnSe disks, mounted and ready for laser experiments: a 1-mm thick disk with 10.6 cm^{-1} absorption coefficient at the 1.89-μm pump laser wavelength and ~5% round-trip loss at the 2.5-μm Cr^{2+} laser wavelength, and a 0.5-mm thick disk with 6 cm^{-1} absorption coefficient at 1.89 μm and ~3% round-trip loss at 2.5 μm. The other disks purchased were never tested due to their unsatisfactory Cr^{2+} doping levels.

6.3 8-Pass Power Handling Experiment

An 8-pass pumping experiment was the first attempt at lasing the Cr^{2+}:ZnSe disks. The experiment used a 2.06-μm Tm,Ho:YLF laser as the pump source, and an 8-pass pumping system made from extra optics on hand. Use of this pump laser wavelength reduced the absorption coefficients in the disks by roughly a factor of three from their values at 1.89 μm, resulting in inefficient pumping of the 0.5-mm disk. Therefore, only

the 1-mm disk was used in this experiment. Despite the sub-optimal pumping, the experiment turned out quite well and indeed achieved record Cr^{2+} laser output power at the time, and the highest Cr^{2+} laser output power demonstrated in this entire set of laser experiments.

The Cr^{2+}:ZnSe disk laser, shown in Figure 6-2, consisted of a pump laser, the Cr^{2+}:ZnSe disk, an output coupler, and multi-pass pumping optics. The pump laser, which was a Q-switched Tm,Ho:YLF laser with 9-W average power at 2.06 μm, 10-kHz pulse repetition rate, was focused to a radius of 0.5 mm at the disk. The 1-mm thick Cr^{2+}:ZnSe disk was used in this experiment, because it readily absorbed the pump laser in just a few passes. The output coupler was a 90% reflecting, 10-cm concave radius of curvature mirror placed 8 cm from the surface of the disk. Although this cavity length and mirror curvature combination was not a part of the intended laser design, it was the only configuration found that performed well. The multi-pass pumping system consisted of a 10-cm focal length lens, a flat mirror, and a 30-cmcc curved mirror that were used to image the pump laser back onto the disk with unity magnification four times to yield eight one-way passes. Eight-pass pumping provided 95% pump light absorption. The pump beam was aligned off axis to eliminate the need for dichroic mirrors in the resonator and produced an elliptical [2 mm x 1 mm] gain region.

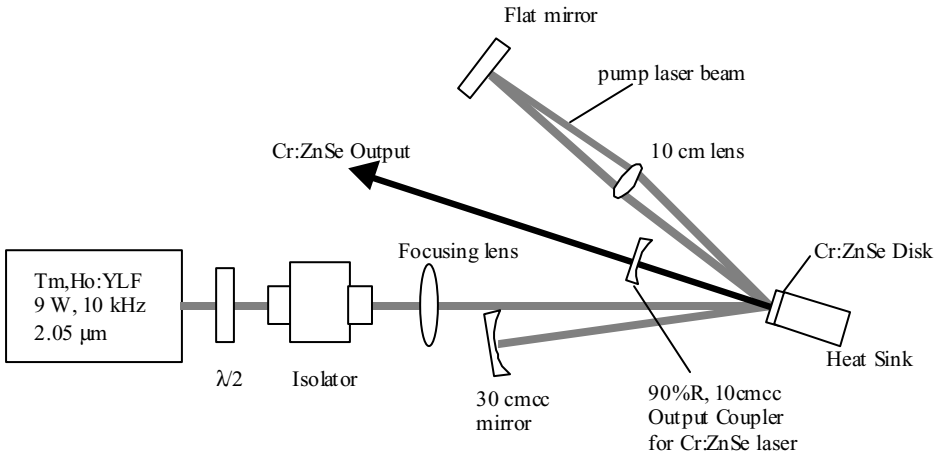

Figure 6-2. Configuration of Disk Laser with 8-pass Pumping System

The Cr^{2+}:ZnSe laser produced up to 4.27 W of output with 9-W input (see Figure 6-3). Threshold was 612 mW (61 μJ/pulse), and slope efficiency was 50% with respect to incident pump power. Overall optical efficiency at full power was 47%. This agrees with the model prediction of 690 mW threshold (8.8 mJ/cm^2) and 54% slope efficiency for a 1-mm diameter pump beam. This Cr^{2+} laser was stable and ran for over six hours with less than 2% variation in average output power. This configuration showed no sign of efficiency rolloff at higher pump power, the typical effect of thermal lensing. Other configurations having output mirrors with longer radii of curvature, or having longer cavity lengths showed considerably reduced output efficiency. A smaller pump beam diameter led to increased radial thermal gradients and instability of the laser cavity. Thus the ~1-mm diameter incident pump spot size represents the smallest useful pump spot size with respect to the 1-mm thick disk for this system, and the 8-cm long multi-mode resonator produced the highest coupling efficiency.

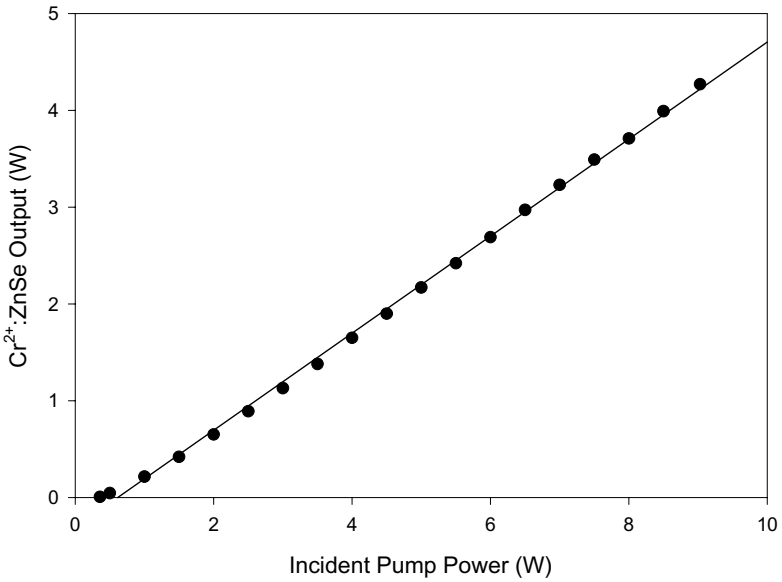

Figure 6-3. Cr^{2+}:ZnSe Disk Laser Input/Output Plot, 1-mm Disk, 8-Pass Pumping

The Cr^{2+} output beam was elliptical in shape with divergence that was 3 and 6 times diffraction limited along the minor and major beam axes, respectively. Output beam quality did not significantly change as a function of pump power. Laser bandwidth at full power was 56 nm FWHM, centered at 2500 nm – typical for a free-running pulsed Cr^{2+} laser with broadband mirrors. Output pulse width was 220 ns, consisting of a short gain-switched pulse followed by a longer pulse that lasted for the duration of the 290-ns FWHM pump pulse. Bandwidth and temporal profiles are shown in Figure 6-4 and Figure 6-5.

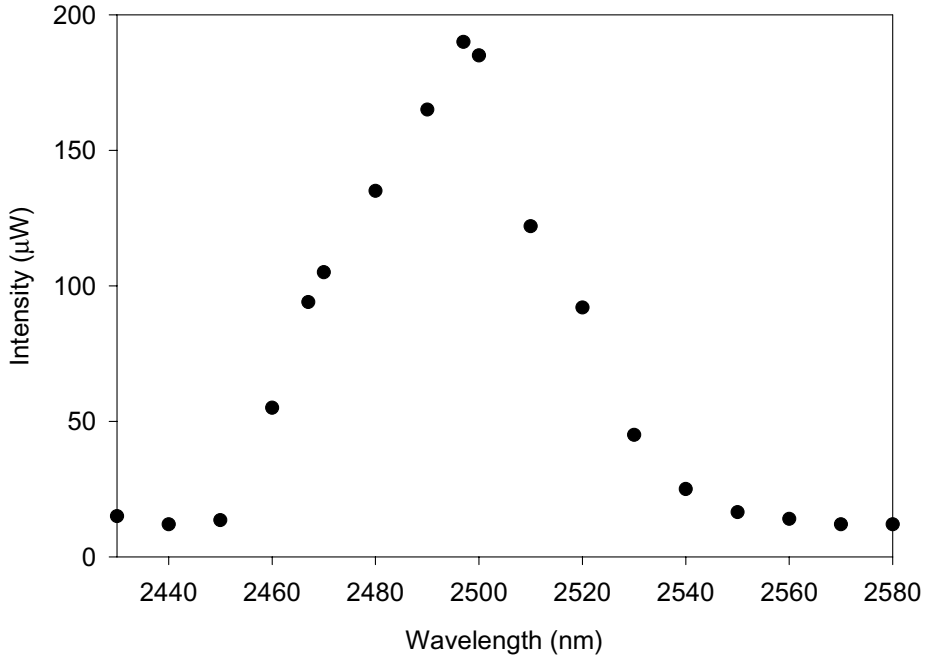

Figure 6-4. Cr^{2+}:ZnSe Laser Bandwidth at 4-W Output Power Using 90%R, 10-cmcc Output Coupler and 1-mm Disk, 8-Pass Pumping

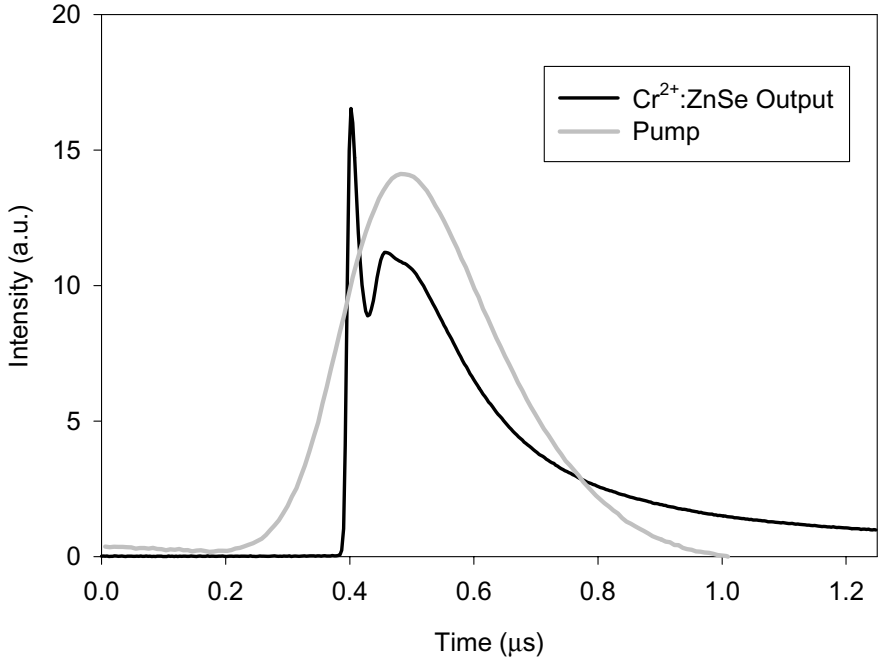

Figure 6-5. Temporal Profile of Pump and Cr^{2+}:ZnSe Laser Output Intensity, 4-W Output Power, 10 kHz Gain-Switched Operation

This resonator configuration did not allow for CW Cr^{2+} laser operation. Reaching Cr^{2+} laser threshold with CW pumping requires approximately 10-15 times more average power than with 10 kHz Q-switched pumping, on the order of 7-15 W for the 1-mm disk with 1-mm beam diameter and the 90%R output mirror. The thermal lensing present at these CW pump power levels prevented the Cr^{2+} laser from working, and in any case the pump laser could not supply more than 11 W on the crystal. CW operation required lower threshold resonators with less thermal lensing and hence required the use of the thinner, 0.5-mm disk and a more effective pumping scheme.

In summary, the 8-pass disk laser experiment showed that the disk laser concept could be used to make a Cr^{2+} laser with output power in the 5-W range, the goal of this research. The 1-mm Cr^{2+}:ZnSe disk laser performed well with Q-switched excitation in a 1-mm diameter beam, producing 4.3-W output power with slope efficiency of 50% and overall optical efficiency of 47%. The threshold and slope efficiency agreed fairly well with the model predictions assuming 1-mm diameter pump beam, short-pulse excitation, 5% passive loss, and no bleaching of the Cr^{2+} absorption. However, the output was highly multi-mode due the cavity design, and attempts to improve the beam quality by increasing the cavity mode size at the laser disk resulted in considerable reduction in laser efficiency not predicted by the simple qualitative mode-overlap analysis technique.

6.4 16-Pass Power Handling Experiment

A 16-pass pumping system was built, based on a design obtained from the literature[25], which could efficiently pump the 0.5-mm disk. A new set of experiments was then conducted to examine the power-handling performance of the mounted 1.0-mm

and 0.5-mm disks. Most of these experiments were done using the new 1.89-μm Tm:YLF pump laser, which allowed the 0.5-mm disk to be tested as well. This section presents the design and characterization of the 16-pass pumping system and discusses the power-handling experiment performed with it.

6.4.1 Description of 16-pass Pumping System

The 16-pass pumping system consisted of a 2-in. diameter, 2-in. focal length concave silver mirror, the Cr^{2+}:ZnSe disk, three roof prisms and a flat mirror. Figure 6-6 shows a side view schematic of the pumping system, and Figure 6-7 shows a schematic and a digital picture of a frontal view of the assembly with disk, prisms, and flat mirror. Note that the roof prisms, concave mirror, and flat mirror all were on tip-tilt stages with a common back-plane, enabling consistent alignment of the optics.

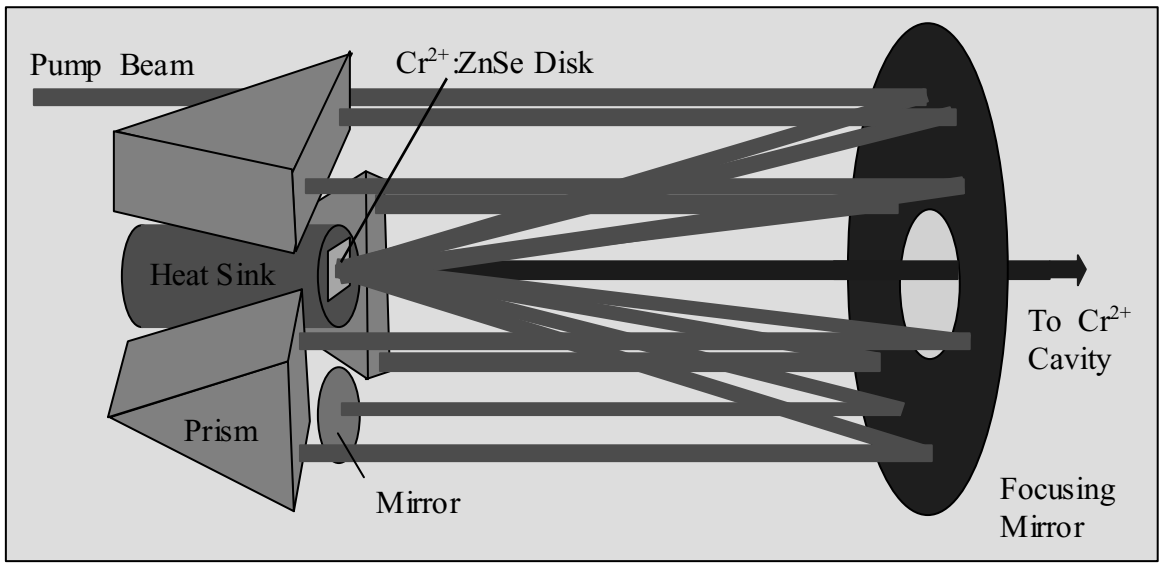

Figure 6-6. Side View Schematic of 16-Pass Pumping System

The 16-pass pumping system was set up so that the incoming pump light would be relay-imaged onto the crystal 8 times, for a total of 16 one-way passes. The schematic in

Figure 6-7 shows the sequence in which the pump beam encountered the prisms and flat mirror, with numbers indicating the sequence order and circles indicating the clear aperture at each location. Pump light entered the system through the hole at location 1 (above the Cr^{2+}:ZnSe disk), hit the concave mirror, and was focused onto the disk one focal length away. The pump light passed through the disk, reflected off the HR coating of the rear surface, passed through the disk again and traveled back to the concave mirror, resulting in the first two absorption passes. The mirror collimated the pump beam and sent it into a roof prism at location 2. The roof prism was oriented to produce a tangential displacement of the pump beam to location 3 before reflecting it back towards the concave mirror. After once again hitting the concave mirror, the pump beam was focused back onto the disk for the third and fourth absorption passes. The remaining pump beam went on to the concave mirror, was collimated again, and was sent into the second roof prism at location 4. The pump beam was translated tangentially to location 5, then reflected back to the concave mirror. Once again, the concave mirror focused the pump beam onto the disk to obtain the fifth and sixth pump passes. The remainder of the pump beam was reflected back onto the concave mirror, collimated, and sent to the third roof prism at location 6. After another tangential beam translation to location 7, the pump beam went back to the concave mirror and was sent onto the disk for the seventh and eighth pump passes. The remaining pump light went back to the concave mirror, was collimated, and was sent to the flat mirror at location 8. The flat mirror was oriented to send the pump beam back the way it came, completing 8 more passes through the laser disk for a total of 16.

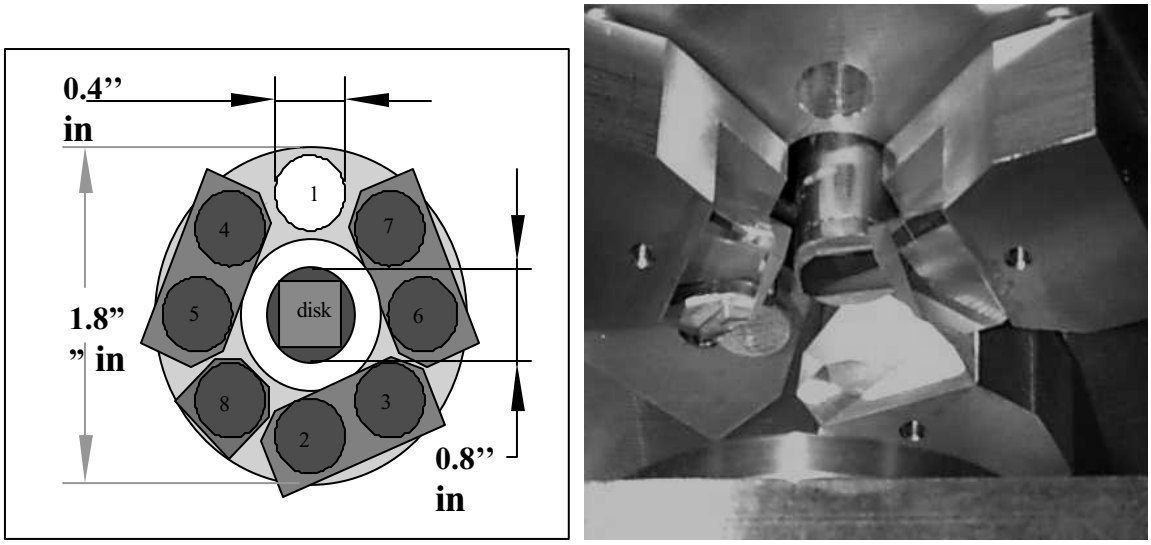

Figure 6-7. Front View Schematic and Picture of the Cr^{2+}:ZnSe Disk and Pump Translation Prisms in the 16-Pass Pumping System.
(These pictures are described in detail in the text)

The absorbed power density in the Cr^{2+}:ZnSe disk laser crystals produced by the 16-pass system was measured to evaluate the effectiveness of the pumping system and to enable accurate heat distributions to be used in the thermal modeling effort performed afterwards. The measurement technique employed was to image the fluorescence signal from the pumped, nonlasing Cr^{2+}:ZnSe disks onto an infrared camera and to assume that the detected fluorescence intensity profile corresponded to the absorbed pump power density. (This technique was not available at the time for the 8-pass experiment, as the hardware had not arrived yet). Naturally, this technique would render longitudinal variation in absorbed power not observable, but would fairly accurately record the overall transverse absorbed power distribution caused by the multi-pass pumping, since the disks were thinner than the depth of field of the imaging system. The lack of observability in the longitudinal direction was dealt with by assuming a uniform absorbed power density in that direction, which is not unreasonable given the multiple-pass pumping.

Fluorescence signal images of the pumped Cr^{2+}:ZnSe disks were recorded with an Electrophysics PV-320 IR camera for five cases (using 1.89-μm pumping), representing a good sample of the pumping conditions found for the laser experiments and in the later thermal characterization experiments. The fluorescence image bitmaps were loaded into Matlab, then each intensity map was normalized, converting it into a transverse fluorescence intensity distribution. These fluorescence distributions were compared with super-Gaussian functions to determine the best approximate representations of the transverse pumping distributions in that could be used in thermal modeling or mode-coupling analyses. The approximate curve fits are shown in Table 6-1. In addition, fluorescence images and intensity cross section plots are shown for case 1 (Figure 6-8, Figure 6-9) and Case 2 (Figure 6-10,Figure 6-11). For reference, the input pump beam had a transverse intensity distribution approximating a 4^{th} order Super-Gaussian with 0.4-mm radius for all cases.

Table 6-1. Estimated Transverse Absorbed Power Distributions in Pumped, Nonlasing Cr^{2+}:ZnSe Disks from Fluorescence Measurements

Case:	Disk Thickness:	Pumping:	Transverse Absorbed Power Distribution
1	1.0 mm	5 W CW	N=4 Super Gaussian, 0.41-mm Radius
2	0.5 mm	5 W CW	N=4 Super Gaussian, 0.45-mm Radius
3	1.0 mm	5 W Q-Sw.	N=4 Super Gaussian, 0.45-mm Radius
4	0.5 mm	5 W Q-Sw.	N=5 Super Gaussian, 0.6-mm Radius
5	1.0 mm	5 W Q-Sw. Fiber	N=4 Super Gaussian, 0.5-mm Radius

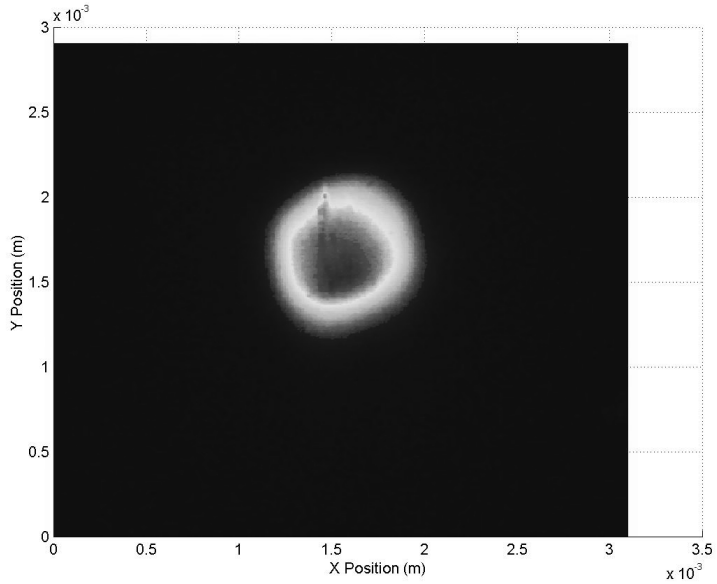

Figure 6-8. Fluorescence Image from 1-mm Disk with 5-W CW Pumping
This is an image of Cr^{2+} fluorescence detected by an IR camera, looking at the 1-mm Cr^{2+}:ZnSe laser disk on axis. The image represents transverse absorbed pump power distribution in the disk when the 16-pass pumping system is used.

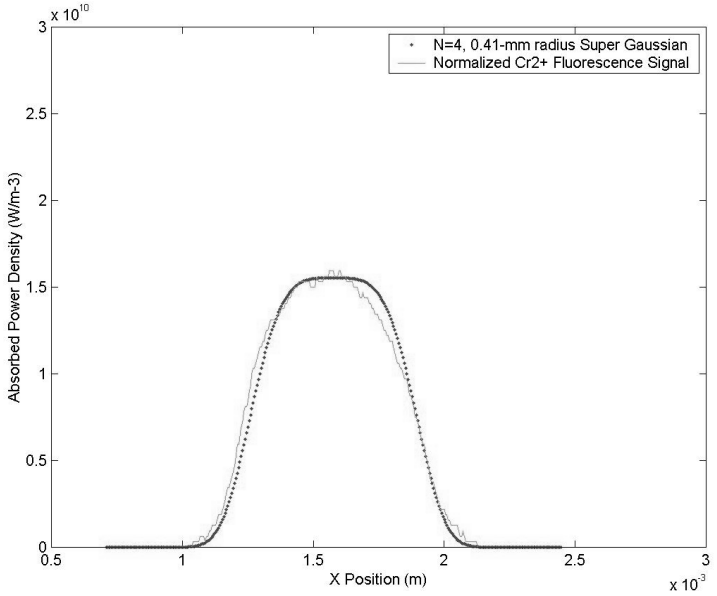

Figure 6-9. Absorbed Power Density in 1-mm Disk with 5-W CW pumping
This plot shows a cross section of the estimated absorbed power density in the laser disk, obtained by appropriately normalizing the fluorescence image of Figure 6-8. The dotted line corresponds to an approximate curve fit of a 2-D Super Gaussian of fourth order and 0.41-mm radius.

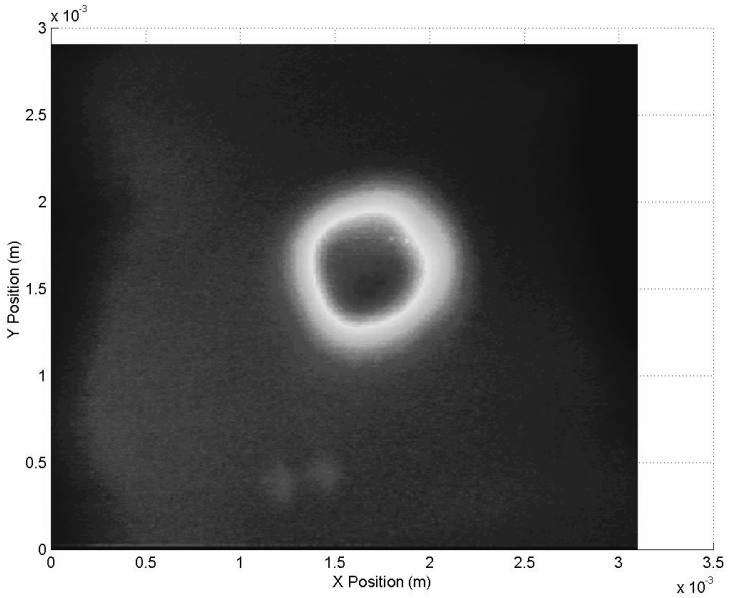

Figure 6-10. Fluorescence Image from 0.5-mm Disk with 5-W CW Pumping
This is an image of Cr^{2+} fluorescence, looking at the 0.5-mm Cr^{2+}:ZnSe laser disk on axis. The image represents transverse absorbed pump power distribution in the disk when the 16-pass pumping system is used.

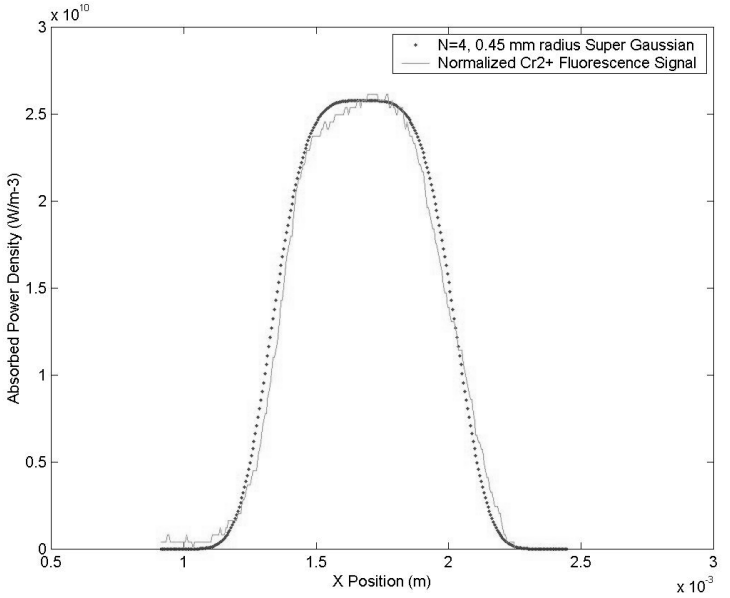

Figure 6-11. Absorbed Power Density in 0.5-mm Disk with 5-W CW pumping
This plot shows a cross section of the estimated absorbed power density in the laser disk, obtained by appropriately normalizing the fluorescence image of Figure 6-10. The dotted line corresponds to an approximate curve fit of a 2-D Super Gaussian of fourth order and 0.45-mm radius.

Translating the crystal in or out of the multiple-pass system changed the locations of where each pump pass hit the disk, allowing each pass to be seen separately at the same time by looking at the overall image of disk fluorescence. Using this technique, it was possible to see all eight spots (from the 16 one-way passes) on the 0.5-mm disk, all approximately the same size. Only the first four passes were visible for the 1-mm disk, due to its high absorption coefficient. In addition, further investigation using heat sensitive liquid crystal film to detect the size of the pump beam at each optic in the multiple-passing system indicated that the pump beam grew in size at the prisms only a moderate amount after each set of passes. Even the case which used fiber-launched pumping with M^2 of ~20 did not experience clipping of the pump beam in the 16-pass optical system. Thus, the increase in M^2 of the pump beam after successive passes through the disk and optical system did not degrade the effectiveness of the pumping system.

6.4.2 Laser Experiment

The first disk laser experiment simply repeated the 8-pass pumping experiment for both disks, using the new 16-pass pumping setup. The configuration of this experiment is shown in Figure 6-12. The pump laser beam was run through an isolator and variable attenuator into the disk laser gain module to pump the Cr^{2+}:ZnSe disk. The Cr^{2+} laser resonator consisted of the disk (with rear surface coated highly reflective) and a partially reflective output coupler with concave radius of curvature. The disk was placed one focal length away from the 50.8-cm focal length concave mirror; an intermediate lens was used to focus the pump beam to the correct size and divergence as it hit the concave

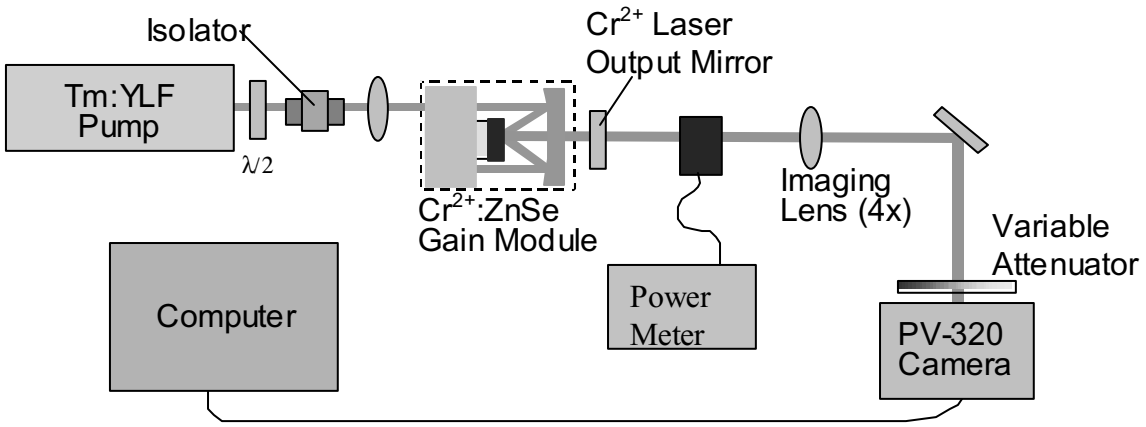

Figure 6-12. Configuration of Cr^{2+}:ZnSe Disk Laser for 16-Pass Pumping

mirror. It was advantageous for the pump beam to be multi-transverse mode to prevent unnecessarily small spot sizes at the concave mirror. A pump beam with $M^2 = 7$ was used, maintaining a beam radius close to ~0.5-mm throughout the 16-pass system (and 0.4-mm diameter at the disk). Pumping was done both Q-switched at 10 kHz and CW.

The Cr^{2+}:ZnSe laser output mirrors used in this experiment were: 97% R with 10-cm concave (cmcc) radius of curvature, 90% R with 10-cmcc radius of curvature, and 85% R with 20-cmcc radius of curvature. It was obvious from the 8-pass experiment that the highest efficiency came from a 10-cmcc output mirror placed at 8-10 cm from the Cr^{2+} disk. However, only 90% R and 97% R mirrors were available in this short radius. Thus, disappointing results were obtained with the 85% R mirror.

The results of the 16-pass disk laser experiment are shown in Table 6-2, showing input pump power at Cr^{2+} laser threshold, slope efficiency (with respect to incident pump power), and maximum Cr^{2+} output power for each of the experiment cases. The results for the 8-pass experiment are also shown for reference (the first row only). The highest

Table 6-2. Disk Laser Performance

Disk	Pumping	Cavity (cm)	Output Coupler	Threshold (W)	Slope Eff. (%)	Output (W)
1 mm	8-pass, Q-sw, 2.06 μm	8	90%R, 10 cmcc	0.612	50	4.27
1 mm	Q-sw., 1.89 μm, 7 M^2	10	97%R, 10 cmcc	0.31	31	1.41
1 mm	Q-sw., 1.89 μm, 7 M^2	9	90%R, 10 cmcc	0.83	39	3.1
1 mm	Q-sw., 1.89 μm, 20 M^2	9	90%R, 10 cmcc	0.76	38	3.3
1 mm	Q-sw., 1.89 μm, 7 M^2	9	85%R, 20 cmcc	0.85	35	1.9
0.5 mm	CW, 2.06 μm, 7 M^2	11	97%R, 10 cmcc	1.2	22	1.4
0.5 mm	Q-sw., 2.06 μm, 7 M^2	8	90%R, 10 cmcc	2.2	~0	0.005
0.5 mm	CW, 1.89 μm, 7 M^2	10	97%R, 10 cmcc	2.3	14	0.4
0.5 mm	Q-sw, 1.89 μm, 7 M^2	10	97%R, 10 cmcc	0.18	34	1.64
0.5 mm	Q-sw, 1.89 μm, 7 M^2	8	97%R, 10 cmcc	.25	40	4.1

efficiency Q-switched experiments agreed quite well with the predictions of the 1-D laser model, using 3% for the loss in the 0.5-mm disk and 5% for the loss in the 1-mm disk. The CW results were disappointing, however. Slope efficiencies were half that of Q-switched excitation for the 0.5-mm disk, and the 1-mm disk never lased CW at all. A comparison of the results to the 1-D model is shown for selected cases in Table 6-3, again with the 8-pass results in the first row for reference.

Table 6-3. Comparison of Disk Laser Results to 1-D Model Predictions

Resonator	Measured Threshold	Measured Slope Efficiency	Predicted Threshold	Predicted Slope Efficiency (%)
8 pass, 1-mm disk, 90%R Q-sw	7.8 mJ/cm^2	50%	8.8 mJ/cm^2	54%
1-mm disk, 97%R, Q-sw	4.9 mJ/cm^2	31%	5 mJ/cm^2	27%
1-mm disk, 90%R, Q-sw	13 mJ/cm^2	39%	9.4 mJ/cm^2	50%
1-mm disk, 85%R, Q-sw	13.4 mJ/cm^2	35%	11.9 mJ/cm^2	61%
0.5-mm disk, 97%R, Q-sw	3.9 mJ/cm^2	40%	3.8 mJ/cm^2	36%
0.5-mm disk, 97%R, CW	190 W/cm^2	22%	460 W/cm^2	38%
0.5-mm disk, 97%R, CW	360 W/cm^2	14%	460 W/cm^2	36%

The Q-switched results generally showed better agreement to the 1-D model, but certain cases of the Q-switched results and all of the CW results showed the phenomenon of reasonable threshold but poor slope efficiency. For the high Q resonators with 10-cmcc output mirrors and Q-switched pumping, the correspondence to the model was within the variability seen by simply translating the disks transversely to change the pumped location. That variability was likely due to small changes in loss and absorption of the pump laser caused by the disks being of non-uniform doping. All the other results showed the phenomenon of reasonably good agreement on threshold but slope efficiency significantly worse than expected. It is suspected that poor mode overlap is to blame for the low efficiency that occurs simultaneously with reasonable threshold values.

Results of the 16-pass experiment yield the following observations:

1. The disk laser was capable of producing over 4 W with 40% or better slope efficiency from each disk, for Q-switched pumping, coming close to the power

handling design goal of 5 W despite the low pump laser power of no more than 12 W entering the 16-pass system.

2. The disks were indeed of good quality, as good results were obtained using high Q resonators for both disks. Based on the slope efficiency values, there was less than 5% loss in the 1-mm disk and less than 3% in the 0.5-mm disk.
3. Laser performance for Q-switched pumping with a 10-cmcc output mirror and 8-10 cm cavity length agreed well with modeling predictions. Laser performance using longer radius mirrors or CW pumping did not agree well with the modeling predictions, showing significantly lower slope efficiency than predicted.
4. It was not possible to make a resonator that could efficiently extract the power from the entire pumped volume in the disks without being multi-mode and high Q. The most efficient resonators had small fundamental-mode sizes and tolerated wide variation in thermal lensing. Attempts to increase the size of the cavity mode to enable single mode operation always resulted in lower laser efficiency, something which the simple laser modeling used in this research did not predict. A likely cause of this problem is thermal lensing aberration, which was eventually found to exist under the pumping conditions found in this experiment.

6.5 Mode-Coupling Experiment

A second experiment was performed to determine the cause of the surprisingly low efficiencies found in certain resonator configurations of the power-handling experiments. It was suspected that the high variability in Cr^{2+} laser efficiency seen over the many disk laser experiments was due to mode-matching or diffraction problems, perhaps caused by

aberrated thermal lensing, which was suspected to be present in the pumped Cr^{2+}:ZnSe laser disks.

The experiment entailed constructing a simple standing wave Cr^{2+}:ZnSe laser resonator and changing the resonator length while measuring resonator output power and transverse beam mode shape. The experiment setup (see Figure 6-13) consisted of the Cr^{2+}:ZnSe disk laser gain module (1-mm thick Cr^{2+}:ZnSe disk on its heat sink, plus the 16-pass pumping optics and the 1.89-μm Tm:YLF pump laser), three cavity mirrors, and an optical rail.

The Cr^{2+} resonator was configured as a standing wave cavity, consisting of the Cr^{2+}:ZnSe disk on one end, a 50-cmcc folding mirror positioned 50 cm from the disk, and a flat 97%R output coupler placed *X* cm away from the folding mirror. The 50-cmcc folding mirror and the thermal lens present in the Cr^{2+}:ZnSe disk provided stability. Cavity mode size was controlled by adjusting the position *X* of the output mirror. The output mirror was mounted on an optical rail, allowing *X* to be changed without disturbing cavity alignment. To minimize the variables in this experiment, the pump laser power was kept at 5 W (Q-switched at 10 kHz) with a 0.4-mm radius pumped spot at the same location on the laser crystal throughout the entire experiment.

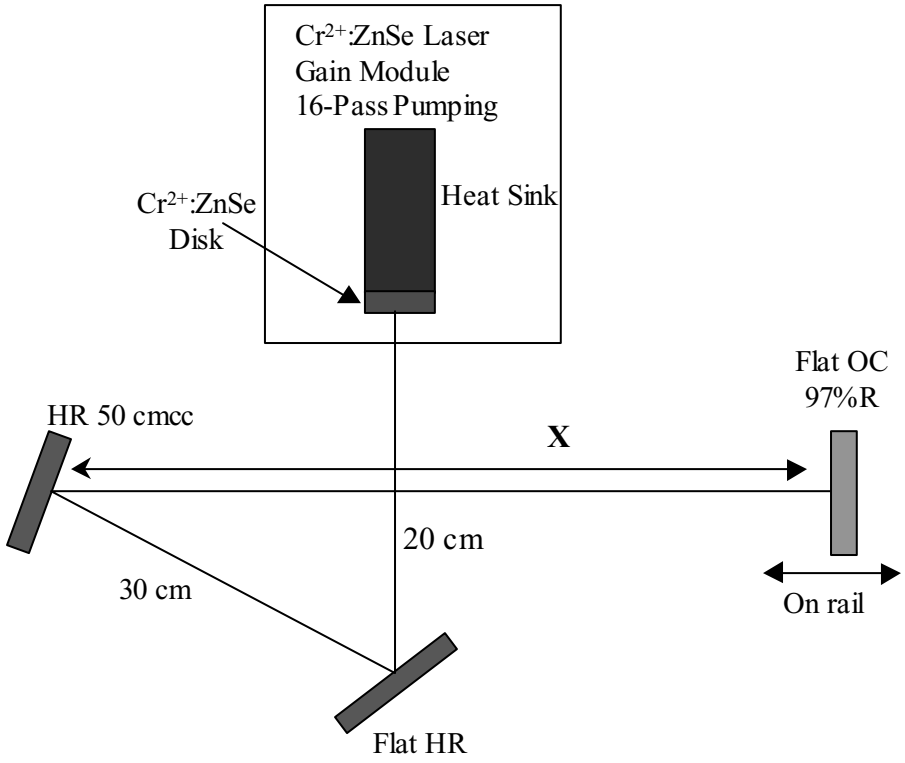

Figure 6-13. Configuration of Mode-Coupling Experiment

The results of the experiment were surprising. As expected, given the previous dismal performance of long cavities, the laser efficiency was poor, about a factor of two less than the ~27% predicted by the ideal laser model and verified by 16-pass laser experiments using a short, multi-mode cavity. The laser exhibited two completely different stable modes of operation, however, accessed at different ranges of output mirror displacement. Ray-trace stability analysis indicated this should not occur for a fixed thermal lens focal length in the disk. Figure 6-14 shows a scan of output power vs. mirror location (for 5 W, Q-switched pumping). The laser operated over a range of output mirror positions from X = 40 cm to X = 60 cm.

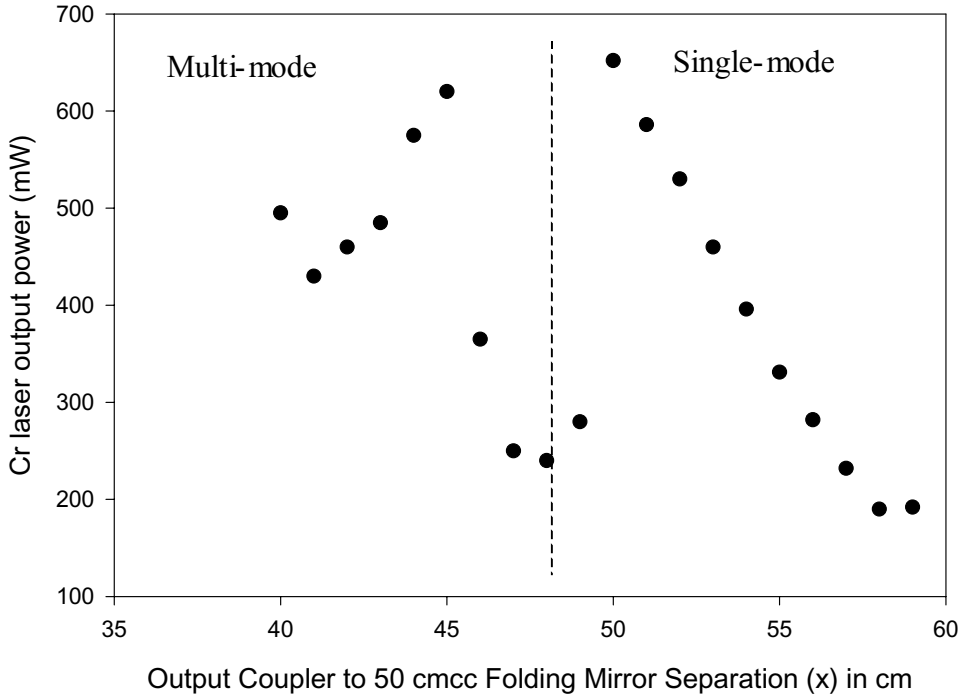

Figure 6-14. 1-mm Cr^{2+}:ZnSe Disk Laser Output Power as a Function of Output Mirror Position, 5-W Tm:YLF Pumping, 97%R Output Mirror
The laser worked from X=40 cm to X=60 cm, with multi-lobed beam shape for X<50 cm and single-lobed beam shape for X>50 cm. Given a fixed focal length thermal lens, stability analysis predicts the cavity should lase for either X<50 cm or for X>50 cm, depending on the thermal lens focal length, but not for both.

A simple ray tracing stability/mode-radius calculation shown in Figure 6-15 predicts that the laser should run for approximate output mirror positions of either 40 cm to 50 cm or 50 cm to 60 cm, depending on the strength of the thermal lensing, but not for both, assuming a constant thermal lens strength. If the single-pass thermal-lens focal length in the laser disk is longer than 25 cm, the laser theoretically should be stable for X<50 cm. If the thermal lens focal length is shorter than 25 cm, the laser theoretically should be stable for X>50 cm.

The required optics were not available to allow thermal lens focal length to be measured while lasing, so thermal lens focal lengths had to be estimated in the generation of Figure 6-15. The thermal lens was easy to estimate for the right side of the plot (X>50 cm). The fact that the cavity stopped lasing at an output mirror position of 58 cm was consistent with a thermal lens focal length of 6 cm. There was no equally convenient way to estimate a thermal lens focal length that would result in stable operation for X<50 cm. It was assumed that the thermal lens would be close to the minimum focal length allowed, so a 26-cm focal length was chosen. The large difference between the focal lengths required to generate each half of Figure 6-15 is suspicious, as it does not seem realistic. It is likely that the Cr^{2+} laser is operating in the presence of something not taken into account in simple ray-trace stability analysis, and that the thermal lens assumptions used to generate the plot must be viewed with suspicion. However, as the cavity mirrors were not spontaneously changing in curvature or reflectivity, and the pumping conditions were not changing, the cause of this phenomenon was thought to be involved with thermal lensing somehow, by process of elimination.

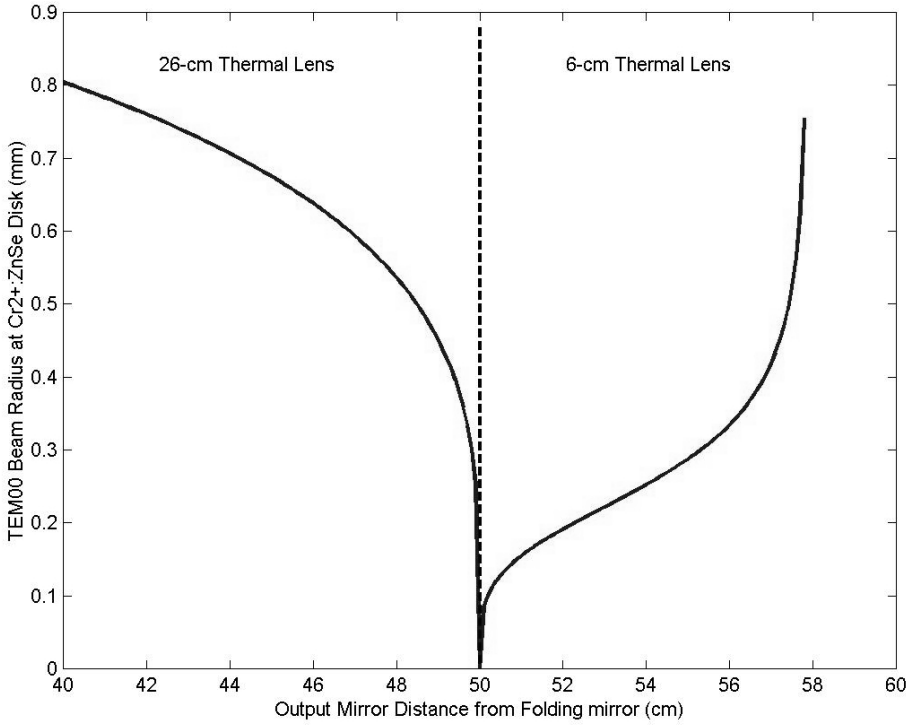

Figure 6-15. Diameter of Fundamental Cavity Mode vs. Output Mirror Position This is a composite plot showing the cavity mode radius and stable cavity operating range predicted by Gaussian beam analysis for two different thermal lens focal lengths in the laser disk, in an attempt to describe what might be happening in this laser experiment. A thermal lens focal length of longer than 25 cm resulted in stable operation for X<50 cm, the left half of the plot. A thermal lens focal length shorter than 25 cm resulted in stable operation for X>50 cm, the right side of the plot. The reasons for choosing 26-cm and 6-cm focal lengths in this plot are described in the text.

In addition to the puzzling stability range was the curiously poor efficiency of the resonator and its dependence on output mirror position. Figure 6-15 seems to indicate that the stable resonator for weak thermal lensing should be considerably more efficient in extracting the power from the ~0.5-mm radius gain region than the stable resonator for strong thermal lensing due to much better mode overlap. Figure 6-14 shows that the stable resonator for strong thermal lensing in fact extracted more power from the gain

region, at least over a limited range of output mirror positions (X~50 cm to 51 cm), where the mode overlap is predicted to be quite poor. Obviously mode-overlap alone does not adequately describe this situation, and a factor of three or more variation in thermal lensing for two different lasing configurations is not reasonable either.

A possible explanation for the puzzling behavior of this laser is that thermal lens aberration is responsible for the laser cavity being stable for both X<50 cm and X>50 cm under otherwise indentical resonator conditions. The absorbed power density estimate of Figure 6-9 shows a transverse dependence approximating a 4^{th} order Super-Gaussian function with ~0.4-mm radius. This produces a non-parabolic transverse refractive index gradient in the laser disk, which results in a non-parabolic thermal lens, i.e. aberration. For this kind of absorbed power distribution, annular regions of the laser disk farther from the center of the pumped spot experience less overall thermal lensing than those annular regions closer to the center of the pumped spot. Perhaps this effect is strong enough in the laser disk to allow cavity modes of different diameter to experience different average thermal lens focal lengths under otherwise identical resonator conditions. If this is true, then the poor efficiency of the resonator can be explained by diffraction loss and poor mode overlap caused by the aberrated thermal lensing.

To figure out what was happening in this resonator, the transverse beam-intensity profile of the laser output was recorded over a range of output mirror positions. The Cr^{2+} laser output intensity profile was captured by an ElectroPhysics PV-320 thermal imaging camera connected to a computer-controlled frame grabber. Beam profile images were taken at a series of output mirror positions, (the same positions used for the output power

measurements). No imaging lenses were used; the camera was simply placed in the (suitably attenuated) output beam, 105 cm from the 50-cmcc folding mirror.

The beam images are shown in Figure 6-16. Single-transverse mode operation occurred for X>50 cm and multi-mode operation occurred for X<50 cm. This is surprising, because the mode radius calculation would in fact predict the opposite effect. Looking at the beam profile images provided clues to what was going on. For X<50 cm, a large diameter mode oscillated, but with considerable aberration shown in the severely multi-mode intensity distribution. This mode should not have oscillated at all, if strong thermal lensing were present. But strong thermal lensing had to be present, as the laser also oscillated for X>50 cm. The output for X<50 cm suggests a hole in the center of the cavity-mode intensity distribution, as if there were some lossy element or damage in the middle of the gain region. Since the same spot lased for X>50 cm, showing maximum intensity distribution at the same location as the hole was for X<50 cm, actual crystal loss or damage was ruled out.

The beam profile images support the thermal lens aberration hypothesis. If a strongly aberrated thermal lens were present in the laser disk, it would act as central diffraction loss for the large diameter cavity mode stable for X<50 cm, producing a large diameter output beam with a central hole. The aberrated thermal lens would also act as a soft aperture preventing multi-mode operation in the configuration for X>50 cm, resulting in an output beam of much smaller diameter than the gain region. The end result for both cases would be reduced laser efficiency, as seen in Figure 6-14. The beam profile images support this idea, as the images corresponding to the highest-efficiency output for X<50

cm show large diameter output with multiple lobes and central holes, and the images for X>50 cm show small diameter, single-lobed output.

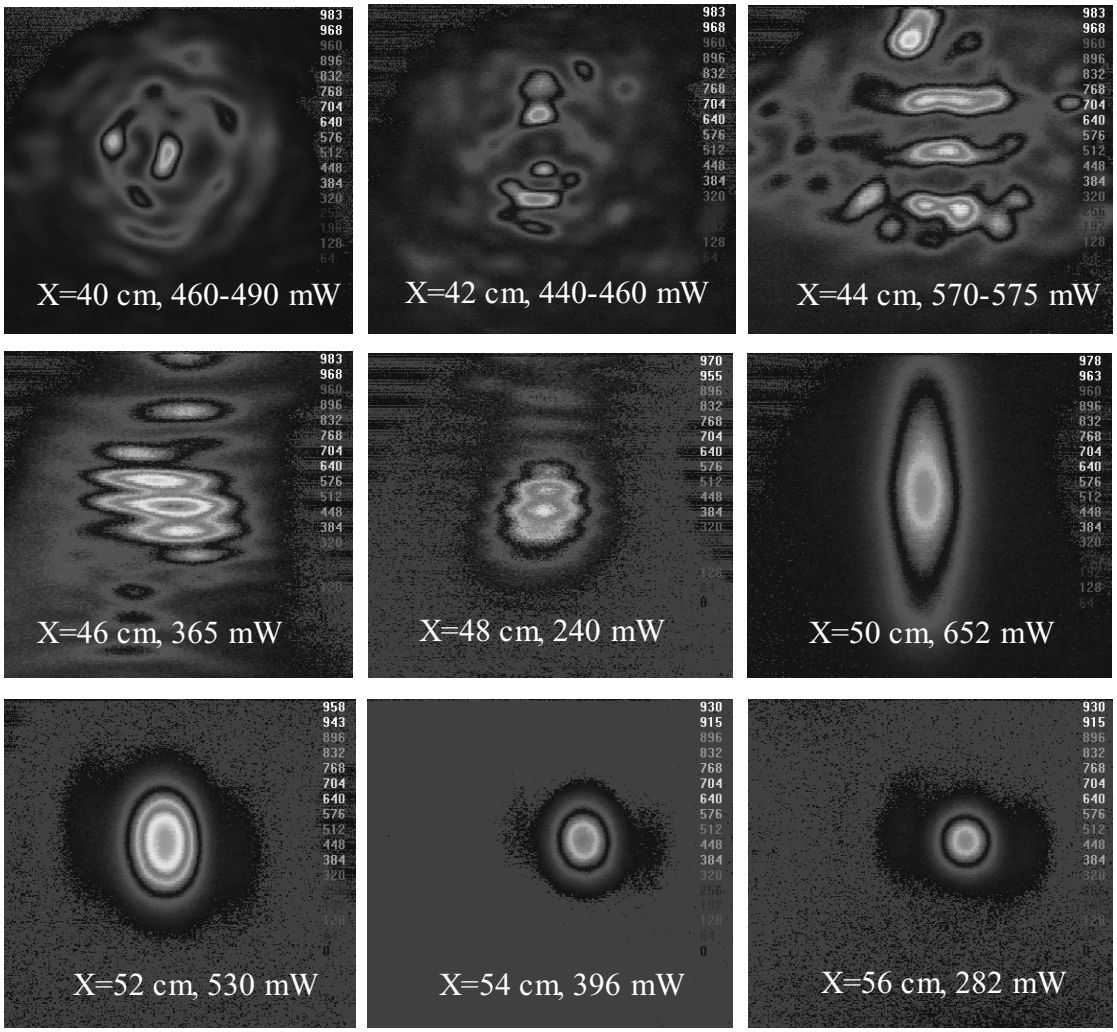

Figure 6-16. Cr^{2+}:Disk Laser Beam Profiles for Different Output Mirror Positions

The low efficiency seen in many of the Cr^{2+}:ZnSe disk laser experiments could be explained at least in part by diffraction loss or poor mode overlap caused by aberrated thermal lensing in the disks. The thermal lens aberrations simply prevented efficient extraction of all the gain in the pumped spot on the disk for any fixed resonator design tried in the experiments. In conditions of severe thermal aberration, a highly multi-mode

resonator with large tolerance for changes in thermal lens focal length and low mode selectivity would have the best change of efficient operation. This kind of resonator has been used in these experiments, the cavity with a 10-cmcc output mirror and 8-10 cm cavity length, and it did indeed produce the highest efficiency output. Unfortunately, if TEM_{00} operation is required, there is nothing to do but either accept the efficiency penalty or somehow reduce the thermally induced aberration significantly.

6.6 Summary

A Cr^{2+}:ZnSe disk laser was constructed and shown to work well under certain conditions. The design goal of 5 W was almost achieved, and would have been if the pump laser had produced more output power. The construction was surprisingly easy, and everything worked for the most part as designed. Mounting the disks on heat sinks and building (and aligning) the pumping systems were a little complicated, but not difficult. The disk laser resonators were easy to construct and align, due to the off-axis pumping.

The laser experiments showed that the Cr^{2+}:ZnSe disk laser worked well in multi-mode resonators with Q-switched pumping, short cavity lengths, and fairly high Q. The results from these cases agreed well with the predictions of the laser dynamics model. Slope efficiencies of 40-50% and pulsed average output powers of up to 4.1-4.3 W at 2.5 μm were achieved in both disks in a hemispherical high-Q standing-wave resonator using a 10-cmcc output mirror and Q-switched pumping. Unfortunately, deviations from the above conditions (including using CW pumping) resulted in significant reduction in laser efficiency that did not correspond to the qualitative predictions of the simple laser

stability and mode overlap modeling done in the laser design phase. A likely explanation is that thermal lens aberration was present in the laser disks, preventing efficient extraction of all the pump power absorbed in the gain region when CW or TEM_{00} operation was attempted. Reducing the aberration of thermal lensing in the disks should significantly improve the efficiency of TEM_{00} or CW laser operation. This would require obtaining usable 0.25-mm disks; devising a mounting method that is better than epoxy, and is suitable for delicate disks but prevents disk warpage; and making a pumping system that produces a radially uniform absorbed power distribution in the laser disks. Or, with more pump power available, a larger pump beam diameter could be used with 0.5-mm and 1-mm disks. If those conditions could be met, there should be nothing preventing the Cr^{2+} disk laser from achieving the good performance predicted by simple modeling.

7 Thermal Characterization of Cr^{2+}:ZnSe Disks

The Cr^{2+}:ZnSe laser disks were thermally characterized in order to provide feedback on how well the disk laser scheme had handled the undoubtedly significant, but largely unknown thermal effects. Both modeling and experiments were employed. The modeling consisted of running a finite-element analysis routine (ABAQUS) using a simple disk model to determine temperature distributions and corresponding thermal lens powers as a function of disk thickness and pump beam distribution. The experiment entailed using a phase-shifting interferometer to measure the optical path length differences occurring in pumped Cr^{2+}:ZnSe disks due to non-uniform temperature profiles (thermal lensing). This chapter presents results of both modeling and experiments, and finally a comparison between the two.

7.1 Thermal Modeling

Modeling the heat transfer within the pumped Cr^{2+}:ZnSe disks was performed both to aid the interpretation of experimental findings and to see if the thermal behavior of the Cr^{2+}:ZnSe disks corresponded closely enough to the models to make predictive modeling a useful design tool. This section discusses the thermal models, choice of pumping conditions, the modeling results, and an interpretation of the results.

7.1.1 Thermal Models

It was clear from the start that the three dimensional nature of the heat flow in the Cr^{2+}:ZnSe disks did not lend itself to a nice closed form solution. Therefore, a commercial finite-element-analysis software package called ABAQUS was employed to make the problem manageable. The thermal models used with ABAQUS were very

simple. Steady state heat transfer was assumed, with no thermal transport by radiation. No structural dynamics were modeled. The model of a laser disk consisted of a slab of ZnSe with one face having a constant temperature of 20 C (the heat sink), and the other faces being insulated. Optical pumping was simulated by an applied volumetric heat source which was uniform along the axis (thickness) of the disk, but varied transversely to match the transverse intensity distribution of the pump laser beam. In effect, this built an assumption into the modeling that the amount of pump light converted to heat was constant as a function of disk temperature. Of course, this is not true, but accounting for varying thermal loading with temperature in ABAQUS proved too difficult to attempt in the time available for this simulation effort. Since the model was linear, only one value of heat source power was needed; the results of applying a different heat source power (with the same spatial distribution) would be linearly dependent.

The model assumed that the thermal interface between the disk and the heat sink was of low thermal resistance, thermal stress was not significant enough to need to be modeled, and that heat loss through the disk surfaces exposed to air was negligible. Although in reality these assumptions might not be completely valid, the values of the parameters needed to accurately model the 'real world' cases of imperfect thermal interfaces, thermal stress, and weak air convection in the laser disks were not known. It was much simpler and cleaner to just model the ideal case and compare it to the experimental results.

Although the underlying model geometry, boundary conditions, and heat source inputs were continuous functions, they had to be sampled at an array of points called

nodes before the numerical solution of the heat equation could be calculated. Ideally, the sampling density would be so high that the numerical solution would be free from error caused by using finite elements instead of true differential elements of infinitesimal dimensions. Unfortunately, finite computer resources and time constraints forced the sampling density to be fairly coarse. After many trials, a node spacing of 0.05 mm was selected. This node spacing was reasonably effective in adequately representing the transverse intensity variation of the 0.4-mm radius absorbed pump power distribution in the disks. With this 0.05-mm node spacing, it was found that the maximum practical crystal size that could be modeled was 3x3x1 mm^3 (which resulted in over 78,000 nodes). Thus, the models were of 3x3-mm^2 disks with different thickness (1.0 mm, 0.5 mm, 0.25 mm), all using the same node spacing of 0.05 mm.

7.1.2 Pumping Conditions

Three different thermal absorbed power density functions were modeled, each using two different beam radii, to determine how thermal lensing was affected by the diameter and intensity distribution of the pump laser beam. (Note that absorbed power density refers to power absorbed per unit volume). The three different density functions used are shown in equations (7-1), (7-2), and (7-3):

$$f_G(x,y,z) = \frac{2}{\pi W^2 T} e^{-\frac{2[(x-x_0)^2+(y-y_0)^2]}{W^2}} \tag{7-1}$$

$$f_{SG4}(x,y,z) \cong 0.799 \frac{2}{\pi W^2 T} e^{-\frac{2\left((x-x_0)^2+(y-y_0)^2\right)^2}{W^4}} \tag{7-2}$$

$$f_{SG50}(x,y,z) \cong 0.525 \frac{2}{\pi W^2 T} e^{-\frac{2\left((x-x_0)^2+(y-y_0)^2\right)^{25}}{W^{50}}} \tag{7-3}$$

where W is the beam radius, T is the disk thickness, x and y are transverse coordinates, and (x0,y0) marks the position of the pumped spot center. All of the absorbed power density functions varied in the transverse plane, but not along the longitudinal axis – a simple way to approximate the multiple passing of the pump laser through the laser disks. The transverse (x,y) dependence was modeled using Super-Gaussian functions, and the longitudinal (z) dependence of the absorbed power was assumed constant. The density functions were normalized such that a volume integral of the absorbed power density function over the entire disk would result in 1-W total absorbed power. (Note that (7-2) and (7-3) were normalized numerically). Applying a different power level was done by multiplying the density function by the desired power value.

The density function of (7-1) has a transverse Gaussian dependence, which represents the heating caused by a TEM_{00} pump beam. The density function of (7-2) has a transverse fourth order Super-Gaussian dependence, which represents the heating caused by a typical multi-mode pump beam or the 16-pass pumping system. The density function of (7-3) has a transverse 50^{th} order Super-Gaussian dependence, which represents an idealized 'top-hat' pump beam (which was what the disk laser design originally called for). The two beam radii used with these functions were 0.4 mm and 0.8 mm. Figure 7-1 shows cross sections of the three different absorbed power distribution functions, plotted through the peak for a 5-W heat load with 0.4-mm beam radius in a 1-mm thick disk.

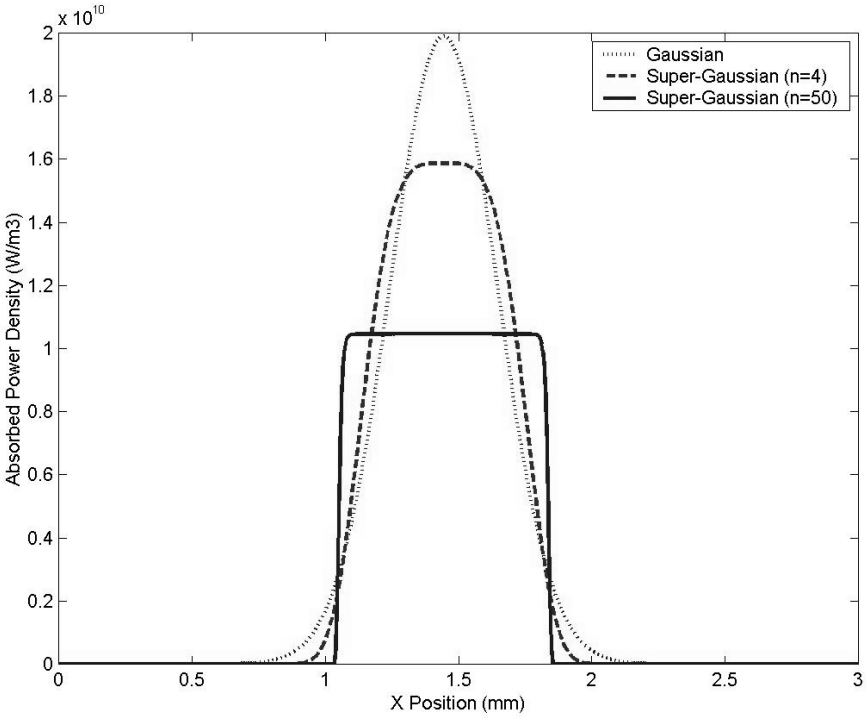

Figure 7-1. Cross Section of Modeled Absorbed Power Density in Laser Disk
This plot shows a transverse cross section of the three different absorbed power density functions used in this modeling effort to investigate the effects of variation in transverse intensity distribution of the input pump laser beam on thermal lensing. The plot is for 5-W input power into the 1-mm disk.

7.1.3 Modeling Results

The modeling results are cross sections of temperature distributions in the disks and estimated thermal lens focal lengths for the cases modeled. The output of ABAQUS was a three-dimensional array of temperature for each case. The 3-D temperature arrays were averaged along the longitudinal axis to provide the z-averaged temperature profiles needed for estimating thermal lens focal lengths. Thermal lens focal lengths were estimated from the z-averaged temperature data using a least squares curve-fitting routine discussed in detail in 7.2.3.

Before discussing thermal lens focal lengths, it is useful to investigate the temperature distributions the model predicted would occur in the laser disks. Figure 7-2 shows longitudinal variation in temperature at the center of the pumped spot for the three disk thickness values modeled. The plot shows the temperature rise above heat sink temperature per watt of absorbed pump power (using 0.4-mm radius Gaussian pumping). Notice that the peak temperatures reached in each disk were fairly comparable. Thus changing disk thickness alone did not significantly affect peak temperatures reached in

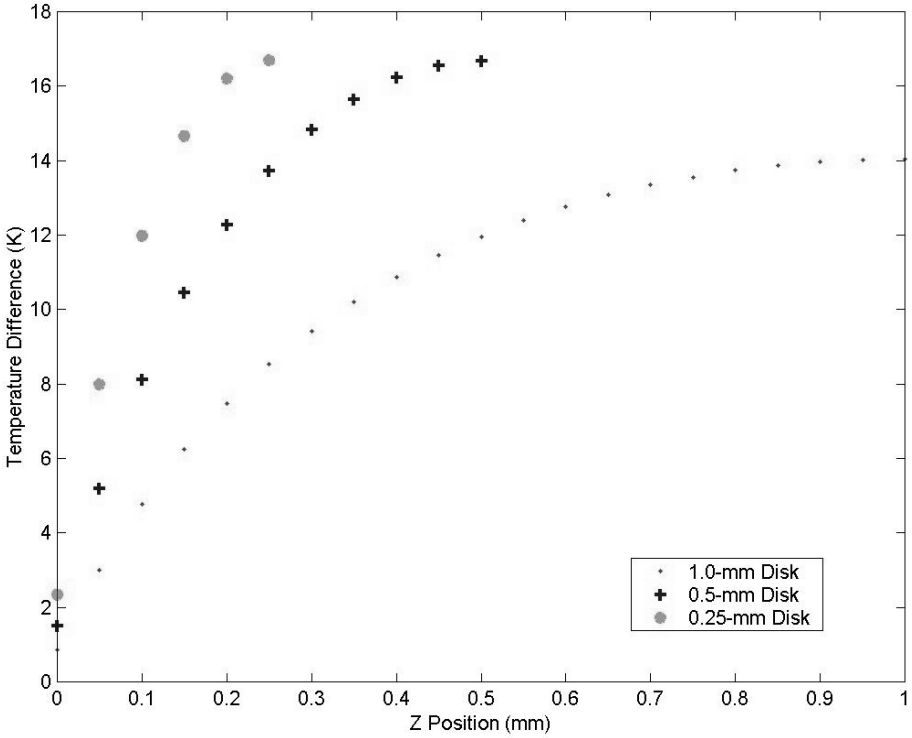

Figure 7-2. Axial Temperature Distribution in Cr^{2+}:ZnSe Disks
This plot shows how temperature starts off at the heat sink temperature (0 K temperature difference) at the heat sink (at z = -0.05 due to an ABAQUS idiosyncrasy), and rises as the input face is approached. This plot is for 1 W of heat input, using the Gaussian power density and 0.4-mm beam radius.

the disks. This effect held for all the pumping distributions, and therefore the full array of those results is not shown.

In order to calculate thermal lens focal lengths, and indeed to aid in interpreting the 3-D temperature information, the temperature arrays were averaged in the z direction to produce 2-D arrays of (z-averaged) temperatures. Figure 7-3 shows a plot of z-averaged temperature as a function of transverse position on the disk, for 5-W heat load with Gaussian distribution, 0.4-mm radius, and 1-mm disk thickness. It does appear that the 5-W heat load makes the center of the pumped spot get quite hot.

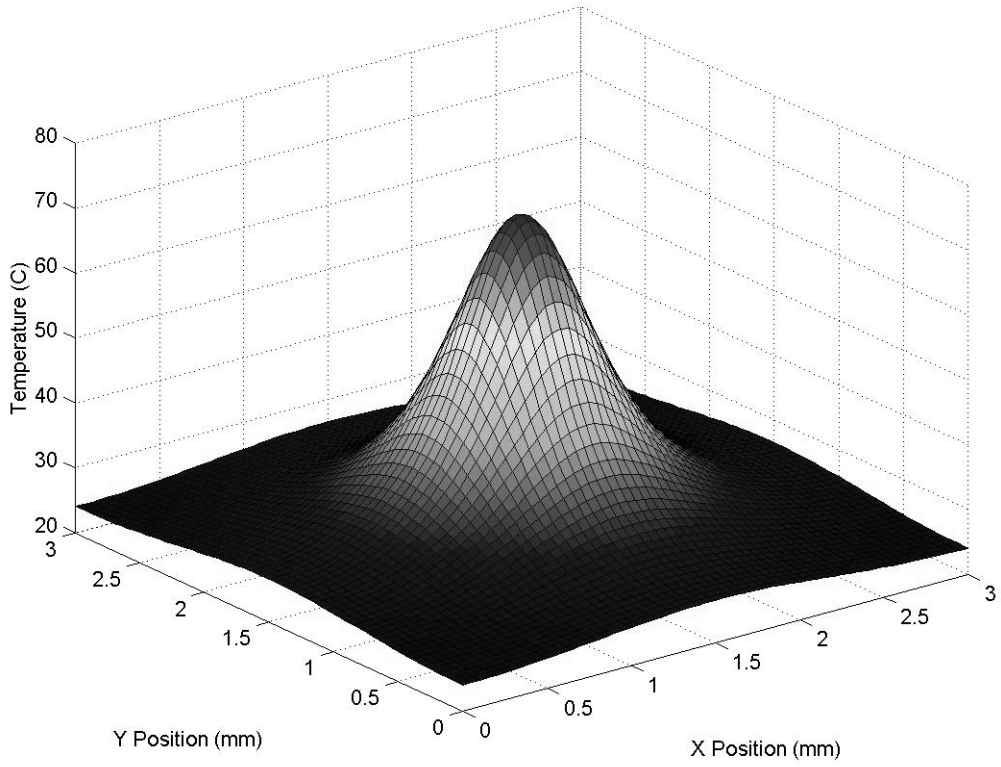

Figure 7-3. Z-Averaged Temperature in 1-mm Disk, 5-W TEM_{00} Pumping
This plot shows the longitudinally averaged temperature distribution in the 1-mm Cr^{2+}:ZnSe disk, predicted by ABAQUS for 5-W pumping with a 0.4-mm radius Gaussian beam. Z-averaged temperatures as high as 70°C are predicted in the center, for a 20°C heat sink temperature.

Table 7-1 shows the variation of longitudinally (z)–averaged temperature at the center of the pumped region, per watt of pump power for the different pumping cases and disk sizes. On the average, the peak (z-averaged) temperature inside the Cr^{2+}:ZnSe disks increased at 10 K per watt of pump power for the 0.4-mm radius pump distributions and 5 K per watt for the 0.8-mm radius pumping. The disk thickness affected temperature profiles more significantly when it was thin in comparison to the pump beam diameter.

Table 7-1. Predicted Longitudinally-Averaged Temperature Rise at the Center of the Pumped Spot in Cr^{2+}:ZnSe Disks Per Watt of Absorbed Heat

Absorbed Power Distribution	Beam Radius	Max Temp, (z-avg.) 1-mm Disk (K/W)	Max Temp, (z-avg.) 0.5-mm Disk (K/W)	Max Temp, (z-avg.) 0.25-mm Disk (K/W)
Gaussian	0.4mm	10.5	11.9	11.6
	0.8mm	6.1	5.5	4.3
Super Gaussian (n=4)	0.4mm	10.6	12.0	11.4
	0.8mm	6.1	5.5	4.0
Super Gaussian (n=50)	0.4mm	9.6	10.3	9.1
	0.8mm	5.3	4.3	2.8

In the transverse (x,y) plane, the (z-averaged) temperature profiles changed slightly with changes in both disk thickness and absorbed pump power distribution. In general, the thinner the disk was relative to the radius of the absorbed power distribution, the more closely the temperature profile in the disk followed the shape of the absorbed power distribution. As an example, Figure 7-4 shows the transverse distribution of z-averaged temperature for the 1-mm disk using the three different pump power distribution functions with 5-W input power and 0.4-mm radius. Notice the temperature profiles are almost identical. In contrast, Figure 7-5 shows that the variations in temperature distribution in the 0.25-mm disk pumped with the three different 0.8-mm radius beams were readily apparent.

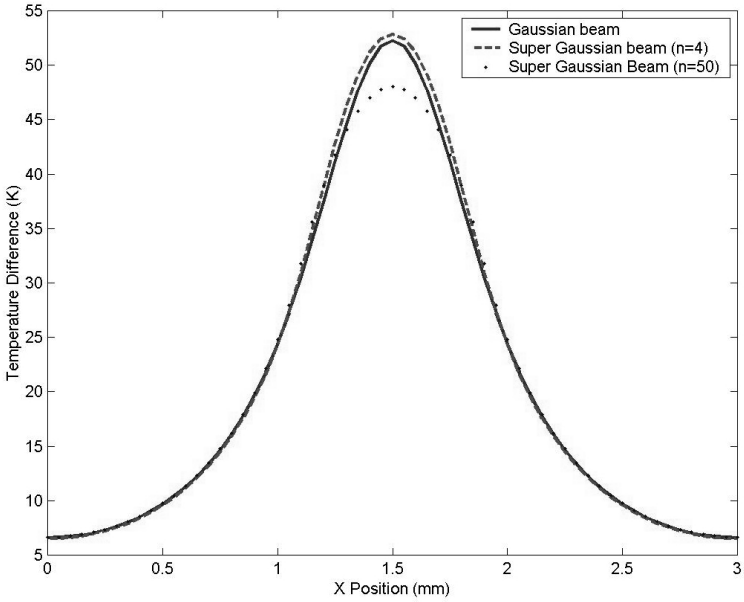

Figure 7-4. Cross-Section of Predicted Temperature Distributions in 1-mm Disk
This plot shows a cross section of predicted z-averaged temperature in the 1-mm Cr^{2+}:ZnSe disk, for Gaussian, 4th order Super Gaussian, and top-hat pumping at 5 W and 0.4-mm radius

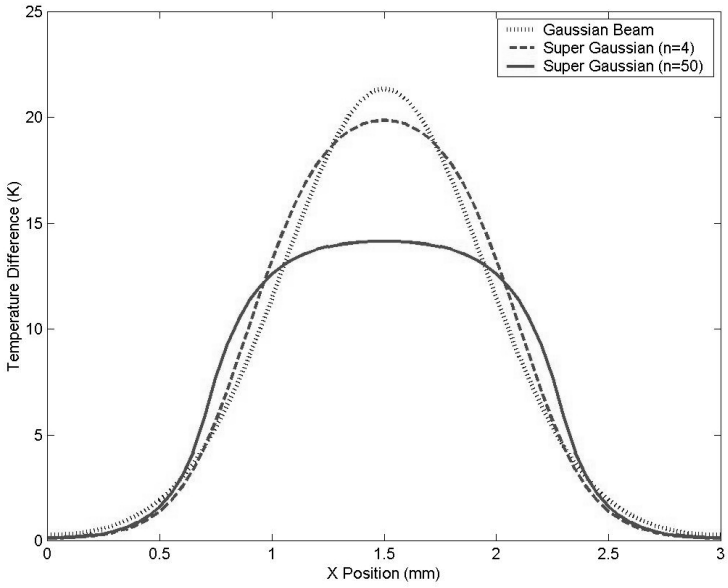

Figure 7-5. Cross-Section of Predicted Temperature Distributions in 0.25-mm Disk
This plot shows a cross section of predicted z-averaged temperature in the 0.5-mm Cr^{2+}:ZnSe disk, for Gaussian, 4th order Super Gaussian, and top-hat pumping at 5 W and 0.8-mm radius. Note the large variation in temperature distribution, compared to that of the 1-mm disk in Figure 7-4.

Thermal lens focal lengths were calculated by curve fitting a parabolic function to transverse phase difference matrices computed from z-averaged temperature data using the following expression:

$$\Delta\phi = \frac{2\pi}{\lambda} OPLD = \frac{2\pi L \Delta T}{\lambda} \frac{dn}{dT} \tag{7-4}$$

where $\Delta\varphi$ is phase difference, OPLD is optical path length difference, λ is light wavelength, L is the length of the optical path (2 times the disk thickness), ΔT is the z-averaged temperature difference, and dn/dT is the change in refractive index with temperature (70×10^{-6} for ZnSe). Further explanation of the process can be found in Section 7.2.3.

Since the disks are mirror coated on one side, the thermal lensing can be defined naturally in two ways, possibly leading to confusion: single pass or double pass. In this chapter the thermal lens focal length and lens power are calculated using the double-pass convention. This means that the total lens focal length is calculated for light traveling through the disk twice (since that is what happens in use). To convert these results to the single-pass convention, simply multiply the double-pass focal length values by two (or divide thermal lens power values by two).

The thermal lensing produced by the (z-averaged) temperature distributions in the disks is summarized in Table 7-2. Two different data window sizes, 0.5 mm and 1.0 mm, were used for the curve-fitting routine that estimated focal length from the arrays of z-averaged temperature. It was found that the best overall fits were obtained by using a data window of about half to three-quarters of the diameter of the absorbed power

distribution, but the 0.5-mm data window provided the most accurate fits at the center of the pumped spot. The information in the table is presented in terms of thermal lens power (in diopters) per watt of input pump power (heat load) for ease of interpretation, as it is then linearly dependent on pump power. The results for the 0.5-mm data window also plotted in Figure 7-6 and Figure 7-7.

Table 7-2. Modeled Thermal Lensing in Pumped, Nonlasing Cr^{2+}:ZnSe Disks

Abs. Power Distribution	Beam Radius	Lens Power (m^{-1}/W) 1-mm Disk		Lens Power (m^{-1}/W) 0.5-mm Disk		Lens Power (m^{-1}/W) 0.25-mm Disk	
		0.5 mm Fit	1 mm Fit	0.5 mm Fit	1 mm Fit	0.5 mm Fit	1 mm Fit
Gaussian	0.4 mm	8.6	4.3	6.6	3.0	4.1	1.6
	0.8 mm	2.1	1.6	1.4	1.0	0.65	0.46
N=4 S.G.	0.4 mm	8.5	4.6	6.4	3.2	3.8	1.7
	0.8 mm	1.7	1.6	0.94	0.93	0.33	0.38
N=50 S.G.	0.4 mm	5.7	4.2	4.0	2.9	2.0	1.5
	0.8 mm	0.88	0.93	0.38	0.45	0.065	0.12

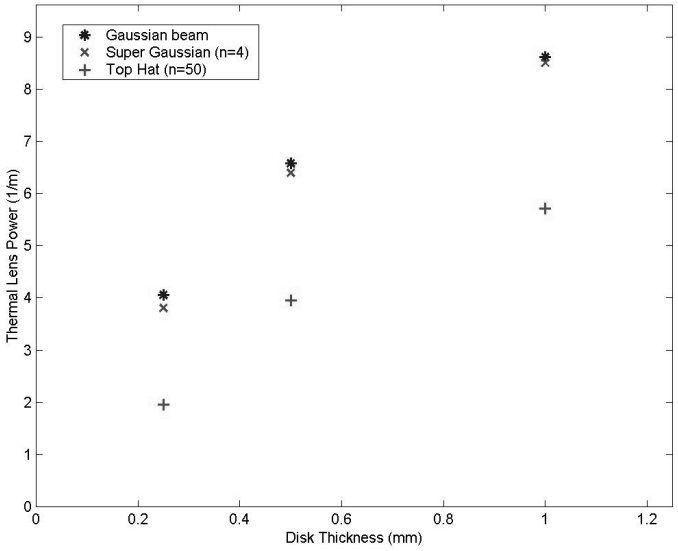

Figure 7-6. Modeled Thermal Lensing in ZnSe Disks, 0.4-mm Radius Pumping
This plot shows model predicted thermal lens power (1/f) for three disk thickness values and three different absorbed power density functions (Gaussian, 4th order Super-Gaussian, and top-hat), all with 0.4-mm radius. The plot is for 1-W heat load, so can be interpreted as thermal lens power per watt of heat load.

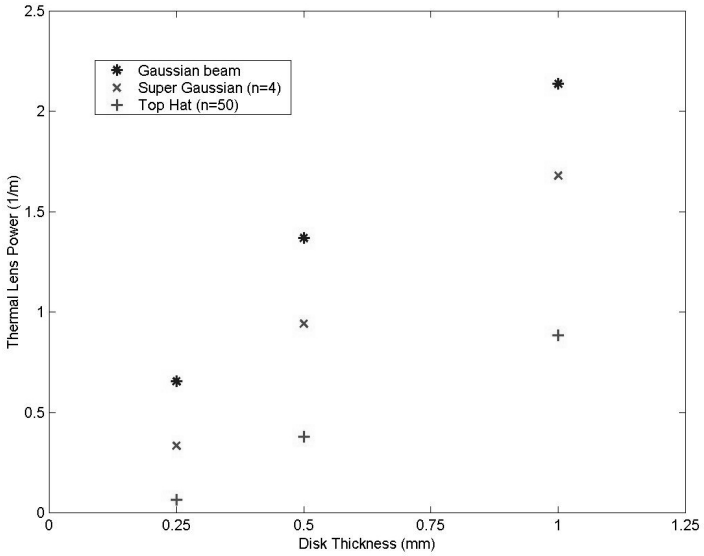

Figure 7-7. Modeled Thermal Lensing in ZnSe Disks, 0.8-mm Radius Pumping
This plot shows model predicted thermal lens power (1/f) for three disk thickness values and three different absorbed power density functions (Gaussian, 4th order Super-Gaussian, and top-hat), all with 0.8-mm radius. The plot is for 1-W heat load, so can be interpreted as thermal lens power per watt of heat load.

None of the data discussed so far shows how good the curve fits are and how aberrated the predicted thermal lensing is. Cross section plots of the phase difference function and the associated thermal lens curve fits are shown for selected cases to show that the thermal modeling does in fact predict thermal lens aberration. The plots of Figure 7-8-Figure 7-11 show the extreme limiting cases of the thermal lensing found in this modeling effort. A 5-W heat load is used for all four figures.

Figure 7-8 shows strong thermal lensing associated with 0.4-mm radius Gaussian pumping of the 1-mm disk, resulting in a 2.3-cm thermal lens focal length (double pass). Figure 7-9 shows the same disk pumped with a 0.4-mm radius top hat, resulting in a 3.5-cm focal length thermal lens. Note that the curve fit is better for the top-hat pumping, indicating less aberration than for Gaussian pumping. Figure 7-10 shows weak thermal

lensing associated with 0.8-mm radius Gaussian pumping of the 0.25-mm disk, resulting in a 44-cm focal length thermal lens, almost a factor of 20 longer focal length than for the 1-mm disk pumped with the 0.4-mm Gaussian. Some of this reduction is due to reduced disk thickness, and some of it is because the beam is wider. However, notice that the lensing is still aberrated, albeit weak. . Figure 7-11 shows that pumping the same 0.25-mm disk with a 0.8-mm top-hat results in virtual elimination of thermal lensing inside the pumped diameter of the disk, with thermal lens focal length of 166 cm.

Notice how the phase (temperature) distribution in the 0.25-mm disk more closely follows the pump intensity profile. It takes a beam diameter to disk thickness ratio greater than approximately 6:1 to achieve this. If uniform (top-hat) pumping is used with beam diameter at least 6 times the disk thickness, thermal lensing is nearly eliminated.

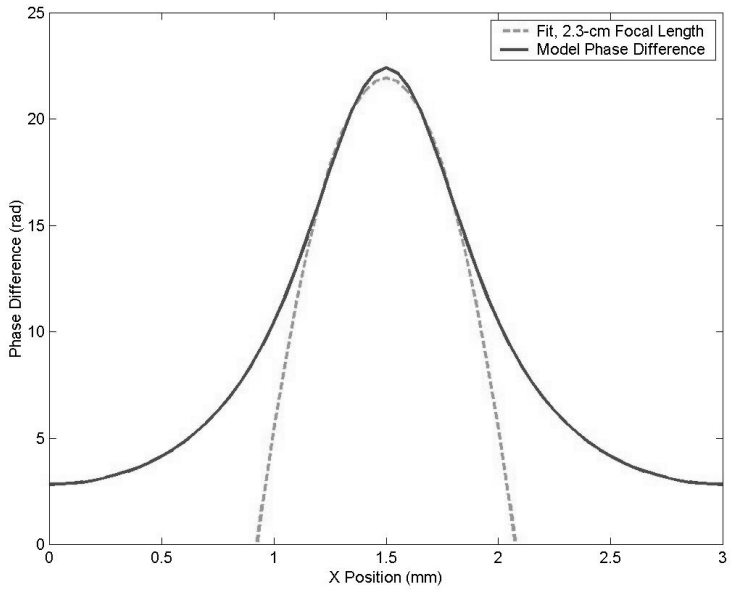

Figure 7-8. Thermal Lensing in 1-mm Disk, 5-W Gaussian Density, 0.4-mm Radius
This figure shows the predicted thermal lens focal length, 2.3 cm, in the 1-mm Cr^{2+}:ZnSe disk for the case of 5-W absorbed heat in a 0.4-mm radius Gaussian density.

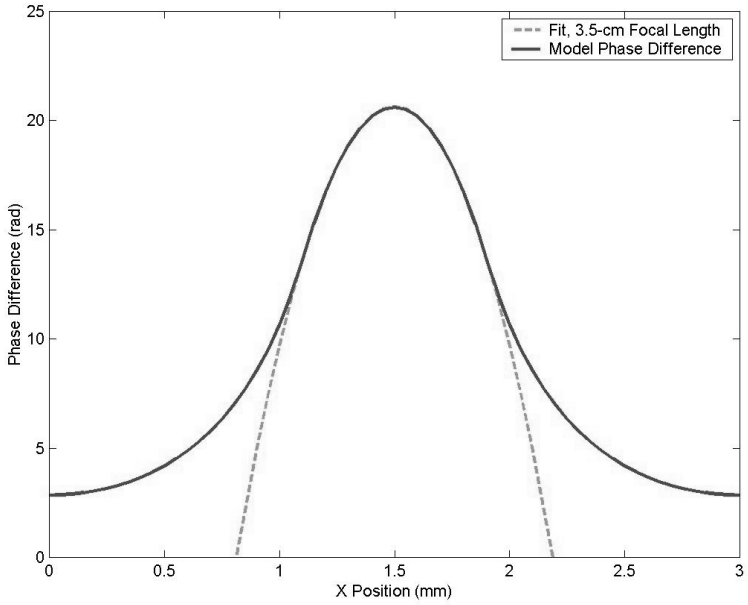

Figure 7-9. Thermal Lensing in 1-mm Disk, 5-W Top-Hat Density, 0.4-mm Radius
This figure shows the predicted thermal lens focal length, 3.5 cm, in the 1-mm Cr^{2+}:ZnSe disk for the case of 5-W absorbed heat in a 0.4-mm radius top-hat density.

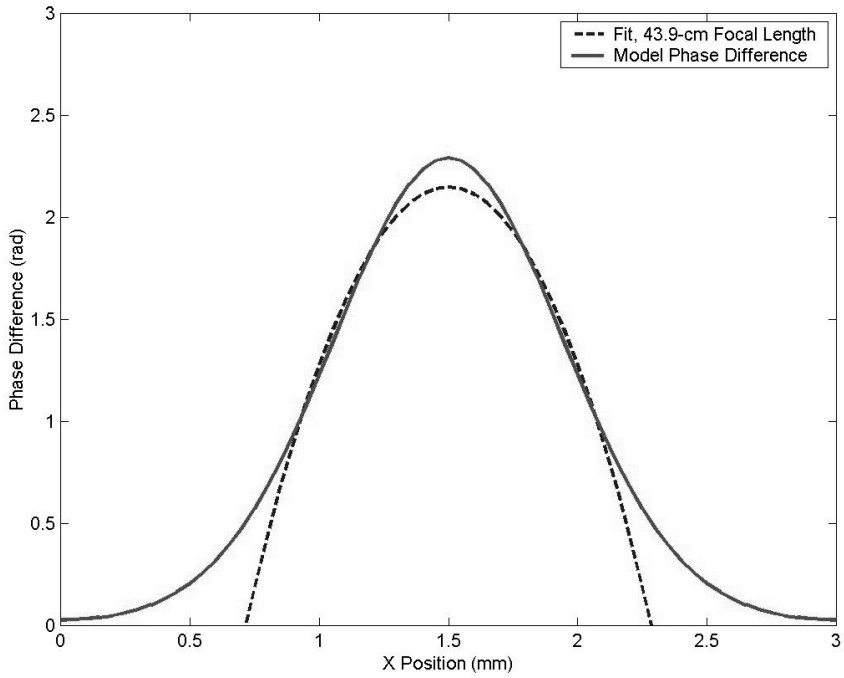

Figure 7-10. Thermal Lensing in 0.25-mm Disk, Gaussian Density, 0.8-mm Radius
This figure shows the predicted thermal lens focal length, 44 cm, in the 0.25-mm Cr^{2+}:ZnSe disk for the case of 5-W absorbed heat in a 0.8-mm radius Gaussian density

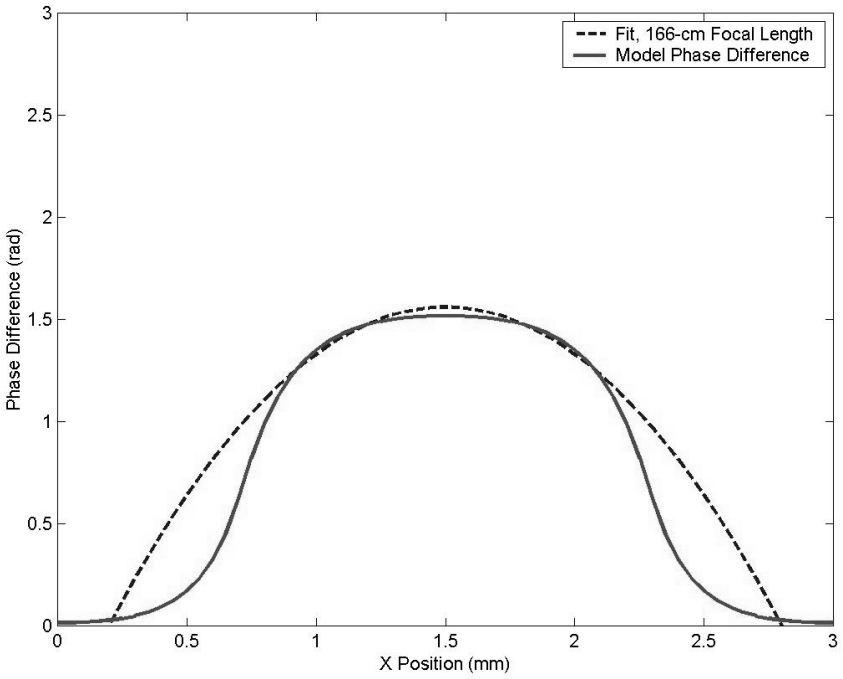

Figure 7-11. Thermal Lensing in 0.25-mm Disk, Top-Hat Density, 0.8-mm Radius
This figure shows the predicted thermal lens focal length, 166 cm, in the 0.25-mm Cr^{2+}:ZnSe disk for the case of 5-W absorbed heat in a 0.8-mm radius Gaussian density

Given that the laser experiments of Chapter 0 used primarily the 1-mm disk and 0.4-mm radius pumping, it can be safely said that the thermal modeling indicates that significant aberration should have been present in the laser disk. Whether this aberration is enough to cause the efficiency problems is an open question. Perhaps a more sophisticated thermal model incorporating temperature dependent thermal loading might provide further insight into this issue, but is was beyond the scope of this research, due to time constraints.

7.1.4 Interpretation of Modeling Results

The modeling results indicate several trends:

1. **The peak and average temperatures reached in a face-cooled laser disk do not depend strongly on disk thickness**. Unfortunately, if all the pump power is absorbed in the disk, the thermal gradient essentially doubles as the disk thickness is halved, doubling the stress on the crystal, but maintaining the same peak and average temperatures. Thus, reducing the disk thickness does not improve cooling efficiency and indeed increases likelihood of thermal fracture.
2. **It takes only a few watts of heat load to elevate the Cr^{2+}:ZnSe temperatures to the point where non-radiative relaxation is significant**. For the 0.4-mm beam size, a total heat load of 5 W resulted in the modeled peak (z-averaged) temperature in the disks being 50 K hotter than the heat sink – a condition which would result in ~40% reduction in laser gain at a heat sink temperature of 293 K. Of course, the exact heat load imparted to a Cr^{2+}:ZnSe disk per watt of absorbed pump power is not well known, and could vary from as little as 15% to as much as 90% or more, depending on disk temperature, the particular sample, and whether the disk is lasing or not.
3. **For a fixed pump power and beam radius, thermal lens power diminishes as the disk thickness is reduced.** In the limiting case of very wide pump beams and thin disks, one would expect thermal lens power to halve if disk thickness is halved, due simply to the reduction in optical path length and trend 1. Radial heat transfer has to be negligible for this limiting case to hold. It appears to take a disk at least six times thinner than the pumped diameter to approach this condition, judging from the results in Table 7-2. Nevertheless, at every disk thickness and

beam diameter modeled, the predicted thermal lens power significantly diminished as the disk thickness was reduced.

4. **The thermal lens power is reduced as the absorbed pump distribution is flattened.** The 50^{th} order super-Gaussian beam did result in significantly reduced thermal lensing compared to that with Gaussian pumping, especially in the thinner disks. Sadly, the 4^{th} order super-Gaussian distribution, which is typical of common multi-mode pump lasers, is not nearly flat enough to produce the reduced thermal lensing; it produced much the same thermal lensing as a perfect TEM_{00} Gaussian beam.
5. **Thermal lens power is virtually eliminated under the conditions of uniform absorbed pump power with a diameter that is greater than 6 times the disk thickness.** A 1-mm disk pumped with a 0.4-mm radius Gaussian pump beam has approximately 70 times the thermal lens power of a 0.25-mm disk pumped with a uniform top-hat beam with the same power but double the radius. Thus, although it takes more pump power to reach laser threshold if the beam diameter is expanded, and the laser becomes more sensitive to thermal lensing as the beam diameter is increased, the reduction in thermal lensing can be more than enough to offset these problems. The disk simply needs to be thin, compared to the diameter of the pump beam, and the pump beam needs to have a fairly uniform transverse intensity distribution. Actually, one would obtain nearly the same effect by using a pump beam with flat transverse intensity distribution that was the same diameter

as the disk. That method would not need the disks to be thin and could be an important discovery for future research.

7.2 Experimental Characterization of Thermal Effects

The thermal characterization experiment used phase-shifting interferometry to measure thermal lensing and temperature in two non-lasing Cr^{2+}:ZnSe disks pumped by the Tm:YLF laser and multi-pass pumping system.

7.2.1 Phase shifting interferometry

The term "phase shifting interferometry" refers to the technique of measuring the phase difference between two light beams. An interferometer with phase shifting capability records interference pattern images, and a computer analyzes the images to calculate phase difference. A typical configuration of the interferometer is shown in Figure 7-12.

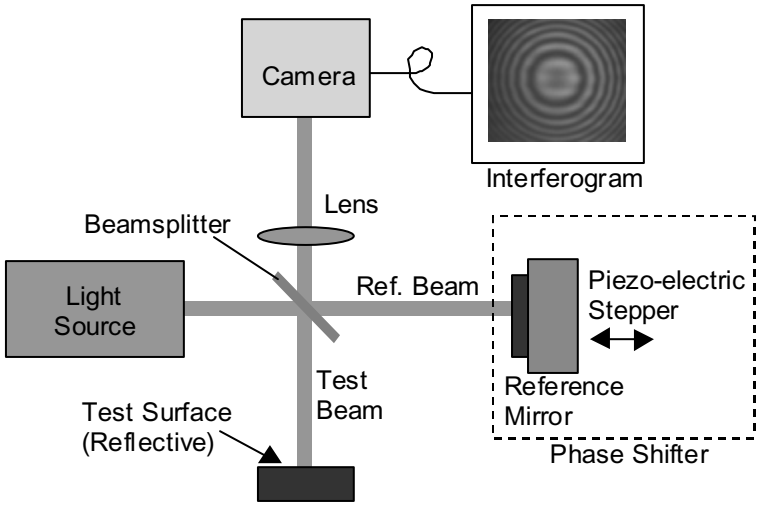

Figure 7-12. Schematic of Phase Shifting Interferometer
This is a typical Twyman-Green interferometer that has the reference mirror mounted on a piezo-electric device that can move the mirror longitudinally in controllable amounts, shifting the interference fringe pattern by changing the phase of the reference beam.

A light source is split by a beamsplitter into reference and test beams. The test beam illuminates the test surface, and is partially reflected back through the beamsplitter and onto a camera hooked up to a computer for image acquisition. The reference beam illuminates the reference mirror, is partially reflected back to the beamsplitter and then onto the camera. The camera (and computer-controlled frame grabber) records images which represent time-averaged interference between the reference and test beams at the "object" plane defined by the placement of the camera and imaging lens. Typically, the object(s) in focus will be the test surface and the reference mirror.

If the optical path length difference between the two arms of the interferometer is smaller than the coherence length of the light source, and the reference and test beam intensities at the camera are similar, then interference fringes with high contrast will be present in the camera images. The intensity pattern on the camera will have the functional form of

$$I_1(x,y) + I_2(x,y) - 2\sqrt{I_1(x,y)I_2(x,y)}\cos[\Delta\phi(x,y] \tag{7-5}$$

where I_1 and I_2 are test and reference beam intensities incident on the camera, and $\Delta\phi$ is the phase difference between the two beams.

Each interference fringe represents a 180° phase change between the reference and test beams, corresponding to a half-wavelength of optical path length difference. This difference could be caused by differences in surface topography between the reference and test surfaces, or by changes in the refractive index (or thickness) of the media through which the beams travel. The interferometer can therefore be used in reflection

mode to measure surface topography, or in transmission mode to measure changes in index of refraction such as thermal-optical effects.

Unfortunately, the basic interferometer allows only the magnitude of the optical path length difference to be measured, due to the cosine dependence of the interference pattern. The sign of the optical path length difference as well as its magnitude, can be determined using the phase shifting technique. With the reference mirror attached to a piezo-electric transducer (PZT), the optical path length of the reference arm can be changed precisely by a few optical wavelengths without affecting the test arm. As the reference mirror is moved, $\Delta\phi$ changes, shifting the fringes in the interference pattern seen by the camera. The direction of the shift of the fringe pattern gives the sign of the phase difference. For computerized data analysis, a quantitative method of performing this technique is needed. One approach is to record four interference pattern images with the PZT-induced phase shift increasing by $\pi/2$ for each successive image, and to post-process the images to obtain an estimate of $\Delta\phi$. The images are described by the following equations:

$$\begin{aligned} I_A(x,y) &= I_1(x,y) + I_2(x,y) - \sqrt{I_1(x,y)I_2(x,y)}\cos[\Delta\phi + 0] \\ I_B(x,y) &= I_1(x,y) + I_2(x,y) - \sqrt{I_1(x,y)I_2(x,y)}\cos[\Delta\phi + \tfrac{\pi}{2}] \\ I_C(x,y) &= I_1(x,y) + I_2(x,y) - \sqrt{I_1(x,y)I_2(x,y)}\cos[\Delta\phi + \pi] \\ I_D(x,y) &= I_1(x,y) + I_2(x,y) - \sqrt{I_1(x,y)I_2(x,y)}\cos[\Delta\phi + \tfrac{3\pi}{2}] \end{aligned} \tag{7-6}$$

These expressions differ only in the applied PZT phase shift. A little arithmetic results in an equation that can be solved for $\Delta\phi$', the so-call 'wrapped phase' function:

$$\frac{I_B(x,y)-I_D(x,y)}{I_C(x,y)-I_A(x,y)}=\frac{\sin[\Delta\phi(x,y)]}{\cos[\Delta\phi(x,y)]}=\tan[\Delta\phi(x,y)]$$

$$\Delta\phi'(x,y)=\arctan[\frac{I_B(x,y)-I_D(x,y)}{I_C(x,y)-I_A(x,y)}] \qquad (7\text{-}7)$$

The wrapped phase estimate $\Delta\phi$' is a piecewise-continuous approximation of the true phase difference $\Delta\phi$, but with all possible phase mapped onto the $[0,2\pi]$ range, the range of the inverse tangent function (hence the term 'wrapped phase'). Phase discontinuities arise in $\Delta\phi$' when the real phase difference $\Delta\phi(x,y)$ varies by more than 2π as a function of position. These phase discontinuities in $\Delta\phi$' must be removed in order to accurately reproduce $\Delta\phi$, a process called phase unwrapping.

Phase unwrapping can be difficult in general, but is a very simple process if the wrapped phase data meet certain conditions. The first condition is adequate sampling of what is in reality a continuous distribution. To accurately sample this distribution, the phase change between successive pixels on the camera must be less than π. The second condition is self-consistency; a path integral around any closed loop in the wrapped, sampled phase estimate $\Delta\phi'(x_i,y_j)$ must be zero. If the wrapped, sampled phase estimate meets these two conditions, then the phase discontinuities can be removed without introducing error. The reason is simple: given the above conditions, any phase change of π or more between successive pixels in the wrapped, sampled phase estimate matrix must be due to the 'wrapping' effect of the arctan function. Adding or subtracting the correct integral multiple of 2π phase to one of the pixels will minimize the phase difference between the two pixels – removing the 'wrapped phase' discontinuity. The

discontinuities in the entire wrapped sampled phase estimate matrix can be corrected in this way, stepping from one pixel to the next in a contiguous path. Once this process is complete, an estimate of the sampled true phase $\Delta\phi(x_i,y_j)$ is produced.

This phase unwrapping procedure is straightforward but gives good results only if the conditions of adequate sampling and self-consistency are met. In a lab table interferometer, this is usually achievable. The only problems end up being stray reflections, damaged camera pixels, damage spots on the optics, inadequate sampling around the edges of the image, and inadequate illuminating intensity. Simply using anti-reflection coated optics, avoiding bad spots on optics and mirrors, using an adequate illuminating light source, and using the appropriate magnification on the imaging system to ensure adequate phase sampling will minimize phase unwrapping errors.

Most of the remaining errors will be small and can be localized to small areas on the phase estimate matrix or removed by windowing or by comparing the phase estimates obtained using different phase unwrapping paths. If errors are still too great, then it is possible to take two sequences of interference patterns, with a 90 degree phase shift between sequences, and average the phase estimates produced from each sequence before performing phase unwrapping. (In its simplest form, only one more interference pattern image needs to be taken to do this, for a total of five 90 degree shifted images.) More sophisticated techniques to mitigate phase error exist, but these simple ones were found to be sufficient for this research.

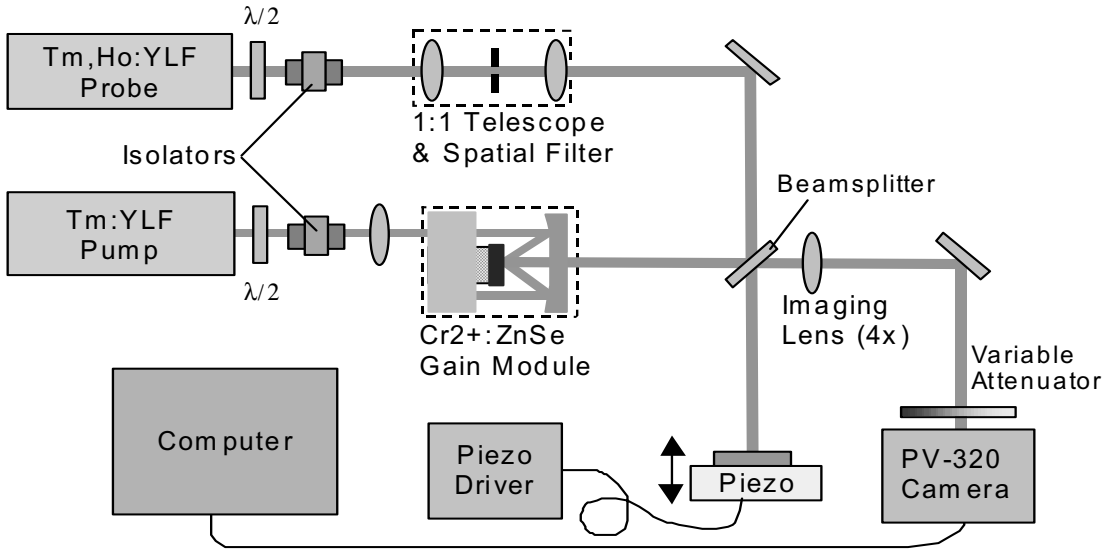

Figure 7-13. Schematic of Cr^{2+}:ZnSe Thermal Characterization Experiment
This setup consists of the 16-pass Cr^{2+}:ZnSe disk laser pump and gain module, and the phase shifting interferometer using a low power Tm,Ho:YLF probe laser as its light source. The output coupler of the Cr^{2+} laser had to be removed to perform this experiment, resulting in the thermal lens measurements being for non-lasing conditions.

7.2.2 Experiment Setup

The experimental setup, shown in Figure 7-13, consisted of a Cr^{2+}:ZnSe disk laser gain head, a Tm:YLF pump laser, a Tm,Ho:YLF probe laser, a Twyman-Green interferometer, and a computer for capturing and analyzing the data. The Cr^{2+}:ZnSe gain head itself consisted of a Cr^{2+}:ZnSe laser disk on a water-cooled heat sink, and the associated relay imaging optics used to obtain 16 passes of the pump light. Two disks were used in this experiment, the 0.5-mm and 1.0-mm thick disks used in the laser experiments in Chapter 0. The Tm:YLF pump laser produced up to 15 W at 1.89 μm, with $M^2 = 5$, for either CW or 10 kHz Q-switched operation. The multi-pass pumping produced a pumped spot with absorbed power distribution fairly well approximated by a fourth order "super-Gaussian" with 0.4-mm radius. The Tm,Ho:YLF probe laser was of

similar design as the Tm:YLF pump laser, but operated with low diode laser input power, resulting in a fairly stable 200-mW output beam at 2.06 μm. This laser was used because the probe needed to be at a wavelength for which the crystals were already coated, excluding more convenient 1-μm or 633-nm lasers. Tm,Ho:YLF was used instead of Tm:YLF in the probe laser to shift its wavelength away from the Cr^{2+}:ZnSe absorption peak of 1.75 μm. The probe laser beam was sent through a 1:1 telescope and spatial filter to clean up the transverse intensity profile, then into a Twyman-Green interferometer, configured as shown in Figure 7-13. An imaging lens captured the interference pattern and projected it with 4x magnification onto a PV-320 thermal camera. A computer recorded the camera images for later analysis.

7.2.3 Experimental Procedure

The following data acquisition and analysis procedure was conducted for a variety of pumping conditions to characterize the Cr^{2+}:ZnSe laser disks. First, the interferometer and pumping optics were aligned, the pump laser power was set, and the five phase-shifted interference patterns needed for the PSI data analysis were recorded using the camera and computer. (Five images were needed instead of four because the simple error reduction technique was used.) Next the interference pattern images were loaded into Matlab as two-dimensional arrays of intensity, and a phase map was calculated using the phase-shifted interferometry technique. Average temperature profiles were calculated for cross sections of the phase map, and then the phase map was fitted with a parabolic surface via least squares to obtain the approximate thermal lens power.

Temperature inside the laser disk was estimated by solving the expression below for ΔT, the longitudinally averaged temperature change, at each element in the phase map matrix. Here, $\Delta\phi$ is the phase difference, λ is the wavelength of the interferometer light source, L is the distance light travels through the laser disk (2 times the disk thickness), and dn/dT is the change in the refractive index of the disk with temperature (70×10^{-6} K^{-1} for ZnSe).

$$\Delta\phi = \frac{2\pi L \Delta T}{\lambda} \frac{dn}{dT} \tag{7-8}$$

This expression assumes the Cr^{2+}:ZnSe disk acts as a thin lens on the interferometer probe beam. The assumption is valid, as the shortest focal lengths measured were greater than 2 cm, and the thickest disk was only 1-mm thick. Solving this equation for all elements in the phase map matrix yields a map of longitudinally-averaged temperature at a grid of points (x_i, y_j) on the pumped crystal.

Unfortunately, the 'raw' temperature map values were susceptible to error from interferometer tilt, making the disk seem hotter than it really was (especially at low pump power levels). This error in estimated temperature difference could account for as much as 50% of the total estimated temperature difference at low pump power, making accurate (z-averaged) temperature estimation impossible at low pump power levels. To remove the effects of interferometer tilt, the temperature around the edges of the phase map was averaged to provide a 'tilt-resistant' baseline temperature. Peak temperature difference was obtained by subtracting the average baseline temperature from the peak temperature.

Fitting of a parabolic surface representing the effect of a thin lens with a given lens power to the data and estimating the thermal lens power were performed using the following technique. The parabolic surface was represented in Cartesian coordinates as:

$$P = A_0 + A_1 x + A_2 y + A_3 xy + A_4 x^2 + A_5 y^2 \tag{7-9}$$

An appropriately sized data window was applied to the matrix of phase data before the least squares fit operation was performed, to limit the least squares fitting region to the region of interest, namely the pumped area on the laser disk or some fraction thereof. The least squares fitting of the surface used the standard method of approximately solving the equation $P=HA$ for the unknown vector A, given that P is a known vector and H is a known matrix (which is not square). First, the phase data matrix was converted into a long column vector P. The matrix H was then created, with each row consisting of the polynomial terms $(1,x,y,xy,x^2,y^2)$ evaluated at the coordinates (x,y) corresponding to that row in P. Finally the coefficients of A were solved for in a least squares sense using the 'pseudo-inverse' method:

$$\vec{A} = (H^T H)^{-1} H^T \vec{P} \tag{7-10}$$

The focal length of any lensing present in the phase data was deduced from the coefficients of the second order terms in the fitted surface polynomial using the expressions shown below:

$$f_x \cong \frac{1}{2A_4}, f_y \cong \frac{1}{2A_5}, f_{tot} = \frac{f_x + f_y}{2} \tag{7-11}$$

To ensure that any astigmatism would be fully observable, a transformation of coordinate basis was performed to eliminate the cross term (xy) in the curve-fit polynomial, and thereby line up the principal axes of the polynomial surface curvature with the Cartesian coordinate axes. Finally, the component focal lengths were averaged together to produce an overall focal length. For data presentation, the average focal length was inverted to produce an average lens power in diopters (1/m).

7.2.4 Experimental Cases

The thermal characterization experiment was performed several times for each mounted Cr^{2+}:ZnSe disk under the following pumping conditions (all non-lasing, due to lack of appropriate optics).

1. 1-mm Cr^{2+}:ZnSe disk, CW multimode Tm:YLF, 0-5W input power
2. 0.5-mm Cr^{2+}:ZnSe disk, CW multimode Tm:YLF, 0-5W input power
3. 1-mm Cr^{2+}:ZnSe disk, Q-switched multimode Tm:YLF with 10 kHz rep. rate, 1 μs FWHM pulse-width, 0-5W input power
4. 0.5-mm Cr^{2+}:ZnSe disk, Q-switched multimode Tm:YLF with 10 kHz rep. rate, 1 μs FWHM pulse-width, 0-5W input power
5. 1-mm Cr^{2+}:ZnSe disk, Q-switched fiber-launched Tm:YLF with 10 kHz rep. rate, 1 μs FWHM pulse-width 0-5W input power

The Cr^{2+}:ZnSe disks were the same ones used in the laser All pumping cases covered the range of 0-5 W input power in steps of 1 W and used the multi-pass pumping optical system In cases 1-4, the input pump beam had a radius of 0.4-mm at the disk and an M^2 of 5. In case 5, the Q-switched Tm:YLF pump beam was run through a multimode

optical fiber with 0.22 NA and 200-μm diameter before being imaged onto the Cr^{2+}:ZnSe disk. The high divergence fiber-launched pump beam had a radius of 0.5-mm at the disk and an M^2 of ~20. Due to the multiple-pass pumping, the absorbed power distribution in the laser disks differed from the intensity distribution of the input pump beam. Imaging the Cr^{2+} fluorescence from the pumped disks allowed the absorbed power distribution in the disks to be estimated. Table 7-3 shows the approximate absorbed power profile in the Cr^{2+} laser disk for each of the pumping cases.

Table 7-3. Pumping Conditions for the Thermal Characterization Experiment

Case:	Disk Thickness:	Pumping:	Tranverse Absorbed Power Distribution
1	1.0 mm	5 W CW	N=4 Super Gaussian, 0.41-mm Radius
2	0.5 mm	5 W CW	N=4 Super Gaussian, 0.45-mm Radius
3	1.0 mm	5 W Q-Sw.	N=4 Super Gaussian, 0.45-mm Radius
4	0.5 mm	5 W Q-Sw.	N=5 Super Gaussian, 0.6-mm Radius
5	1.0 mm	5 W Q-Sw. Fiber	N=4 Super Gaussian, 0.5-mm Radius

7.2.5 Results

The experimental procedure was repeated for all five experiment cases at an array of pump power levels going from 0 to 5 W in 1-W steps. This section presents the step-by-step results from one part of one case, that of the 1.0-mm Cr^{2+}:ZnSe disk pumped with 5-W CW pump power, then summarizes the measured thermal lens power and maximum temperature rise in the disks as a function of pump power for all five cases.

The outcomes of the intermediate steps are shown in Figure 7-14 through Figure 7-18. Figure 7-14 shows an interference pattern image and a contour plot of the 'wrapped phase' estimate obtained from the phase-shift interferometry. Figure 7-15 shows a 3-D representation of the phase estimate after the phase unwrapping procedure.

Note that there are approximately four waves of total phase curvature present in the 3x3-mm phase map. Next, Figure 7-16 shows a horizontal cross-section plot of the phase map (through the center of the pumped region) showing the heat-induced phase curvature and a parabolic curve-fit for the thermal lensing that corresponds to the phase curvature. The curve-fit was performed using a 0.5-mm data window to guarantee the accurate calculation of the thermal lens focal length present at the very center of the pumped region, illustrating the most extreme thermal lensing measured in the entire experiment. An optical power of 38 diopters (or 2.6-cm focal length) was found.

Figure 7-17 shows a second phase map cross section, but this time the curve-fit used a larger sized data window, 1.0-mm diameter, to illustrate the thermal lensing averaged across the entire pumped region. Notice the much longer thermal-lens focal length, 4.5 cm, and the poor quality of the curve fit when the 1-mm data window was used. Evidently, a 1-mm diameter beam would experience significant aberration in passing through this pumped laser disk.

Finally, a horizontal cross section of estimated longitudinally-averaged temperature is shown in Figure 7-18. The temperature cross section plot reveals that the crystals do get hot, up to 65°C hotter in the center of the pumped region than at the coldest point on the disk, according to the raw temperature data. As noted above, however the 'raw' temperature values contain error resulting from interferometer tilt. With the appropriate baseline temperature calculated by averaging the temperature around the edges of the temperature map, the peak temperature difference was approximately 46 °C.

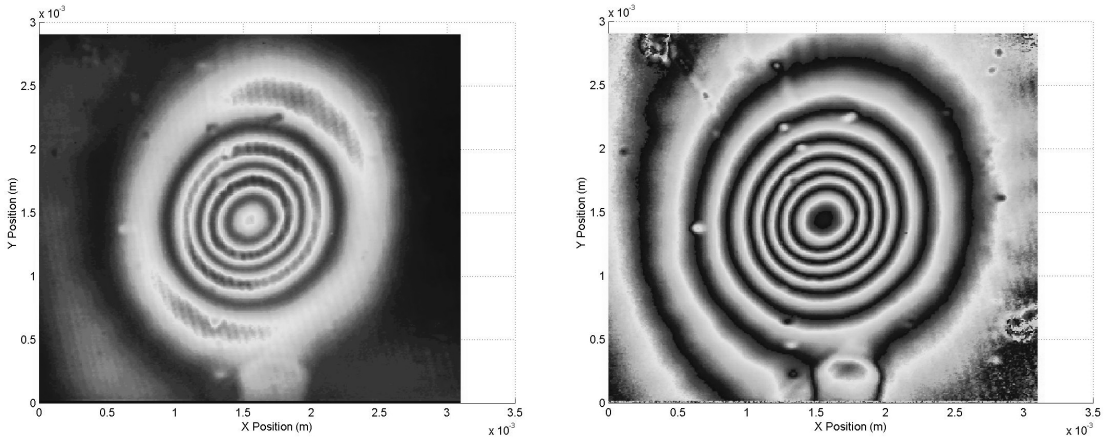

Figure 7-14. Interference Pattern and Resulting 'Wrapped Phase' Estimate for Experiment Case 1: 1-mm Cr^{2+}:ZnSe Disk pumped by a 5 W, 0.4-mm Radius 4th Order Super-Gaussian Beam.

This set of plots shows an image on the left of an interference pattern in 2.05-μm light captured by a PV-320 camera, and the resulting wrapped phase estimate constrained to lie on the interval [0,2π]. Note the high contrast fringes, and also the presence of phase discontinuities at small damage sites.

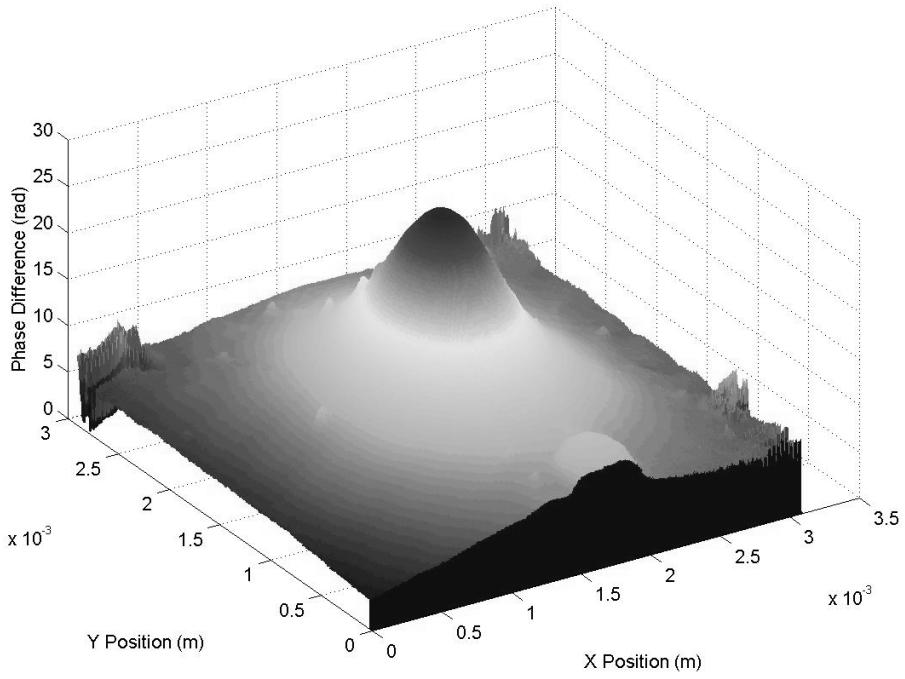

Figure 7-15. 'Unwrapped' Phase Estimate, Experiment Case 1

This plot is for the 1-mm disk, pumped with 5-W CW in 0.4-mm radius. This is the most extreme phase curvature measured in this experiment, corresponding to the shortest focal length thermal lens.

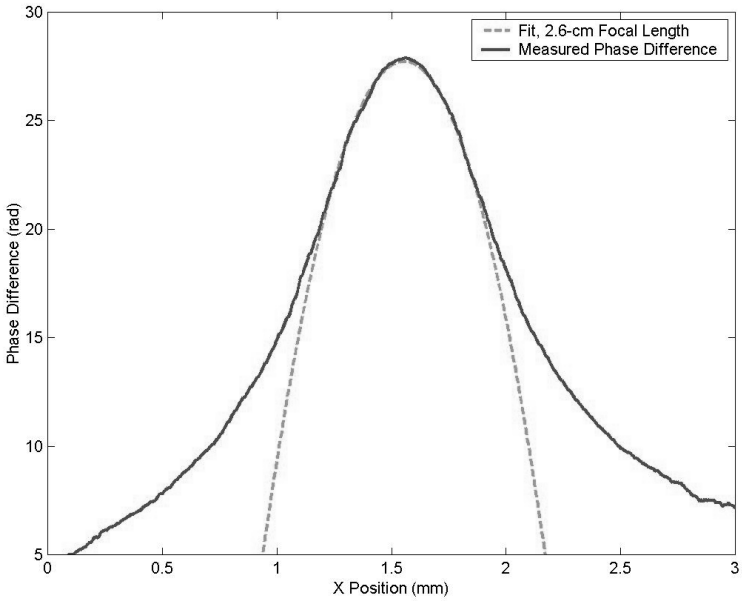

Figure 7-16. Measured Thermal Lensing in 1-mm Disk, Case 1, 0.5-mm Curve Fit
This plot shows a horizontal cross section of the transverse phase curvature an incident plane wave would receive after passing twice through the disk. Pumping is 5-W CW in a 0.4-mm radius beam. The curve fit with 0.5-mm data window results in 2.6-cm thermal lens focal length. Notice that the curve fit is better for the center than at the edges of the pumped region.

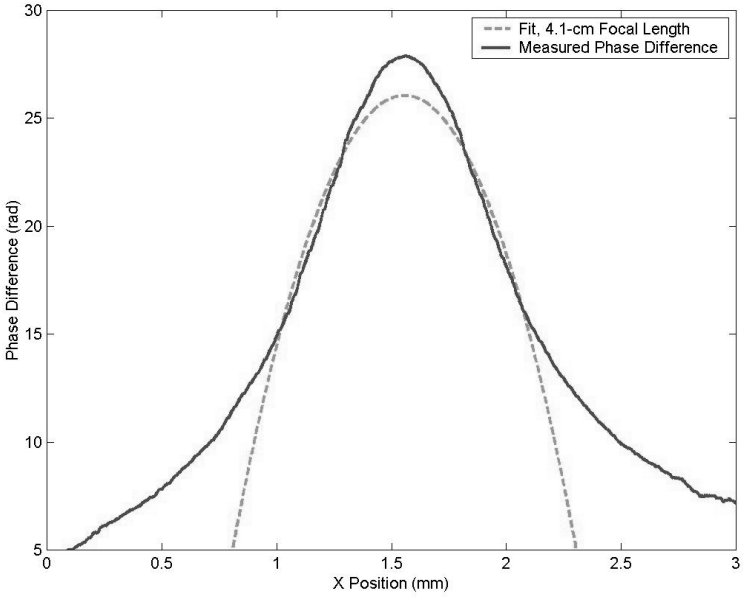

Figure 7-17. Measured Thermal lensing in 1-mm Disk, Case 1, 1-mm Curve Fit
This plot shows the same thing as Figure 7-17, just with a 1-mm data window for the curve fit. Notice that the curve fit is not good at the center, but isn't bad for most of the pumped region area. A thermal lens focal length of 4.1 cm was estimated.

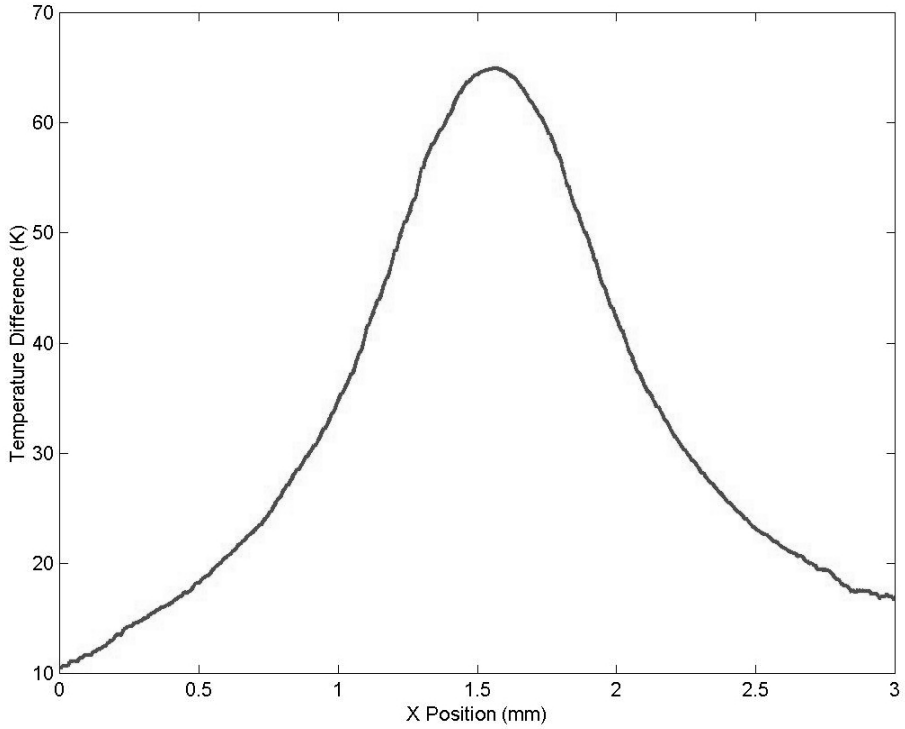

Figure 7-18. Cross Section of (Z-averaged) Temperature Distribution in 1-mm Cr^{2+}:ZnSe Disk 1: 5-W Pumping in a 0.4-mm Beam Radius
This is an estimate of longitudinally averaged temperature obtained from the phase curvature data (using $70x10^{-6}$ as the dn/dT value for Cr^{2+}:ZnSe)

The results of the thermal characterization experiment are summarized in the table and plots below. The results are presented in terms of thermal lens power (in diopters) and maximum (longitudinally averaged) disk temperature as a function of pump power. To make Table 7-4, the maximum temperatures and average thermal lens powers (1/focal length) for each pump power level of each case were plotted vs. pump power. Lines were fit to the plots, to estimate the dependence of the quantities of interest on the pump power. A linear dependence was assumed for peak temperature and thermal lens power, as would be expected, and was mostly supported by the plots, Figure 7-19, Figure 7-20, and Figure 7-21.

Table 7-4. Thermal Lensing and Max. (Z-Avg.) Temperature in Cr^{2+}:ZnSe Disks

Experiment Case:	1	2	3	4	5
Pumping: (CW or Q-switched) (Radius)	CW 0.41 mm	CW 0.45 mm	Q-Sw 0.45 mm	Q-Sw 0.6 mm	Q-Sw 0.5 mm
Disk Thickness:	1 mm	0.5 mm	1 mm	0.5 mm	1 mm
Lens power, 1.0-mm curve-fit (m^{-1}/W)	4.24	1.90	3.66	0.81	3.10
Lens power, 0.5-mm curve-fit (m^{-1}/W)	6.95	3.32	5.47	1.13	4.11
Max long. avg. temp rise (°C/W)	9.1	8.12	8.2	3.9	7.4

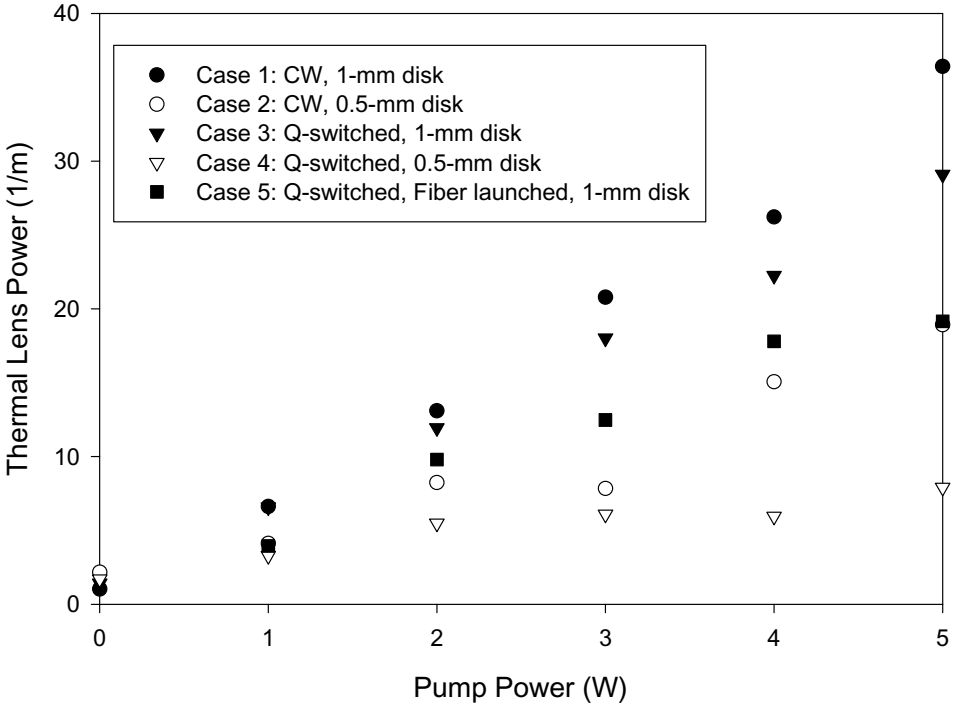

Figure 7-19. Measured Thermal Lens Power in Pumped Cr^{2+}:ZnSe Disks, 0.5-mm Data Window Used in Curve Fitting

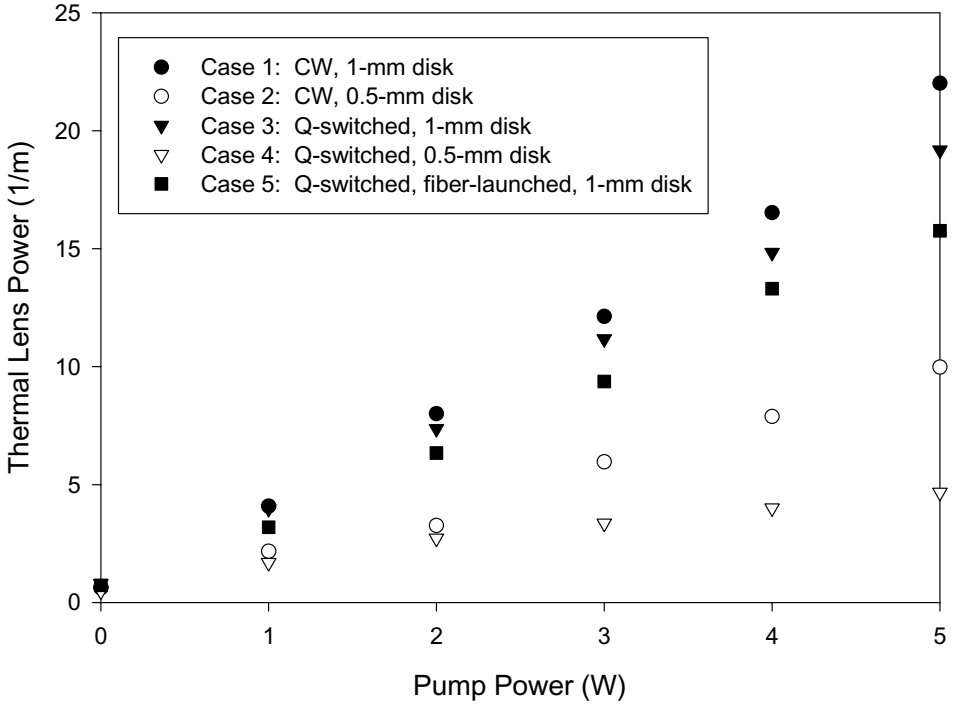

Figure 7-20. Measured Thermal Lens Power in Pumped Cr^{2+}:ZnSe Disks, 1.0-mm Data Window Used in Curve Fitting

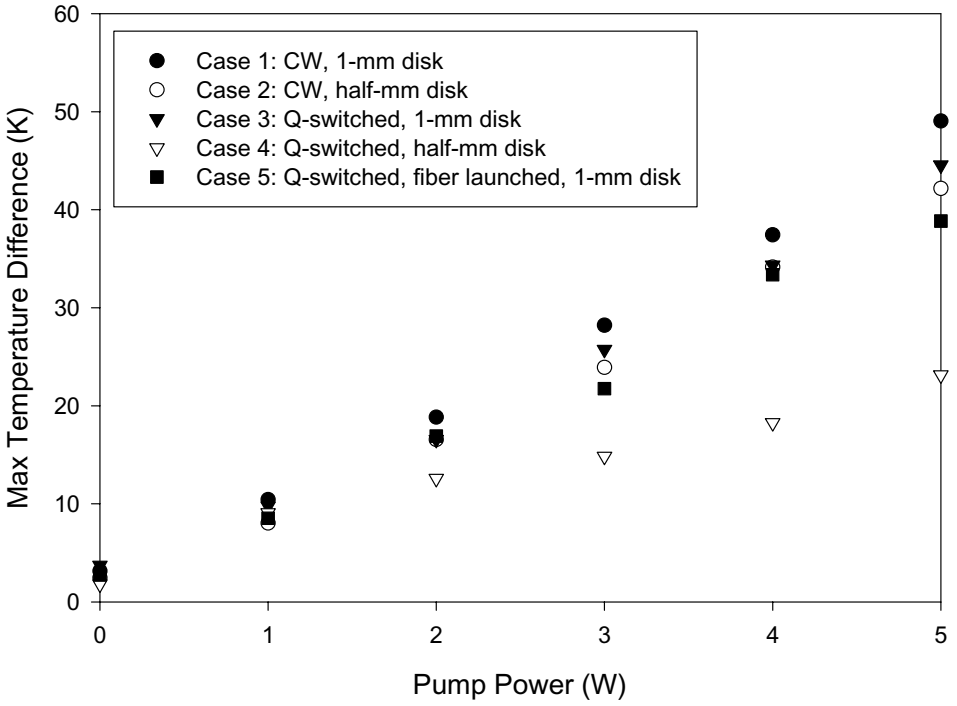

Figure 7-21. Peak (Z-Avg.) Temperature in Pumped Cr^{2+}:ZnSe Disks

7.2.6 Interpretation of Results

Results of the thermal characterization experiment suggest the following trends:

1. **The thermal lens power and peak temperature in the disks were indeed approximately linearly dependent on pump power**, at least under the conditions used in this experiment.
2. **It took only a few watts of incident pump power to raise the average temperatures in the Cr^{2+}:ZnSe disks to the point where nonradiative relaxation becomes significant.** The peak z-averaged temperature in the disks increased approximately 8 K per watt of pump power for 0.4-mm radius pumping. With a 293 K heat sink temperature, 5 watts of input power yielded a temperature of approximately 333 K in the disks – hot enough for nonradiative relaxation to lower the laser gain by ~30 %. The reason why the temperature increase per watt of pump power is so high is not known. To solve this puzzle, two unknown quantities need to be measured: temperature profiles of each disk while lasing, and the thermal resistance of the boundary between each disk and its heat sink.
3. **The 0.5-mm disk exhibited less than half the thermal lensing seen in the 1.0-mm disk, but had similar values of peak temperature**.
4. **CW pumping produced stronger thermal lensing than Q-switched pumping.** It is thought that bleaching of the Cr^{2+} absorption during Q-switched pumping reduced thermal lensing by flattening the absorbed power distribution and increasing the size of the pumped region. This can happen because the Cr^{2+}:ZnSe disk can only absorb a finite amount of pulse energy per unit volume for a short pulse. If there is more

energy in the center of the transverse energy distribution of the pump pulse than can be absorbed in the Cr^{2+}, it just passes through. The absorbed power distribution will be 'clipped' at some maximum value, which will tend to flatten the absorbed power profile.

5. **The thermal lensing considered over the entire pumped region as a whole was significantly aberrated**, as indicated by the approximate factor of 1.5 change in calculated thermal lens powers produced by using the two different-sized data windows for the curve-fitting procedure. If there were no aberration, changing data window size would have no effect on estimated thermal lens power. The variation in calculated thermal lens power was largest (a factor of 1.7) in the CW-pumped cases and smallest (a factor of 1.3) in the Q-switched, fiber-pumped 1-mm disk.

The accuracy of this experiment is somewhat difficult to quantify, as there are many potential sources of error, such as interferometer aberration, damaged spots on the crystals, curve-fitting errors, and drift in pump laser power and beam parameters. To place some bounds on the experimental error, the experiment was repeated for a mirror of known radius of curvature. The phase unwrapping method identified the 10-cm radius of curvature with an accuracy of at least 15%, and detected about a 2-meter residual erroneous curvature on a flat reference mirror. Based upon these results, the likely overall accuracy of thermal lensing and temperature estimates is no worse than 20%. It appeared that aberrations in the interferometer such as astigmatic probe beams, tilt, and spherical aberration are to blame for the errors, as they were present in some form for all of the optics and crystals tested. Even with the error, this interferometric technique was

by far more informative and useful than other techniques that could be used, such as razor blade scanning or measuring far-field spot size.

7.3 Comparison of Modeling and Experimental Results

The thermal lensing modeling compared surprisingly well with the experimental results, with both revealing the same trends. Both modeling and experiment showed a linear relationship between temperature and thermal lens power as a function of absorbed pump power. Temperature profiles and thermal lens powers were comparable for a given disk, pump beam radius, and input power level, within a factor of 2. The modeled results showed higher thermal lensing and peak temperatures in the disks, but the models also assumed that all the input power was converted to heat (no fluorescence). The 11 K temperature rise per watt of pump power predicted by the model (for 100% heat load) makes the 8 K temperature rise per watt of pump power found in the experiment correspond to a 75% heat load. This is a bit high, 50%-60% being more reasonable, but within experimental error margins. Reducing the disk thickness produced the anticipated reduction in thermal lensing without significant changes in either peak temperature or the average transverse temperature distribution in the disks. Experimentally measured thermal lensing showed the same kind of aberration found in the modeled thermal lensing. The aberration was significant for 0.4-mm radius Gaussian pumping of the 1-mm disk, no surprise considering the results of the laser experiments in Chapter 0.

Overall, the thermal modeling was able to capture the basic trends needed for laser resonator design tradeoff analyses, and the predicted temperature profiles agreed fairly well with the experimental results. Modeled results, however, may be no more accurate

than a factor of two, as there are several optical and thermal parameters involved with real Cr^{2+}:ZnSe laser disks which are poorly known, difficult to measure and therefore cannot be represented accurately in the thermal models.

8 Conclusion

This chapter presents a summary of the salient findings of this research, draws overall conclusions as to overall feasibility of high power Cr^{2+} lasers, and presents recommendations for future work in Cr^{2+} laser power scaling.

8.1 Research Summary

Cr^{2+} materials were shown to be suitable as lasers in the 5-W level, but material properties rigidly constrain laser design. Background research and material characterization experiments showed that the Cr^{2+}:II-VI laser materials have potentially very efficient quasi 4-level laser dynamics, can handle at least as absorbed power density as the YLF used in the 15-W pump laser without thermal fracture, and can be tuned perhaps as much as 1000-nm in a suitably broadband resonator. However material properties made power scaling difficult, especially for the limited 15-W pump laser power available, due to the high dn/dT of ~$70x10^{-6}$, the Cr^{2+} doping density limitation of $5x10^{18}$-$5x10^{19}$ cm^{-3}, and the onset of significant non-radiative relaxation at room temperature. Of the three Cr^{2+} materials examined, Cr^{2+}:ZnSe, Cr^{2+}:CdMnTe, and Cr^{2+}:CdSe, the Cr^{2+}:ZnSe proved most promising for power scaling, due to its high Cr^{2+} doping density of 2-$5x10^{19}$ cm^{-3} and good thermal conductivity of 18 W/mK. Choice of this material precluded any demonstration of high power output at wavelengths longer than 3 μm, but was necessary given time constraints and the properties of available laser materials. Available pump laser power and Cr^{2+} material properties pointed to the disk laser as the most feasible configuration. The design was based upon a highly doped, thin

Cr^{2+}:ZnSe disk, a 1.89-μm Tm:YLF pump laser, multi-pass pumping producing a 1-mm diameter pumped spot size, and a simple high-Q standing-wave resonator.

Cr^{2+}:ZnSe disks with at least 10^{19} cm^{-3} Cr^{2+} doping and thickness of 1 mm or 0.5 mm were obtained, coated, and mounted directly on water-cooled heat sinks. Disk coating pushed the limits of mid-IR coating technology, but did indeed result in low loss, reasonably high damage threshold coatings. Loss was < 5% in the 1-mm disk and < 3% in the 0.5-mm disk, low enough for efficient laser operation. Two disk mounting techniques were tried, solder and epoxy, with the solder proving more satisfactory as it prevented disk warpage, but was also a more risky operation. Both disks withstood non-lasing absorbed power densities up to 10 kW/cm^3 without thermal fracture, well beyond the level at which YLF in the pump laser would fracture under non-lasing conditions.

Once mounted, both disks produced efficient 10-kHz pulsed laser operation in a simple, 8-cm long multi-mode laser cavity with 10-cmcc, 90%+ reflectivity output mirror and a 0.9-mm diameter pumped spot, with the best performance being 47% incident power efficiency demonstrated at 4.3 W of 2.5-μm output. The disk laser experiments showed that over 4-W average power could be obtained at 2.5 μm from a Cr^{2+}:ZnSe disk laser using a 15-W 2-μm pump source and at least 8-pass.

Unfortunately, the reduction of thermal lensing through the use of thin disks did not fulfill the expectations of the initial design, resulting in disappointing CW performance overall, and disappointing pulsed performance in any cavity but a short multi-mode configuration using a 10-cmcc output mirror. The original resonator design based upon weak thermal lensing and consisting of a 50-cmcc output coupler and 25-cm cavity

length did not work at all. Even the short-cavity multi-mode backup design for conditions of strong thermal lensing did not achieve good CW performance, despite its success for pulsed laser operation. The best CW performance was 1.4 W in a one-time demonstration from the 0.5-mm disk (which subsequently dimpled at that spot– a casualty of the epoxy mounting method). The 1-mm disk never lased CW at all, though it escaped CW damage.

The mediocre efficiency was not predicted by the simple qualitative cavity stability and mode-coupling analysis, even when thermal lensing was accounted for. Later thermal lensing modeling and measurement, along with a specially designed mode-matching experiment, provided indications that the problem was likely aberration in the thermal lens as much as the lensing itself. Both the lensing and the aberration were much stronger than originally anticipated and could not be ignored.

The discovery of possible thermal aberration precipitated an exhaustive characterization of thermal lensing in the laser disks using both finite-element models and phase-shifting interferometry. It was found that the 16-pass pumping system did a great job of efficiently delivering pump power to the Cr^{2+}:ZnSe disks, producing 90%-95% absorption efficiency in less than a 1-mm diameter spot on the disks. The absorbed power distribution, however, was had too much radial variation to allow the thermal lens reduction that is the hallmark and basic requirement of the laser design, and strong, aberrated thermal lensing persisted.

The absorbed power distribution in the laser disks was characterized by a so-called super-Gaussian function of order 4 with radius of ~0.45 mm. An attempt was made to

flatten the absorbed power distribution by running the pump laser through a 200-μm core, 0.22 NA optical fiber. This did not result in an appreciable change in absorbed power distribution, though the fiber did effectively isolate the pump laser, eliminating the need for a Faraday isolator with its 15% loss in the pumping system. Success with this technique has been reported in the literature, and it might have worked in this experiment had a larger core fiber, or a larger pump spot size been used.

The absorbed power distribution produced in the laser disks by the 16-pass pumping system generated thermal lens power (for light traveling through the disk twice) in the range of 6 diopters per watt of absorbed pump power for the 1-mm disk, and a bit less than half that for the 0.5-mm disk for CW excitation. The temperature-induced optical path difference in the disks was found to approximate the absorbed power distribution in the center of the pumped spot, but to taper off more slowly than the absorbed power distribution at the edges. This resulted in aberrated thermal lensing with overall focal length measured around the rim of the gain region being significantly longer than the focal length measured in the center of the gain region. Disappointing laser efficiencies were attributed to this phenomenon.

The peak longitudinally-averaged temperatures measured in the disks were approximately 8 K per watt of pump power at the hottest spot. When compared to the modeling results of 11 K per watt of absorbed pump power (which assumed 100% heat loading), a heat load estimate of 75% was obtained. This was high, but not unreasonable given the known non-radiative relaxation processes that occur in the disks. For instance, the 1-mm disk was estimated to have a 60% nonlasing heat load at room temperature,

given its 15% overall radiative heat load and 50% quenched fluorescence lifetime of 4 μs. The difference between the modeled and measured values is within the experimental uncertainty of these experiments. Lasing heat load, as previously mentioned, was not measured in this experiment due to the lack of appropriate optics, but would likely be substantially less than in the non-lasing case, perhaps as low as 30% of the absorbed pump power. This would suggest maximum temperature increases of ~4 K per watt under lasing conditions. The laser producing 4-W output with 10-W pumping would therefore have experienced peak z-averaged temperatures in the laser disk of up to 333 K.

8.2 Feasibility of High Power Cr^{2+} Lasers

In light of this research, it appears that Cr^{2+} lasers with outputs in excess of 5 W are feasible, but many simultaneous design constraints that must be satisfied for acceptable laser operation. Although it seems obvious, a first requirement is an affordable pump source with ~2-3 times more power than the desired Cr^{2+} laser output power. Only recently have ~40-W 1.9-μm lasers become available, and most of those are fiber lasers capable of only CW operation. Nicely packaged pulsed high power 1.9-μm lasers are still hard to come by.

The Cr^{2+}:ZnSe laser material itself appears to handle the power density and high (multiple-passed) pump intensity well, which is promising for power scaling to 10 W or higher. The intrinsic loss in the laser material is low enough for disk-type samples at least to achieve high laser efficiency in high-Q laser cavities. Pump absorption should not be a problem, as long as the correct pump wavelength and multiple-pass pumping are

used. The effects of thermally induced optical distortion, however, are strong enough to dominate Cr^{2+} laser cavity dynamics if any absorbed pump power non-uniformity exists.

Other issues such as non-radiative relaxation, Cr^{2+} bleaching, and damage appear secondary in comparison, and indeed could be dealt with more easily if the thermally induced distortion were not present. The primary obstacle to further power scaling is thus the optical distortion caused by radially non-uniform temperature profiles in the Cr^{2+} laser materials, a problem expected to affect all Cr^{2+}:II-VI materials, and be worse for II-VI host materials with lower thermal conductivity, such as CdSe and CdMnTe.

8.3 Recommendations

Despite many different experimental difficulties, the only insurmountable in this power scaling research were the thermally induced optical distortion in the Cr^{2+} laser disks and the lower than expected power of the pump source. The distortion was caused by a transverse temperature distribution in the laser material that produced a non-spherical optical path length difference distribution that could not be compensated for by spherical optics. The pump source power limitation resulted from limited budget and inadequate optical coating damage tolerances. Given that the pump source power will be determined by budget and availability, further Cr^{2+} research should focus on techniques to mitigate thermal lensing or thermal lens aberration. This will likely produce the most return for the effort expended, and should require neither an increase in pump power, nor abandonment of the disk laser concept.. Specific research recommendations are described below.

8.3.1 Use Radially-Uniform Pumping in Cr^{2+} Materials

For the disk laser design described in this research, it is recommended that the pumping system be altered to produce a radially-uniform absorbed power distribution. The thermal modeling indicated that such a distribution will reduce thermal lens power and significantly reduce aberration relative to the results reported here. The original disk laser design called for this, but it was not achieved by the pumping system

A localized uniform absorbed power distribution equates to pumping by a true 'top-hat' beam. This can be achieved in principle by forcing the pump laser to produce one using a graded reflectivity cavity mirror, by using a commercially available holographic transverse 'mode converter,' or by running the pump beam through a 1-mm diameter rod waveguide. For the current 16-pass optical system, increasing the beam diameter to ~1.5 mm might also yield considerable improvement, although more pump power would be needed. It is worth noting that modeling suggests the combination of top-hat pumping, 1.5-mm beam diameter, and 0.25-mm disk thickness should result in negligible thermal lensing, ~2-m double-pass focal length for a 5-W heat load.

8.3.2 Improve Cr^{2+}:ZnSe to Obtain Working 0.25-mm disks

In parallel with improvements in pump intensity distribution, it is recommended that Cr^{2+} materials research be conducted to produce usable 0.25-mm disks. One approach is to experiment with processing techniques to reduce or eliminate the need to polish the surfaces of the Cr^{2+}:II-VI samples after the doping run. It would also be invaluable to determine why nonradiative relaxation becomes significant at Cr^{2+} concentrations as low as 10^{19} cm^{-3} and how it might be prevented to exploit higher Cr^{2+} doping.

8.3.3 Modify The Disk Laser Design

There is a guaranteed way to eliminate thermal lensing: ensure no radial temperature gradients occur at all in the laser material. This has proven difficult but might be possible with two simple modifications to the disk laser design.

One modification, admittedly speculative, involves placing a heating element on the input face of the disk, with a hole in it where the pump and resonated light travel through. The inevitable radial cooling that occurs during pumping a large diameter disk with a small pump beam could be dynamically compensated by controlling the temperature of the heating element. This works even for thick disks, and could be implemented on the existing disk laser design fairly easily. At a 5-W optical heat load (expected at 17-W pumping while the laser is running), a maximum heating element intensity of ~600 W/cm^2 would be required to match the optical heat load. This results in a modest requirement of 55 W for a 5-mm diameter heating element with 1.2-mm diameter central hole. If the overall cooling capacity of the system allows, thermo-electric coolers could be used on both sides of the disk as combined heating and cooling elements to maintain positive control over both absolute disk temperature and temperature gradients. This would be the ideal way to cool the Cr^{2+} laser material down below room temperature and maintain temperature with the least amount of difficulty.

A second modification is to use the top-hat pump beam, and a disk with diameter no larger than that of the beam. If the heat transfer through the edge of the disk is negligible, there will be in theory no radial cooling and thus no radial temperature gradient. Thermal modeling indicates that simply exposing the disk edges to still air would be effective.

Like the previous design, this configuration does not require a thin disk for optimum performance, and might in fact work better and be easier to implement using a short laser rod: a 1-2 mm diameter cylinder with 1-2 mm thickness. As in the disk laser design, the laser material needs to be face cooled, but the barrel of the cylinder should be exposed to the air or well insulated. Diffraction loss in a multiple-pass pump system might be a problem for this configuration, but more than two passes would not be needed in a 1-2 mm disk of highly doped Cr^{2+}:ZnSe. On-axis pumping could be effectively used and there would be enough room in the laser head to put a transparent heat sink on the input face for additional cooling. This technique looks especially promising for high energy pulsed operation, as the thick disk will have greater energy storage volume than a thin disk would for equivalent concentrations, and the resulting high gain laser resonator would tolerate the extra loss associated with the transparent heat sink. This design could be combined with the previous design, by face cooling the laser rod but having a heating/cooling element around the barrel of the rod, providing some dynamic control of thermal lensing if so desired.

A final possible improvement to the disk laser design is using transparent heat sinks on both faces of the laser disk. This would make the face-cooling geometry easier to implement, as there could be access into the laser material from both faces. Currently, no material is available except diamond that could outperform the copper heat sink on the mirror face, and diamond absorbs in the Cr^{2+} emission band. If silicon carbide optical material properties and availability improve slightly, however, transparent SiC heat sinks with an index similar to that of Cr^{2+}:II-VI materials but with thermal conductivity greater

than copper could be used to face-cool both ends of the laser disk or rod. The pumping induced temperature changes in the Cr^{2+} samples would be half the magnitude as in the present configuration and laser design would be much more flexible. The Cr^{2+} disks would not even need to be coated, but simply optically contacted to SiC windows that are coated on one face only. This would allow Cr^{2+}:CdSe and Cr^{2+}:CdMnTe to be used in low loss normal incidence configurations even though optical coatings are not yet developed for these materials.

Bibliography

1. DeLoach, L.D., *et al.*, *Transition metal-doped zinc chalcogenides:spectroscopy and laser demonstration of a new class of gain media.* IEEE Journal of Quantum Electronics, 1996. **32**(6): p. 885-895.

2. Kuck, S., K.L. Schepler, and L. Shiozawa, *Cr2+ emission spectroscopy in CdSe.* Journal of Luminescence, 1997. **72-74**: p. 116-117.

3. Hommerich, U., *et al.*, *Demonstration of room-temperature laser action at 2.5 μm from Cr2+:$Cd_{0.85}Mn_{0.15}Te$.* Optics Letters, 1997. **22**(15): p. 1180-1182.

4. Wagner, G.J., *et al.*, *Continuous-wave broadly tunable Cr2+:ZnSe laser.* Optics Letters, 1999. **24**(1): p. 19-21.

5. Wagner, G.J. and T.J. Carrig, *Power Scaling of Cr2+:ZnSe Lasers*, in *Advanced Solid State Lasers, OSA Technical Digest*. 2001, Optical Society of America: Washington, DC. p. 335-370.

6. Carrig, T.J., *et al.*, *Acousto-Optic Mode-Locking of a Cr2+:ZnSe Laser*, in *OSA Trends in Optics and Photonics, Advanced Solid State Lasers*, H. Injeyan, U. Keller, and C. Marshall, Editors. 2000, Optical Society of America: Washington DC. p. 182-187.

7. Sorokina, I.T., *et al.*, *Active and passive mode-locking of Cr2+:ZnSe*, in *Advanced Solid State Lasers, OSA Technical Digest*. 2001, Optical Society of America: Washington, DC. p. 87-89.

8. Mond, M., *et al.*, *Continuous Wave Diode Pumped Cr2+:ZnSe and High Power Laser Operation*, in *OSA Trends in Optics and Photonics, Advanced Solid State Lasers*, C. Marshall, Editor. 2001, Optical Society of America: Washington, DC. p. 162-165.

9. Page, R.H., *et al.*, *Demonstration of diode-pumped and grating-tuned ZnSe:Cr2+ lasers*, in *OSA Trends in Optics and Photonics, Advanced Solid-State Lasers*, C.R. Pollock and W.R. Bosenberg, Editors. 1997, Optical Society of America: Washington DC. p. 208-210.

10. Adams, J.J., *et al.*, *Tunable Laser Action at 4.0 microns from fe:ZnSe*, in *OSA Trends in Optics and Photonics, Advanced Solid State Lasers*, M. Fejer, H. Injeyan, and U. Keller, Editors. 1999, Optical Society of America: Washington DC. p. 435-440.

11. Page, R.H., *et al.*, *Recent developments in Cr2+-doped II-VI compound lasers*, in *OSA Trends in Optics and Photonics, Advanced Solid State Lasers*, S.A. Payne and C. Pollock, Editors. 1996, Optical Society of America: Washington, DC. p. 130-136.

12. Page, R.H., *et al.*, *Cr^{2+}-doped zinc chalcogenides as efficient, widely tunable mid-infrared lasers.* IEEE J. Quantum Electron., 1997. **33**(4): p. 609-619.

13. McKay, J.B. and K.L. Schepler, *Cr2+ Lasers: Efficient, Broadly Tunable Mid-IR Laser Sources*, in *Solid State and Diode Laser Technical Review, DEPS Technical Digest*. 2001, DEPS: Albuquerque, NM.

14. Grebe, G., G. Roussos, and H.-J. Schultz, *Cr2+ excitation levels in ZnSe and ZnS.* Journal of Physics C: Solid State Physics, 1976. **9**: p. 4511-4516.

15. Goetz, G., H. Zimmerman, and H.-J. Schultz, *Jahn-Teller interaction at Cr2+(d4) centres in tetrahedrally coordinated II-VI lattices studied by optical spectroscopy*. Zeitschrift fur Physik B, 1993. **91**: p. 429-436.

16. Podlipensky, A.V., *et al.*, *Passive Q-switching of Er:glass laser with Cr2+:ZnSe and Co2+:ZnSe saturable absorbers*, in *OSA Trends in Optics and Photonics, Advanced Solid State Lasers*, H. Injeyan, U. Keller, and C. Marshall, Editors. 2000, Optical Society of America: Washington DC. p. 249-253.

17. Henderson, B. and G. Imbusch, *Electronic Centres in a Vibrating Crystalline Environment*, in *Optical Spectroscopy of Inorganic Solids*. 1989, Clarendon Press: Oxford. p. 184-257.

18. Koechner, W., *Solid-state laser engineering*. 3rd completely rev. and updated ed. Springer series in optical sciences, v 1. 1992, Berlin ; New York: Springer-Verlag. xiii, 634.

19. Podlipensky, A.V., *et al.*, *1 W continuous wave laser generation and excited state absorption measurements in Cr2+:ZnSe*, in *OSA Trends in Optics and Photonics, Advanced Solid State Lasers*, H. Injeyan, U. Keller, and C. Marshall, Editors. 2000, Optical Society of America: Washington DC. p. 201-206.

20. Verdeyen, J.T., *Laser Electronics*. 1995, Englewood Cliffs, NJ: Prentice-Hall, Inc.

21. Wagner, G.J., *et al.*, *High-Efficiency, Broadly Tunable Continuous-Wave Cr2+:ZnSe Laser*, in *OSA Trends in Optics and Photonics, Advanced Solid State Lasers*, M. Fejer, H. Injeyan, and U. Keller, Editors. 1999, Optical Society of America: Washington DC. p. 427-434.

22. McKay, J., D. Krause, and K. Schepler, *Optimization of Cr2+:CdSe for Efficient Laser Operation*, in *OSA Trends in Optics and Photonics, Advanced Solid State Lasers*, H. Injeyan, U. Keller, and C. Marshall, Editors. 2000, Optical Society of America: Washington DC. p. 218-223.

23. Stewen, C., *et al.*, *Yb:YAG thin disk laser with 1 kW output power*, in *OSA Trends in Optics and Photonics, Advanced Solid State Lasers*, H. Injeyan, U. Keller, and C. Marshall, Editors. 2000, Optical Society of America: Washington DC. p. 35-41.

24. McKay, J., K.L. Schepler, and G.C. Catella, *Efficient grating tuned mid-IR Cr2+:CdSe laser.* Optics Letters, 1999. **24**(22): p. 1575-1577.

25. Erhard, S., *et al.*, *Pumping Schemes for multi-kW thin disk laser*, in *OSA Trends in Optics and Photonics, Advanced Solid State Lasers*, H. Injeyan, U. Keller, and C. Marshall, Editors. 2000, Optical Society of America: Washington DC. p. 78-84.

REPORT DOCUMENTATION PAGE

Form Approved
OMB No. 074-0188

1. REPORT DATE *(DD-MM-YYYY)*	2. REPORT TYPE	3. DATES COVERED *(From – To)*
03-2003	**Dissertation**	Oct 1999– Mar 2003

4. TITLE AND SUBTITLE

POWER SCALING FEASIBLILITY OF CHROMIUM-DOPED II-VI LASER SOURCES AND THE DEMONSTRATION OF A CHROMIUM-DOPED ZINC SELENIDE FACE-COOLED DISK LASER

5a. CONTRACT NUMBER

5b. GRANT NUMBER

5c. PROGRAM ELEMENT NUMBER

6. AUTHOR(S)

McKay, Jason B., Captain, USAF

5d. PROJECT NUMBER

5e. TASK NUMBER

5f. WORK UNIT NUMBER

7. PERFORMING ORGANIZATION NAMES(S) AND ADDRESS(S)
Air Force Institute of Technology
Graduate School of Engineering and Management (AFIT/EN)
2950 P Street, Building 640
WPAFB OH 45433-7765

8. PERFORMING ORGANIZATION REPORT NUMBER

AFIT/DS/ENP/02-05

9. SPONSORING/MONITORING AGENCY NAME(S) AND ADDRESS(ES)
AFRL/SNJW
Attn: Dr. Kenneth Schepler
3109 P Street DSN: 785-3804 x274
WPAFB OH 45433 e-mail: Kenneth.Schepler@wpafb.af.mil

10. SPONSOR/MONITOR'S ACRONYM(S)

11. SPONSOR/MONITOR'S REPORT NUMBER(S)

12. DISTRIBUTION/AVAILABILITY STATEMENT

APPROVED FOR PUBLIC RELEASE; DISTRIBUTION UNLIMITED.

13. SUPPLEMENTARY NOTES

14. ABSTRACT

Tunable lasers in the 2-4 μm wavelength range are needed for Air Force sensor applications. Chromium-doped II-VI materials are a promising class of laser material for tunable operation in this wavelength range, but until recently had not produced enough output power to meet application requirements. This dissertation investigates Cr^{2+}:II-VI material properties and potential laser designs, then experimentally demonstrates and analyzes the performance of a Cr^{2+}:ZnSe disk laser design that can produce sufficient output power. Cr^{2+}:II-VI laser materials are found to be susceptible to overheating and thermal lensing, but are otherwise satisfactory laser materials. The most feasible laser design given a 15 W pump power limit was a face-cooled disk laser design using Cr^{2+}:ZnSe. The experimental implementation of the laser design produced 4.3 W. However, the experimental laser worked well only under a restricted set of conditions, due to thermal lensing caused by a radially non-uniform absorbed power distribution in the laser disk. Design modifications are discussed which should reduce thermal lensing to acceptable levels. The conclusion is that Cr^{2+}:II-VI laser sources can produce enough power for Air Force sensor applications, if enough effort is spent on ensuring adequate thermal management in the laser material.

15. SUBJECT TERMS

Lasers, Laser Applications, Laser Spectroscopy, Transition Metal Lasers, Chromium Lasers, Chromium Doped II-VI Materials, Thermal Lensing

16. SECURITY CLASSIFICATION OF:			17. LIMITATION OF ABSTRACT	18. NUMBER OF PAGES	19a. NAME OF RESPONSIBLE PERSON
a. REPORT	b. ABSTRACT	c. THIS PAGE			Dr. Won B. Roh, (ENP)
U	U	U	UU	179	19b. TELEPHONE NUMBER *(Include area code)* (937) 255-3636, ext 4509; e-mail: Won.Roh@afit.edu